Univerzita Karlova v Praze
1. lékařská fakulta

Studijní program: Zobrazovací metody v lékařství

Ing. Martin Ovesný

Výpočetní metody v jednomolekulové lokalizační mikroskopii

Computational methods in single molecule localization microscopy

Disertační práce

Školitel: Dr. Guy Hagen, Ph.D.

Praha, 2016

Prohlášení:

Prohlašuji, že jsem záverečnou práci zpracoval samostatně a že jsem řádně uvedl a citoval všechny použité prameny a literaturu. Současně prohlašuji, že práce nebyla využita k získání jiného nebo stejného titulu.

Souhlasím s trvalým uložením elektronické verze mé práce v databázi systému meziuniverzitního projektu Theses.cz za účelem soustavné kontroly podobnosti kvalifikačních prací.

V Praze, 1.6.2016

Ing. Martin Ovesný

Identifikační záznam:

OVESNÝ, Martin. Výpočetní metody v jednomolekulové lokalizační mikroskopii. [Computational methods in single molecule localization microscopy]. Praha, 2016. 133 s. Disertační práce (Ph.D.). Univerzita Karlova v Praze, 1. lékařská fakulta, Ústav buněčné biologie a patologie. Vedoucí práce Hagen, Guy.

Acknowledgements

I would like to express my sincere gratitude to my supervisor Dr. Guy Hagen, Ph.D. for the opportunity to participate in the research of super-resolution microscopy and for his guidance in the scientific world. My thanks also belongs to my colleagues from the Institute of Cellular Biology and Pathology, especially to Pavel Křížek, Zdeněk Švindrych, and Josef Borkovec. Above all, I greatly appreciate support and care from my family.

Abstract

Fluorescence microscopy is one of the chief tools used in biomedical research as it is a non invasive, non destructive, and highly specific imaging method. Unfortunately, an optical microscope is a diffraction limited system. Maximum achievable spatial resolution is approximately 250 nm laterally and 500 nm axially. Since most of the structures in cells researchers are interested in are smaller than that, increasing resolution is of prime importance. In recent years, several methods for imaging beyond the diffraction barrier have been developed. One of them is single molecule localization microscopy, a powerful method reported to resolve details as small as 5 nm. This approach to fluorescence microscopy is very computationally intensive. Developing methods to analyze single molecule data and to obtain super-resolution images are the topics of this thesis.

In localization microscopy, a super-resolution image is reconstructed from a long sequence of conventional images of sparsely distributed single photoswitchable molecules that need to be systematically localized with sub-diffraction precision. We designed, implemented, and experimentally verified a set of methods for automated processing, analysis and visualization of data acquired by single molecule localization microscopy and we "packaged" them as an open source software called ThunderSTORM. ThunderSTORM has become one of the top softwares in the field.

Next, we introduce our design for a novel dual-objective super-resolution microscope, which roughly doubles the count of collected photons. This further improves achievable resolution by a factor of $\sqrt{2}$. We built a working prototype of the microscope and developed and experimentally verified methods for calibration of the microscope and for image analysis.

In the last part of the thesis we address the issue that despite the high spatial resolution of localization microscopy it is not always suitable for live cell imaging due to its limited temporal resolution. One strategy is to increase the density of photoactivated molecules present in each image. Such an approach poses a challenge for the image analysis. We present 3denseSTORM, a new algorithm which is able to recover 2D or 3D super-resolution images from a sequence of diffraction limited images with high densities of photoactivated molecules. The algorithm utilizes methods from compressed sensing and uses a Poisson noise model, which becomes critical in low-light conditions. We derive the theoretical resolution limits of the method and show examples of image reconstructions in 2D and 3D simulations and in real data of biological samples. The method is suitable for fast image acquisition in densely labeled samples and helps facilitate live cell studies with single molecule localization microscopy.

Keywords

Super-resolution microscopy, single-molecule localization microscopy, image processing, numerical optimization, sparse representations.

Abstrakt

Fluorescenční mikroskopie je jedním z hlavních nástrojů biomedicínského výzkumu díky tomu, že se jedná o neinvazivní nedestruktivní a vysoce specifickou zobrazovací metodu. Bohužel optický mikroskop je difrakčně limitovaný systém, což znamená, že nejvyšší dosažitelné rozlišení je přibližně 250 nm laterálně a 500 nm axiálně. Jelikož většina buněčných struktur, o které se výzkumníci zajímají, je menší, zvýšení rozlišovací schopnosti je velice důležité. V posledních letech bylo vyvinuto několik metod, které umožňují zobrazování za hranicí difrakce. Jednou z nich je jednomolekulová lokalizační mikroskopie, která dokáže rozlišit detaily až do 5nm. Tato metoda je však velmi výpočetně náročná. Vývoj metod pro zobrazování a analýzu dat z jednomolekulové lokalizační mikroskopie je předmětem této práce.

V lokalizační mikroskopii je obraz se superrozlišením zrekonstruován z dlouhé sekvence konvenčních obrázků jednotlivých řídce distribuovaných fotoaktivovaných molekul. Ty jsou systematicky lokalizovány se subdifrakční přesností. V této práci jsme navrhli, implementovali a experimentálně ověřili sadu metod pro automatické zpracování, analýzu a vizualizaci dat pořízených jednomolekulovou lokalizační mikroskopií. Tyto metody jsou dostupné ve formě otevřeného softwaru, který jsme nazvali ThunderSTORM. ThunderSTORM se stal jedním z předních softwarů v této oblasti.

Dále představujeme náš návrh nového dvouobjektivového mikroskopu schopného superrozlišení, který zhruba zdvojnásobuje počet detekovaných fotonů. To dále zvyšuje dosažitelné rozlišení násobkem $\sqrt{2}$. Sestavili jsme funkční prototyp tohoto mikroskopu. Dále jsme vyvinuly a experimentálně ověřili metody pro kalibraci a pro analýzu obrazu z tohoto mikroskopu.

V poslední části této práce se zaměřujeme na to, že navzdory vysokému prostorovému rozlišení lokalizační mikroskopie, není tato metoda vždy vhodná pro zobrazování živých buněk z důvodu své špatné rozlišovací schopnosti v čase. Jednou ze strategií je zvýšit hustotu fotoaktivovaných molekul v každém obrázku. Nicméně takový přístup představuje další výzvu při analýze obrazu. Zde prezentujeme 3denseSTORM, nový algoritmus, který je schopný zrekonstruovat 2D nebo 3D obrazy se superrozlišením ze sekvence difrakčně limitovaných obrázků s vysokou hustotou fotoaktivovaných molekul. Tento algoritmus využívá metody komprimovaného snímání a používá Poissonův model šumu, což je velmi důležité v temných podmínkách. Odvodili jsme teoretický limit rozlišení této metody a ukázali obrazové rekonstrukce 2D a 3D dat pořízených simulací i snímáním reálných biologických vzorků. Vyvinutá metoda je vhodná pro rychlou akvizici obrázků hustě označkovaných biologických vzorků, což zlepšuje možnosti studovat živé buňky pomocí jednomolekulové lokalizační mikroskopie.

Klíčová slova

Mikroskopie se superrozlišením, jednomolekulová lokalizační mikroskopie, zpracování obrazu, numerická optimalizace, řídké reprezentace.

Table of contents

List of figures

List of tables

Notation

Scalars, sets, tuples, vectors, and matrices

x	scalar
$\{a, b, c\}$	an unordered set
(x, y, z)	ordered n-tuple (3-tuple in this case)
$\boldsymbol{x} = [x_1, x_2, \ldots, x_n]^\top$	column vector with n entries, $i = 1, 2, \ldots, n$
$X = [\boldsymbol{x}_1, \boldsymbol{x}_2, \ldots, \boldsymbol{x}_m]$	$m \times n$ matrix
$X(x, y)$	element of the matrix X at the (x, y) position
$0_{m \times n}$	$m \times n$ zero matrix

General mathematical symbols, variables and operations

$r \in \mathbb{R}, z \in \mathbb{Z}_{>0}$	r is a real number and z is a positive integer
$\lfloor \cdot \rfloor$	round down to integer ("floor")
$\lceil \cdot \rceil$	round up to integer ("ceiling")
$\mathrm{f}(a \mid b)$	function of the variable a given the parameters b
$a \bmod b$	remainder after integer division of a by b
$\max\limits_{x} \mathrm{f}(x) = \{\mathrm{f}(x) \mid \forall y : \mathrm{f}(y) \leq \mathrm{f}(x)\}$	the minimum value of $\mathrm{f}(x)$
$\arg\min\limits_{x} \mathrm{f}(x) = \{x \mid \forall y : \mathrm{f}(y) \geq \mathrm{f}(x)\}$	the value of x that yields the minimum of $\mathrm{f}(x)$
$\ln(x)$	natural logarithm of x
$\exp(x) = e^x$	exponential function of x
$\operatorname{erf}(x) = \frac{2}{\sqrt{\pi}} \int_0^x e^{-t^2} \mathrm{d}t$	error function of x
$\operatorname{atan2}(y, x) = 2 \arctan \frac{\sqrt{x^2+y^2}-x}{y}$	two-argument arctangent function
$\operatorname{sgn}(x) = \begin{cases} -1 & \text{if } x < 0 \\ 0 & \text{if } x = 0 \\ 1 & \text{if } x > 0 \end{cases}$	sign function of x

Chapter 1

Introduction

Microscopy is a field of imaging objects or features of interest small enough that are not visible to the naked eye. Microscopes revolutionized biology and they are essential tools used in a variety of fields ranging from material science, forensic sciences to life sciences, medical research and diagnostics. The vast majority of imaging techniques are based on the interaction of an electro-magnetic field with matter. Varying in energy, in microscopy we recognize infrared, light, electron, or x-ray microscopy. Also other methods are known, such as acoustic microscopy, magnetic resonance microscopy, or atomic force microscopy to name a few. In this thesis we concentrate on light microscopy as it provides many powerful features for biomedical research.

A light (or optical) microscope uses a visible light (wavelength approximately 400-700 nm), which makes the technique minimally invasive to biological specimens and thus allows for observation of living organisms. In contrast to imaging within the visible spectrum, infra-red microscopes exhibit worse resolution and there might be issues with heating up the specimen. On the other side of spectrum, imaging with higher energies, such as in electron microscopes, although reaching much higher resolution, the instrumentation becomes very expensive. Also the sample can't be alive, the preparation is much more complicated than for light microscopy and the energies are so high that the imaging is destructive to the sample (Crang, 1988). For these reasons, electron microscopy remains very popular for structural assays and in material science. On the other hand, light microscopes are a firmly established tool for biology and especially for study of living cells.

1.1 Fluorescence microscopy

Light microscopy works on principle of passing visible light transmitted through or reflected from a sample through series of lenses to the observer's eye or alternatively into a digital camera. Many techniques to improve contrast of a transparent specimen have been developed, such as bright field, dark field, cross-polarized light illumination, differential interference contrast, or phase contrast (the invention for which Frits Zernike was awarded by the Nobel Prize for physics in 1953). Since biological samples are mostly transparent, the improvement in contrast is crucial to make sense of acquired images.

Arguably, the single most important invention in modern cell biology was application of fluorescence and phosphorescence in microscopy. In a fluorescence microscope the specimen is illuminated with a light of specific wavelength (energy) which is absorbed by a fluorescent molecule, so called fluorophore (or chromophore). This excites an orbital electron of the molecule to higher quantum state. When the electron relaxes to its ground state a photon of lower energy (longer wavelength) is emitted. Thus the illumination wavelength is always higher then the emission wavelength. This phenomena is well known as Stokes shift and is depicted in Figure 1.1. Note that it not always the case that the relaxation to the ground state occurs through fluorescence. It can also happen that the energy is released in form of vibrations (heat), or it can be released later via phosphorescence, or the energy can be transfered to a second molecule, etc. Also, sometimes when the illumination is intense a single electron can absorb two photons, which can excite the photon to a higher quantum state even though the energy of the photons is lower than would be normally needed for the excitation.

The real power of fluorescence microscopy comes from the great contrast which is unprecedented. Since the majority of biological samples are transparent, it used to be practically impossible to distinguish different parts of the cells by transmission or reflection. But with

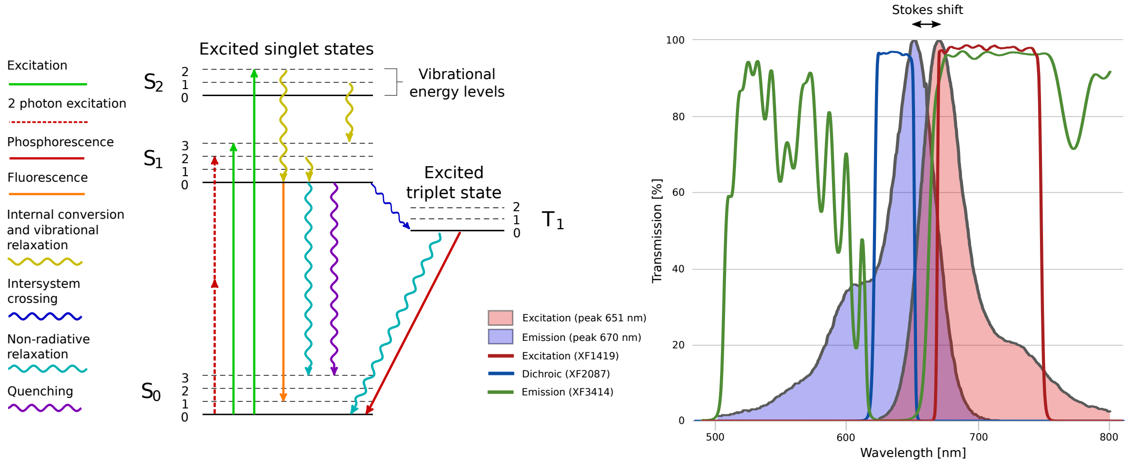

Fig. 1.1 Principle of fluorescence. Left: Jablonski diagram, right: Stokes shift between excitation and emission spectra of Cy5 and transmission characteristics of XF407 filter set[1].

fluorescence, we can label one or more different parts of a cell by different fluorophores with non-overlapping excitation spectra. This way, it is chemically guaranteed that only a particular parts of the cell are observed given the wavelength of illumination. Since birth of fluorescence microscopy, there have been many fluorescent probes discovered with different properties, and excitation/emission spectra. Also many labeling protocols have been developed, thus it is now possible to label virtually anything in any sample (Drummen, 2012). Development of fluorescent probes and labeling protocols is a wide and active area of research (Dempsey et al., 2011; Fernández-Suárez and Ting, 2008; Kobayashi et al., 2010). In 2008, the Nobel Prize for chemistry was awarded to Osamu Shimomura, Martin Chalfie, and Roger T. Tsien for discovery and development of the green fluorescent protein (GFP) and its derivatives.

The most simple setup of a fluorescence microscope is shown in Figure 1.2. Light passes from a source (lamp, laser, light-emitting diode, etc.) through the illumination path (typically a series of lenses, diaphragm, bandpass filter - the setup depends on the type of illumination) and is reflected by a dichroic mirror through an objective into a sample. Some of the light is absorbed by the sample, some is transmitted through and some is reflected back. When absorption occurs, fluorescence is emitted from the sample and is collected by the objective.

---

[1] *Omega Optical - Curvomatic* available at http://www.omegafilters.com/curvomatic/

The emitted light then travels through the dichroic mirror and series of mirrors and lenses to either an eye-piece, or a digital camera. The illumination light that got reflected from the sample back to the objective is filtered by the dichroic mirror, so only emitted light is collected by the detector. Using this setup, we acquire so called *widefield* image.

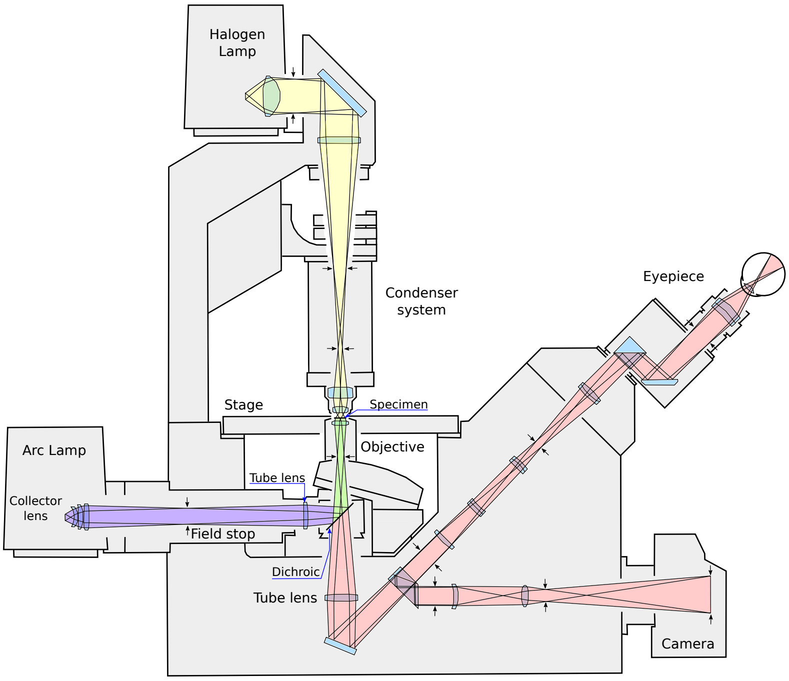

Fig. 1.2 The Zeiss Axiovert 135, an example of epifluorescence microscope setup.

1.2 Diffraction barrier and resolution of light microscope

Despite sophisticated design and fabrication of modern lens components, resolution of optical microscopes is hampered by fundamental limit caused by the wave nature of visible light. As wavefronts pass through a circular aperture at the back focal plane of an objective, diffraction occurs as in Figure 1.3a. In 1873 Ernst Abbe wrote a mathematical formula called the Abbe sine condition (Abbe, 1873) that states the light with wavelength λ traveling in a medium with refractive index n and converging to a spot with angle θ will make a spot with radius

$$d = \frac{\lambda}{2n\sin\theta} = \frac{\lambda}{2\mathrm{NA}}\,. \tag{1.1}$$

Note that $\mathrm{NA} = n \sin\theta$ is known as the numerical aperture and is an important parameter of any objective. Also note that in fluorescence microscopy, λ is the emission wavelength of the light originated in the sample.

The spot created by diffraction is called the point-spread function (PSF), which is the impulse response of the microscope, see Figure 1.3b. An ideal two-dimensional section of the PSF is known as the Airy disk, which is the intensity of Fraunhofer (far-field) diffraction pattern on a circular aperture (Hecht, 2001) and is given by

$$h(\theta) = I_0 \left(\frac{2\mathrm{J}_1(z)^2}{z} \right), \tag{1.2}$$

where I_0 is the maximum intensity of the pattern at the Airy disk center, J_1 is a first order Bessel function of the first kind, and

$$z = \frac{\pi q}{\lambda N}. \tag{1.3}$$

Here λ is wavelength, q is radial distance from the optical axis in the focal plane and $N = R/d$ is the f-number of the system, i.e., ratio of the lens focal length R and the aperture diameter d.

A point object in a microscope, such as a single molecule of a fluorescent protein, generates an image that consists of a diffraction pattern. Neglecting local aberrations, we can assume that a microscope is a linear shift invariant system, thus the shape of PSF remains the same for point objects in different locations in the sample. Then according to Abbe's theory, images are composed from an array of diffraction-limited spots, having varying intensities that overlap to produce the final result. This can be mathematically expressed as

$$\mathrm{i}(x,y,z) = \iiint \mathrm{s}(u,v,w)\mathrm{h}(x-u, y-v, z-w)\, \mathrm{d}u\, \mathrm{d}v\, \mathrm{d}w, \tag{1.4}$$

where the image (stack $\mathrm{i}(x,y,z)$, or a single section $\mathrm{i}(x,y,z=0)$) of the sample produced by an optical microscope is a convolution of the distribution of fluorophores in the specimen $\mathrm{s}(x,y,z)$ and the point spread function $\mathrm{h}(x,y,z)$.

Resolution limit is often defined as the smallest separation distance between two point-like objects in which they can still be distinguished as two individual spots. As a result, most resolution criteria are directly related to the properties of the PSF. Differing in formulation, some of the most common criteria are the Rayleigh criterion (Rayleigh, 1879), the Abbe limit (Abbe, 1873), or the Sparrow limit (Sparrow, 1916), as shown in Figure 1.3c. We usually use the Rayleigh criterion, which states that the lateral and axial resolution is given by $d_{xy} = 0.61\lambda/\mathrm{NA}$ and $d_z = 2\lambda\eta/(\mathrm{NA})^2$, respectively. Here λ is the excitation wavelength and η is the refractive index of the mounting/immersion media.

Practically speaking, for reaching the theoretical resolution limit it is necessary to use a high quality aberration-corrected objective with magnification high enough that the recorded image complies with the Nyquist-Shannon sampling criterion. Also immersion and mounting media with correct refractive index are required to avoid spherical aberrations.

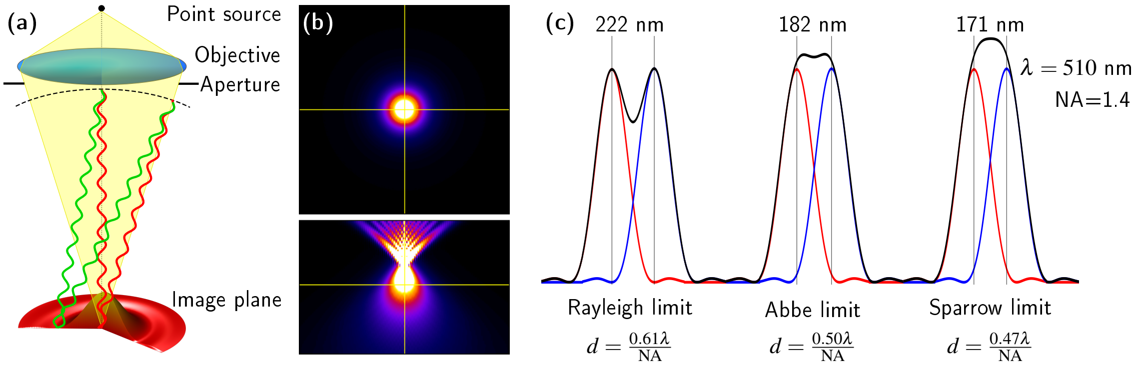

Fig. 1.3 Resolution in a light microscope. (a) diffraction of light, (b) lateral and axial cut through a point spread function (Gibson & Lanni model (Kirshner et al., 2011)), (c) common resolution limits.

1.3 Sectioning methods

In a conventional widefield image the fluorescence emitted by the specimen outside the focal plane interferes with the fluorescence emitted from the focal plane thus reducing resolution of features in the focal plane. Many methods were introduced to deal with this problem and we briefly introduce the most significant of them in the remainder of this section. Note that all these techniques can be (and often are) combined with the super-resolution methods described in Section 1.4.

1.3.1 Total internal reflection

One possible solution to achieve optical sectioning is to use a total internal reflection (TIRF) objective and take advantage of evanescent wave to only excite fluorophores in a thin region of a specimen ($\approx$ 100 nm) (Ambrose, 1956; Axelrod, 1981). This imaging technique is very powerful and is often used to study membrane dynamics, however, one of its disadvantages is that the imaging is confined to a thin interface between two media of dissimilar refractive index. For imaging multiple sections located deeper in the sample, one of the following techniques must be used instead.

1.3.2 Multi-photon illumination

Using the principle of two-photon excitation mentioned in Section 1.1 is the basis for multi-photon microscopy (Göppert-Mayer, 1931). In such microscope a powerful pulsed laser with a longer wavelength is used for illumination. Hence only in the area of focus the illumination is intense enough to excite the fluorophores. This type of microscopy excels in deep tissue imaging (Denk et al., 1990).

1.3.3 Light-sheet illumination

The idea of light-sheet is an extension to the illumination mode of the ultramicroscope, a dark field microscope that applies a thin sheet of illumination light under an angle that is not coincident with angle of an objective. To generate contrast the objective collects only the light scattered from the sample. In 1925 Richard Adolf Zsigmondy was awarded the Nobel Prize in chemistry for the invention of the ultramicroscope. By applying the idea to fluorescence measurements, light-sheet fluorescence microscopy was born. This technique is faster than multi-photon excitation because an entire plane is illuminated, thus doesn't need point-wise scanning across the sample, and unlike TIRF, thick samples can be imaged (Huisken et al., 2004).

1.3.4 Confocal principle

A confocal microscope (Minsky, 1988) uses a pinhole to reject out-of-focus light to improve both lateral and axial resolution. Applying this principle led to invention of Confocal Laser Scanning Microscope (CLSM) (Davidovits and Egger, 1969). It works by focusing light from a laser to a single spot in the sample and then using a set of mutually perpendicular galvanometer mirrors to scan the whole sample. Since the scanning is point-wise a single point detector, such as photo-multiplier tube or avalanche photo-diode, is used to record the fluorescence. Recently, Zeiss came up with a new *Airyscan* CLSM (Weisshart, 2014), which uses a multichannel area detector with 32 elements that provides further improvement $(1.7\times)$ in resolution in all spatial dimensions.

Frame rate is usually a limiting factor of point-wise scanning when observing live samples where rapid changes occur. To address this, spinning disk microscopes were invented (Petráň et al., 1968). The confocal principle applies here as well. A pinhole is replaced by a Nipkow disk that rotates over a sample and as the light passes through the pinholes in the disk a set of points in the sample is recorded simultaneously, which effectively improves speed of the method. A digital camera is used for this kind of scanning. Nowadays, Electron Multiplying Charge Coupled Device (EMCCD) and Scientific Complementary Metal–Oxide–Semiconductor (sCMOS) cameras are the most used matrix detectors for microscopy.

Another well recognized method to apply the confocal principle is Virtual Scanning Microscopy. Here a programmable array microscope is used to replace physical pinholes. As the name suggests a programmable array, such as digital micro-mirror device (Hanley et al., 1999) or liquid-crystal micro-display (Smith et al., 2000), is used to modulate both the illumination and excitation light. Since a digital active matrix is used, the modulation patterns are controlled by a computer and can be easily modified for different scanning strategies (Křížek et al., 2012).

1.4 Imaging beyond the diffraction limit

Fluorescence microscopy has become firmly established as one of the chief tools available for the study of biological systems at the cellular level. Unfortunately, the resolution of fluorescence microscopes is limited due to wave nature of light (Abbe, 1873). As many biological structures within cells are much smaller than this, increasing resolution is of prime importance. Consequently, in last couple of decades the field has been revolutionized and the diffraction barrier has been surpassed by several different techniques (Huang et al., 2009). We list some of these techniques in the following subsections. The most recent trend in super-resolution microscopy is to combine several different principles together to exploit their individual strengths and to minimize their weaknesses.

Imaging beyond the diffraction limit using optical microscopes opens numerous opportunities for biologists to perform analyses that were previously thought impossible. For its great potential super-resolution microscopy was voted for the Method of the Year by Nature Methods journal (Evanko, 2009). In 2014, the Nobel Prize in chemistry was awarded to Eric Betzig, Stefan Hell, and William E. Moerner for the development of super-resolved fluorescence microscopy.

1.4.1 Near-field optical scanning microscopy

Near-field optical scanning microscopy (NSOM) is a super-resolution method which is fundamentally different from the other methods discussed here. This technique works in near-field, that is the detector is placed in distance much smaller than wavelength, and thus exploits properties of evanescent waves. A probe scans the entire sample point-by-point, illuminates a tiny area of the sample, and collects the fluorescent light. Even though this kind of microscope is able to achieve high resolution ($\approx$ 20 nm laterally and $\approx$ 5 nm axially) (Betzig and Trautman, 1992), the working distance and depth of field are very low and scan times are high. These are direct consequences of the underlying principle.

1.4.2 4Pi microscopy

A different principle is exploited in a 4Pi microscope. Here the numerical aperture of an objective is effectively increased by using two opposite objectives focused at the same spot in the sample, thus doubling the observation angle, theoretically up to 4π steradians. Moreover, illumination and detection paths are set up so the light goes through both objectives and lengths of the paths are the same. This implies coherent imaging where both the illuminated spot in the sample and the light emitted by fluorophores is subjected to superposition. A 4Pi microscope achieves $\approx$ 100 nm axial resolution (Hell and Stelzer, 1992). In practice it is difficult to maintain the perfect alignment essential for such microscope to operate.

1.4.3 Structured illumination microscopy

Another method which uses a trick to extend microscope's NA is structured illumination microscopy (SIM). An optical system can be characterized by its optical transfer function (OTF). Note that with knowledge of the PSF, the OTF can be obtained simply as the Fourier transform of the PSF. The OTF describes capability of the system to transfer signals of certain spatial frequencies. Since an objective behaves as a low-pass filter, the OTF has a limited region of support. The idea of SIM is to move high frequency information into the region of support of the OTF. To achieve this, illumination is spatially modulated to obtain a sinusoidal pattern. When the light emitted from the sample passes through the objective, high frequencies are aliased inside the OTF support. If multiple images with different orientation and phase of the illumination pattern are recorded, the high frequency signal can be recovered from the spectra. Then a generalized Wiener filter is applied to combine the low frequency images with the extracted high frequency information and a super-resolution image is produced.

SIM is only capable of improving both lateral and axial resolution by factor of two (Gustafsson, 2000; Gustafsson et al., 2008). Nonetheless, it has been demonstrated that exploiting nonlinearities connected with saturation of the fluorophores, higher order harmonics can be observed in the spectra thus higher frequencies can be extracted (Gustafsson, 2005).

This can yield lateral resolution < 50 nm. However, high power illumination required to achieve saturation can damage the sample. Also to recover the signal modulated on higher harmonics, more images need to be acquired, which hampers frame rate.

1.4.4 Stimulated emission-depletion microscopy

Stimulated emission-depletion microscopy (STED) (Hell and Wichmann, 1994; Klar and Hell, 1999) operates by scanning the sample by an excitation pulse laser followed by a doughnut-shaped STED beam. First, the excitation beam excites the fluorophores which are then stimulated by the STED beam to return to the ground state. As result, only the fluorophores located in the center of the STED beam emit fluorescence. This effectively narrows the PSF, thus increases lateral resolution up to ≈ 20 nm (Westphal and Hell, 2005). Axial resolution is same as in a confocal microscope but it was shown it can be improved to ≈ 30 nm when combined with 4Pi principle (Dyba and Hell, 2002).

Historically, STED microscopy required pulsed lasers that have to be synchronized to alternate the illumination within just hundreds of picoseconds (Dyba and Hell, 2003). This has been recently overcome by using continuous wave lasers in combination with time-gated detection of fluorescence (gCW-STED) (Moffitt et al., 2011; Vicidomini et al., 2011).

Temporal resolution of STED microscopes is limited due to the scanning principle, however, this can be neglected by scanning over smaller regions. Another limiting factor is that high power lasers need to be used which results in photo-bleaching and can even damage the sample. Despite these challenges, it was successfully demonstrated that dynamic processes can be observed using STED (Pellett et al., 2011; Westphal et al., 2008).

1.4.5 Stochastic super-resolution microscopy

It has been discovered that when shinning a powerful source of light on a fluorescent sample, some of the fluorophores can be temporarily turned off to a dark state and later return to an emitting state. Thus, theoretically it would be possible to always activate only a single fluorescent molecule at a subregion of a sample so in the recorded image no two molecules overlap. Therefore, the resolution is no more limited by diffraction. Assuming correct sampling, positions of all molecules in the sample can be recovered with a precision which is only limited only by number of collected photons. More photons mean more accurate localization and consequently higher resolution.

This very principle is the main idea of single molecule localization microscopy (SMLM), which is also known as photo-activated localization microscopy (PALM) (Betzig et al., 2006), fluorescence PALM (fPALM) (Hess et al., 2006), stochastic optical reconstruction microscopy (STORM) (Rust et al., 2006), direct STORM (dSTORM) (Heilemann et al., 2008) and many more. The main difference between the methods is in the principle of activation and deactivation of fluorescent molecules. In real experiments, SMLM methods achieve < 20 nm lateral and < 50 nm axial resolution. Since only a subset of fluorophores is active in a single image, typically thousands frames need to be recorded to reconstruct a single super-resolution image. This negatively affects temporal resolution, which is on the order of few minutes, and makes the method incompatible with live cell imaging. However, recent progress shows that increasing density of photoactivated fluorophores opens possibilities for imaging dynamic processes in living cells (Min et al., 2014b; Ovesný et al., 2014b).

Other methods from the stochastic family, such as Bayesian analysis of blinking and bleaching (3B) (Cox et al., 2012) or super-resolution optical fluctuation imaging (SOFI) (Dertinger et al., 2009; Geissbuehler et al., 2014), estimate the distribution of fluorophores by statistical analysis of their blinking behavior in time rather than frame-by-frame spatial localization. These algorithms allow many molecules to overlap in a single image, hence, achieve better temporal resolution (≈ 5 seconds). Improved temporal resolution comes with the price of worse lateral resolution (≈ 50 nm) and they either can't recover axial position at all, or with a limited accuracy.

1.5 Scope of the thesis

This thesis is concerned with single molecule localization microscopy. SMLM is a super-resolution technique, which typically doesn't require a complicated setup, therefore, it is relatively cheap to acquire and maintain such microscope. The main burden of SMLM is in analysis of acquired images. For this purpose a specialized software is essential. One of the main goals of the project is development of such software to provide a reliable and systematic process of data analysis. Moreover, as mentioned in Section 1.4.5, SMLM suffers with bad temporal resolution. Addressing this issue is the second main goal of the thesis.

In Chapter 2 we introduce SMLM in more detail and briefly review the state of the art in image acquisition and data analysis.

Chapter 3 is all about ThunderSTORM, our solution for SMLM image analysis. We describe some of the most important features available, we evaluate and compare the software to other state of the art methods in the field, and we show some of our published results of real data analyzed with ThunderSTORM.

In Chapter 4 we reveal design of our dual-objective microscope which effectively achieves higher photon detection rates and thus improves localization accuracy in all three dimensions. We also describe and evaluate algorithms for molecule detection used with this setup.

To improve temporal resolution, increasing the density of photoactivated molecules is essential. 3denseSTORM is our algorithm able to analyze such data and is in detail described and evaluated in Chapter 5.

Results of this thesis are concluded in Chapter 6.

Chapter 2

Single molecule localization microscopy

In this chapter we review the concept of single molecule localization microscopy and describe some of the common techniques of 3D imaging used in SMLM. The main focus of the chapter is to introduce the methods we developed and implemented in ThunderSTORM (Ovesný et al., 2014a), a state of the art software for SMLM data analysis and super-resolution imaging, which has become one of the main tools used by researchers in the field.

2.1 A brief review of SMLM

Single-molecule localization microscopy methods have quickly been adopted by many laboratories as a reliable method for achieving optical resolution beyond the diffraction limit. One reason for this rapid dissemination is that the method requires a fairly simple microscope setup, but perhaps more importantly, SMLM methods invite contributions from a variety of disciplines in chemistry and physics, as well as the ultimate applications of SMLM in cell biology. Probe design, labeling strategies, instrumentation development, and image analysis are all part of the process, making SMLM a truly interdisciplinary endeavor.

SMLM methods work by isolating and imaging single molecules in an extended time series. The idea is to, by utilizing one of several possible methods, intentionally photoswitch molecules to an emissive state both infrequently and randomly, such that they can be imaged individually. The imaged molecules are then localized by fitting the imaged Airy patterns to a suitable model. Typically, the localization accuracy achieved is about 20 nm, primarily depending on the number of photons collected from each molecule. Recently two excellent and comprehensive reviews were published, one on localization of single molecules (Deschout et al., 2014), and one on algorithms for data analysis (Small and Stahlheber, 2014).

Beginning in 2006, Betzig and coworkers (Betzig et al., 2006) used the fluorescent proteins Kaede and EosFP to achieve a remarkable result: imaging of cellular structures with a resolution well below the classical limit using genetically-introduced fluorescent probes. Their method, photoactivated localization microscopy (PALM) has subsequently been applied and expanded upon by a number of other research groups. Also in 2006, Hess and coworkers (Hess et al., 2006) showed that photoactivatible GFP (PAGFP) could be used to achieve super-resolution.

More recently, several new fluorescent proteins have been developed aimed at PALM experiments. Today, one of the most commonly used probes in PALM is mEOS2 (McKinney et al., 2009; Wiedenmann et al., 2004), which is photoconvertible. mEOS2 has an absorption maximum of 506 nm, and an emission maximum of 519 nm. After photoconversion using at 405 nm light, the absorption maximum shifts to 573 nm, and the emission maximum shifts to 584 nm. In a typical PALM experiment using mEOS2, a 561 nm laser is used for fluorescence excitation with simultaneous activation with a 405 nm laser at low levels. Sparse subsets of single, isolated mEOS2 molecules are photoconverted to the red form, where they are excited by the higher power 561 nm laser. This results in a short burst of fluorescence from the molecule followed by photobleaching, or possible conversion to a dark state. Under commonly used experimental conditions, the dark state of mEOS2 has been found to have an average lifetime of 4.1 seconds (Durisic et al., 2014). The molecules can then return to an emissive state, resulting in another detectable fluorescence burst.

Another strategy for SMLM was developed in the lab of Xiaowei Zhuang, who showed that pairs of common organic dyes (for example an *activator*, Cy3 and a *reporter*, Cy5) could be used as well, calling their technique stochastic optical reconstruction microscopy (STORM) (Bates et al., 2007; Huang et al., 2008a). In STORM methods, an appropriate laser is used to excite a lower wavelength dye (e.g., 532 nm for Cy3), which can in turn excite a longer wavelength dye (e.g., Cy5).

Working with common, single organic dyes (such as Alexa488, Alexa532, Alexa647, and Cy5), other research groups developed direct STORM (dSTORM) (Heilemann et al., 2008; van de Linde et al., 2008a). This method uses aqueous buffers containing both reducing agents such as mercapto ethylamine (MEA), and an oxygen scavenging system based on the enzymes glucose oxidase and catalase (Uppoor and Niebergall, 1996; van de Linde et al., 2008b). It is also possible to use a buffer system containing ascorbic acid (a reducing agent) and methylviologen (an oxidizing agent), forming a reduction-oxidation system known as ROXS (Vogelsang et al., 2009, 2008). Today, dSTORM in aqueous buffer with MEA and the glucose oxidase-catalase system is probably the most commonly used way to achieve super-resolution.

The use of thiolated reducing agents has been shown to be critical, and a finding from the Zhuang group showed, in a remarkable mass spectrometry experiment, that a reversible thiol-dye adduct is formed, breaking the chromophoric electron structure in Cy5, resulting in a long lived dark state (Dempsey et al., 2009). This experiment was performed using β-mercaptoethanol and Cy5, but it seems likely that this is a general mechanism. More recently, a set of 26 common organic dyes was systematically tested for STORM imaging performance (Dempsey et al., 2011). In a somewhat similar study, a set of 7 photoconvertible or photoactivatible fluorescent proteins were characterized for use in PALM (Durisic et al., 2014). Describing the photophysics of the probes used in SMLM helps further efforts toward quantitative single molecule counting in SMLM experiments.

Working concurrently with the research groups mentioned above, the Cremer group has shown, in papers dating back to 1998 (Bornfleth et al., 1998), that SMLM can be accomplished using conventional GFP (Lemmer et al., 2009) or YFP (Lemmer et al., 2008) with a single laser. Moerner also used conventional YFP (Biteen et al., 2008), based on older observations of GFP and YFP blinking (Dickson et al., 1997; Garcia-Parajo et al., 2000). Our group has successfully used this approach to image erbB3 molecules tagged with the YFP mCitrine (Křížek et al., 2011; Ovesný et al., 2014a).

The early breakthroughs in SMLM were quickly expanded to allow 3D imaging. One possibility is to intentionally introduce astigmatism into the imaging system (using a cylindrical lens positioned inside the microscope or in front of the camera) which can allow axial position determinations (Huang et al., 2008b; Kao and Verkman, 1994). Another possibility is to simultaneously image two separate focal planes in the sample on two separate sectors of a common CCD camera (Juette et al., 2008). There are several other methods which can achieve 3D SMLM, including interferometry (Shtengel et al., 2009), and 4Pi detection (Aquino et al., 2011). Other extensions have included multicolor imaging (Bates et al., 2007; Gunkel et al., 2009; Malkusch et al., 2012; Shroff et al., 2007), imaging live cells (Shroff et al., 2008), anisotropy measurements (Gould et al., 2008), and single particle tracking (Manley et al., 2008; Subach et al., 2010).

2.2 Methods for 3D SMLM imaging

As mentioned above, SMLM allows 3D imaging through variety of techniques. Here we discuss some of these techniques that are arguably used the most due to their relatively cheap and simple setup. All the 3D methods discussed below use the notion of the point spread function (PSF). They exploit the fact the PSF is a function of z-coordinate of an imaged molecule. Thus, axial position the molecule can be determined based on a shape of its image.

2.2.1 Defocus

In a conventional setup, the radius of PSF grows with an increasing axial distance of the imaged molecule from the focal plane ($z = 0$ nm). Note that the intensity profile of a real PSF differs from the ideal Airy shape due to many abberations caused by imperfect lenses and propagation of light through different media (specimen, coverslip, immersion oil). There have been many models derived to capture these phenomena (Kirshner et al., 2013, 2011). Here we use a Gaussian PSF model since it has been previously demonstrated that it is a very good approximation of real PSF of a microscope when dealing with pixelation effects and the presence of noise (Stallinga and Rieger, 2010; Thompson et al., 2002). The Gaussian

PSF model is robust and computationally efficient and is defined by the following equation:

$$\mathrm{h_G}\left(x,y\mid\theta\right)=\frac{\theta_N}{2\pi\sigma\left(\theta_z\right)^2}\exp\left(-\frac{\left(x-\theta_x\right)^2+\left(y-\theta_y\right)^2}{2\sigma\left(\theta_z\right)^2}\right)+\theta_o\,, \tag{2.1}$$

where $\mathrm{h_G}\left(x,y\mid\theta\right)$ returns the photon count at position (x,y) given the parameters $\theta=\left\{\theta_x,\theta_y,\theta_z,\theta_N,\theta_o\right\}$. The entries of θ are as follows: $(\theta_x,\theta_y,\theta_z)$ are the molecular coordinates, θ_N corresponds to the total number of photons emitted by the molecule, and θ_o corresponds to the background offset. Width of the Gaussian $\sigma(\theta_z)$ changes with the axial position θ_z.

Figure 2.1 shows what the sections of the PSF look like when defocusing through an ideal point source. It is obvious that there is no reliable way to distinguish whether a molecule is above or below the focal plane.

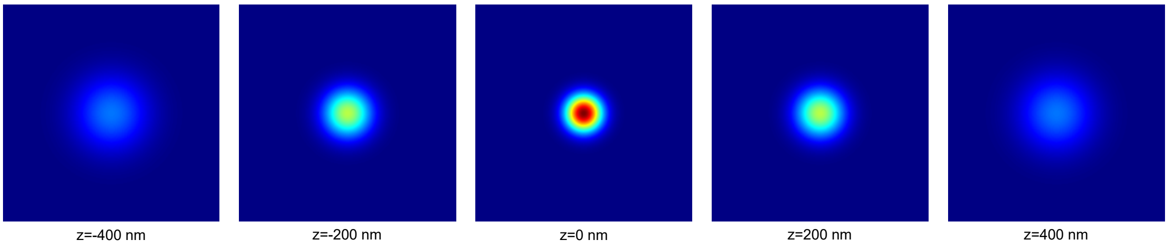

Fig. 2.1 Sections of a plain PSF.

2.2.2 Astigmatism

One possibility to recover 3D position of a molecule is to intentionally introduce slight astigmatism into the imaging system using a cylindrical lens positioned inside the microscope or in front of the camera (Huang et al., 2008b). This results in images of molecules with different ellipticity depending on their axial position. When a molecule is in focus, its image appears round. If the molecule is slightly above or below the focal plane, its image appears ellipsoidal, see Figure 2.2. A common PSF model for astigmatic 3D imaging is an elliptical Gaussian:

$$\mathrm{h_{EG}}\left(x,y\mid\theta,\phi\right)=\frac{\theta_N}{2\pi\sigma_\mathrm{x}\left(\theta_z\right)\sigma_\mathrm{y}\left(\theta_z\right)}\exp\left(-\frac{x'^2}{2\sigma_\mathrm{x}\left(\theta_z\right)^2}-\frac{y'^2}{2\sigma_\mathrm{y}\left(\theta_z\right)^2}\right)+\theta_o\,, \tag{2.2}$$

where

$$\begin{aligned} x' &= (x-\theta_x)\cos\phi - (y-\theta_y)\sin\phi\,, \\ y' &= (x-\theta_x)\sin\phi + (y-\theta_y)\cos\phi\,. \end{aligned}$$

Here $\sigma_x(\theta_z)$ and $\sigma_y(\theta_z)$ are the imaged widths of the molecule along two perpendicular axes rotated by the angle ϕ with respect to xy-axes.

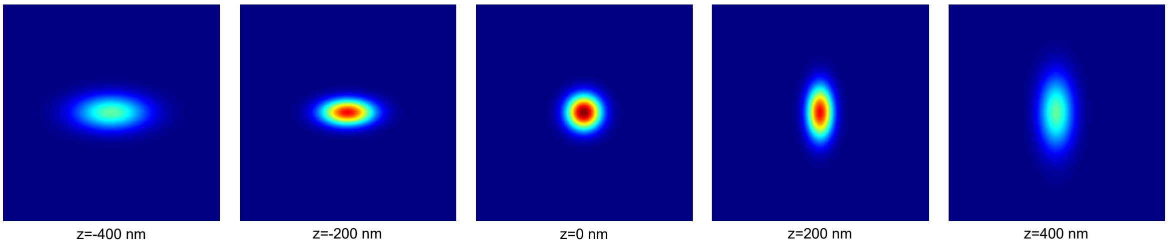

Fig. 2.2 Sections of an astigmatic PSF.

2.2.3 Biplane

Another possibility is to simultaneously image two separate focal planes in a sample on two separate sectors of a common camera (Juette et al., 2008), or alternatively on two different cameras. This is called biplane imaging. There are two approaches to achieve this. The first is to place two objectives on opposing sides of the sample each focused in a slightly different focal plane. The second approach is to use only a single objective, but to split the emitted light with a $50:50$ beam splitter and to lengthen one of the optical paths so as to image two distinct focal planes. Both approaches work on a similar principle, however, the dual objective setup is superior since it collects almost twice as many photons than a single objective setup. We will discuss the dual objective setup in more detail in Chapter 4. The biplane imaging works well with the Gaussian PSF model given by Equation (2.1). Since there are two focal planes imaged simultaneously, the axial coordinate can be precisely recovered, see Figure 2.3. In principle, it is also possible to combine biplane setup with astigmatic imaging by introducing a cylindrical lens into one, or even both, of the detection paths (Min et al., 2014a).

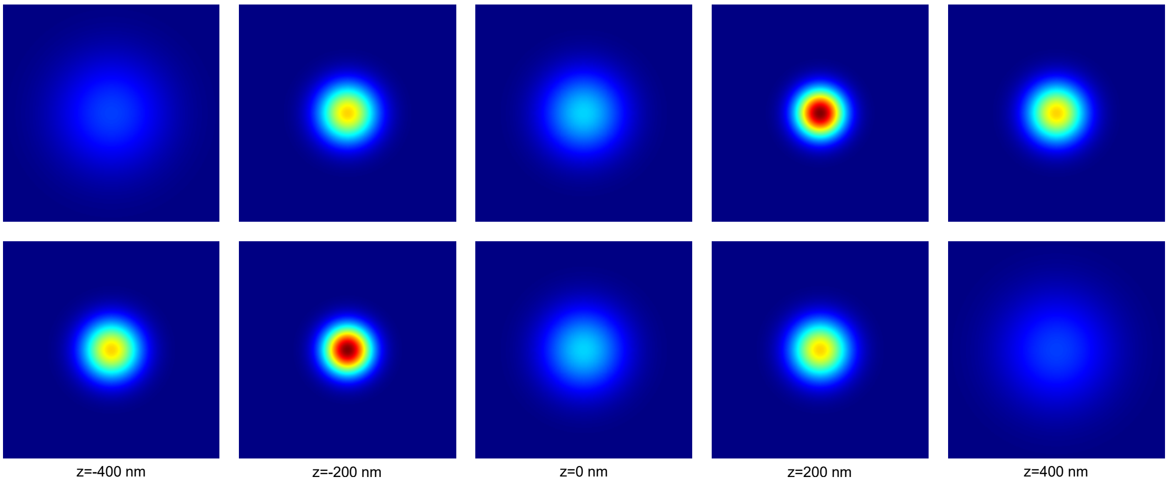

Fig. 2.3 Sections of a biplane PSF.

2.2.4 Double-helix

The last possibility we discuss here is application of rotating PSFs (Pavani and Piestun, 2008; Pavani et al., 2009), also called double-helix point spread functions (DH-PSFs). Rotating PSFs do not change shape as much as they continuously rotate with defocus, see Figure 2.4. This method is a direct application of PSF engineering using phase-shift masks which is loaded in a reflective phase-only spatial-light modulator placed in a Fourier plane of an imaging system. It has been demonstrated that such setup is capable of optimal 3D imaging in terms of the Fisher information (Shechtman et al., 2014). Thus, loading a proper phase-shift mask allows for significantly higher localization accuracy and larger depth of field than astigmatism and biplane methods (Badieirostami et al., 2010). Although an analytic expression of the DH-PSF does not exist, it can be approximated by a double Gaussian function (Lew et al., 2010) written as

$$\begin{aligned} \mathrm{h}_{\mathrm{DH}}(x,y \mid \theta, r) &= \frac{\theta_N/r}{2\pi\sigma_1^2} \exp\left(-\frac{(x-\theta_x-\mu_{\mathrm{x}1}(\theta_z))^2+\left(y-\theta_y-\mu_{\mathrm{y}1}(\theta_z)\right)^2}{2\sigma_1^2}\right) \\ &+ \frac{\theta_N/(1-r)}{2\pi\sigma_2^2} \exp\left(-\frac{(x-\theta_x-\mu_{\mathrm{x}2}(\theta_z))^2+\left(y-\theta_y-\mu_{\mathrm{y}2}(\theta_z)\right)^2}{2\sigma_2^2}\right) + \theta_o\,, \end{aligned} \tag{2.3}$$

where $\{r \in \mathbb{R} \mid 0 < r < 1\}$ is a ratio in which the total number of emitted photons θ_N is divided between the two Gaussians. Note that here σ_1 and σ_2 are constants, while the relative position of the Gaussians $(\mu_{\mathrm{x}1}, \mu_{\mathrm{y}1})$ and $(\mu_{\mathrm{x}2}, \mu_{\mathrm{y}2})$ are functions of axial position θ_z.

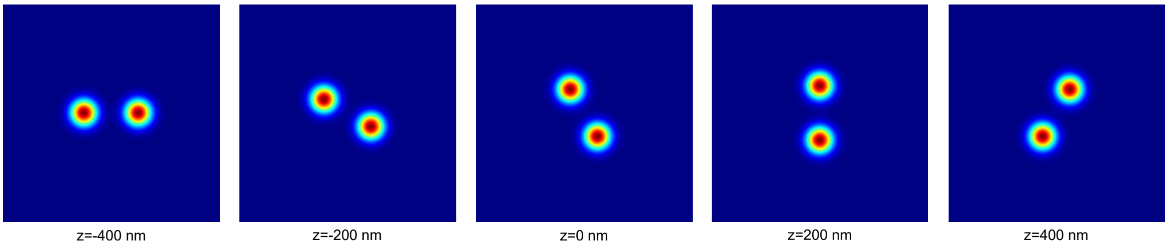

Fig. 2.4 Sections of a double helix PSF.

2.3 SMLM image analysis

In SMLM, a super-resolution image is reconstructed from a sequence of conventional images of sparsely distributed single photoswitchable molecules. Because the image sequence is usually long and the positions of the molecules have to be estimated systematically with sub-diffraction precision, specialized software is required for processing the data. The design, implementation, and evaluation of algorithms for processing SMLM data, and the combination of these algorithms into useful software to create super-resolution images which are informative, accurate, and beautiful has become a field in its own right (Small and Stahlheber, 2014).

SMLM analysis has two stages. First, the raw images are analyzed by image processing algorithms which output a list of molecular coordinates and other parameters such as photon count or localization uncertainty. In the second stage, the list of molecules is taken to be corrected for errors in acquisition, e.g., drift and then further analyzed, e.g., by visual examination of the rendered super-resolution image, or by quantitative evaluation (cluster analysis, co-localization measures, etc.).

Here we discuss various aspects of image processing methods for SMLM, i.e., the first stage. We briefly review some of the software that is currently available and we introduce our own solution. We also discuss how Monte Carlo simulations can be used to evaluate SMLM processing procedures. The issues of the second stage are covered later in Section 2.4.

The traditional approach can be broken down into several steps, shown as a flow chart in Figure 2.5. Below we describe each of the steps in detail.

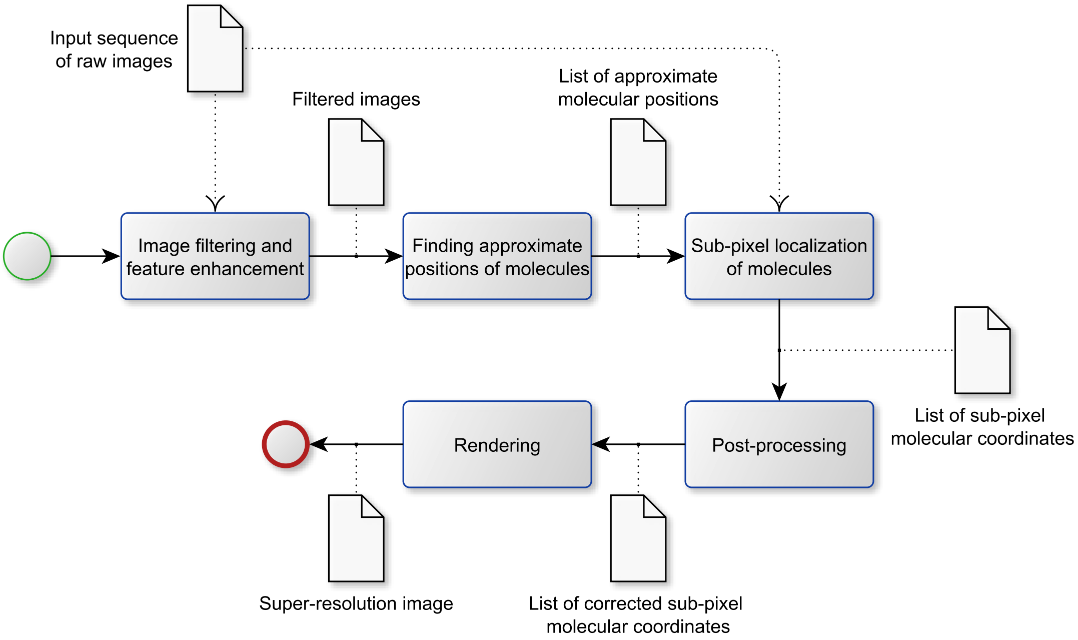

Fig. 2.5 Data analysis steps for single molecule localization super-resolution imaging. The “pages” represent data or images, while the “boxes” represent processing steps carried out by analysis software.

2.3.1 Image filtering for noise reduction and feature enhancement

Image filtering is one of the first steps in many image processing applications. This step helps to identify the molecules in the raw data by reducing noise and enhancing the features we are interested in, see Figure 2.6. In this case, we are interested in point-like signals representing single molecules. Low-pass filters (for example a Gaussian filter or averaging filter) can be used to reduce noise in the image (Křížek et al., 2011). Recently, better results were acquired with band-pass filters, for example with a lowered Gaussian filter as was used in DAOSTORM (Holden et al., 2011), or with a filter based on wavelet transformation (Izeddin et al., 2012).

2.3.2 Thresholding and detection of molecules

Thresholding and detection involves finding the approximate positions of the molecules in the input images while treated by the noise reduction and feature enhancement step described

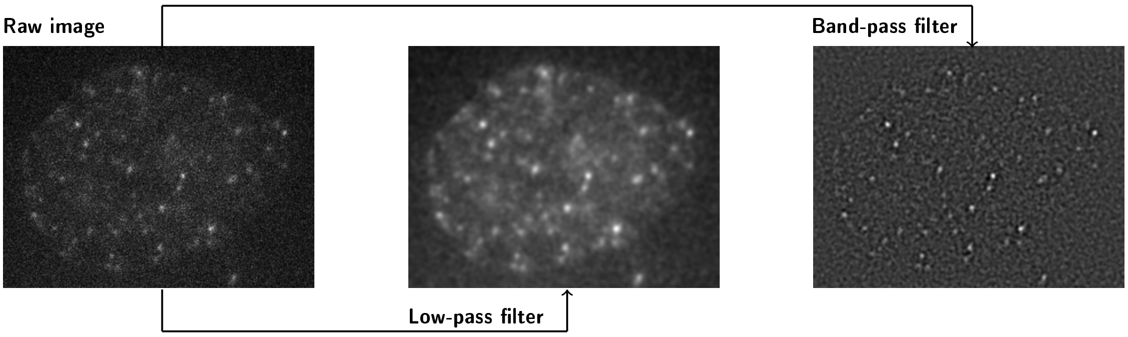

Fig. 2.6 Example of SMLM image filtering.

above, see Figure 2.7. Detection, also known as *spot finding* or *blob detection* is part of the field of feature detection in image processing and has been quantitatively evaluated for single molecule imaging (Ruusuvuori et al., 2010). The question we are asking is “what is a real molecule and what is only noise?” A simple detection of local intensity maxima in an 8-connected neighborhood gives reliable results and is commonly used by SMLM algorithms. The next step is to apply an intensity threshold. This is the most critical step of the analysis. Different methods have been suggested in literature based on estimate of background noise (Henriques et al., 2010; Izeddin et al., 2012; Křížek et al., 2011).

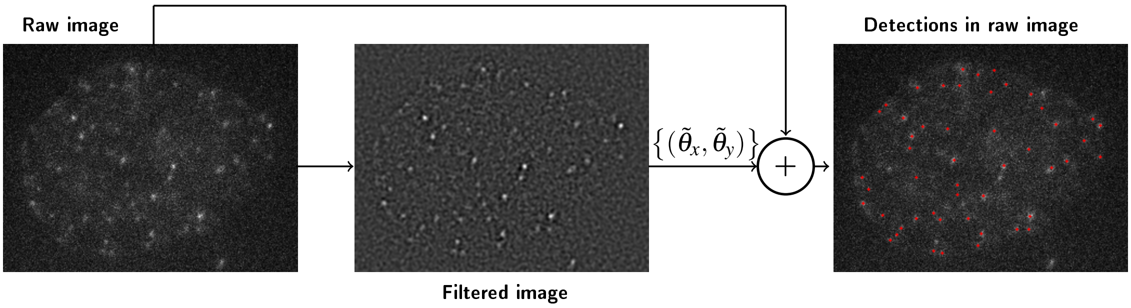

Fig. 2.7 Example of molecule detection. The detection is performed in a filtered image. Then the found positions $\left\{(\tilde{\theta}_x, \tilde{\theta}_y)\right\}$ are “moved” to the raw image for further processing.

A different approach is used in Easy-DHPSF (Lew et al., 2013) which is a software specifically developed for 3D localization using the double-helix method described in Section 2.2.4. Because the DH-PSF is a composition of two spots, the basic spot finding algorithm described above would not work since all spots in the image must be paired to be considered as single molecules. This is achieved through template matching. First, the analyzed image is phase correlated with a model PSF used as a template. Then local maxima are found in the phase correlated image and a threshold is applied. This approach can be generalized to any 3D imaging technique when correlation with multiple sections of 3D PSF is performed. This can be very advantageous since we obtain full three-dimensional estimate of molecular positions, as opposed to a simple spot finding where only lateral positions are estimated.

2.3.3 Sub-pixel localization

Sub-pixel localization of single molecules with an accuracy below the diffraction limit is the basis of SMLM methods and is the factor which produces the super-resolution effect. Prior to super-resolution microscopy, the concept of sub-diffraction localization was used for many years in particle tracking algorithms (Abraham et al., 2009; Chenouard et al., 2014; Daumas et al., 2003; Kusumi et al., 1993; Thompson et al., 2002). There were also several reports using single molecule localization to measure size or distance relationships (Churchman et al., 2005; Gordon et al., 2004; Lemmer et al., 2008; Lidke et al., 2005; Qu et al., 2004; Yildiz et al., 2003). Localization algorithms can be divided into two categories. Fast, non-fitting methods with analytic solutions and slower, generally more accurate methods based on fitting a PSF model using iterative nonlinear optimization.

To localize molecules with sub-pixel precision, after the detection step described above, one needs to create sub-images by cutting out each molecule in a small region of interest. The size of the window should be set proportional to the width of the imaged size of the molecules in the image. Note that in this step the raw input images are used, because a filtered image holds less information.

Non-fitting methods

Calculation of the center of mass in a local image neighborhood is a very fast method for sub-pixel localization of molecules and is used in QuickPALM (Henriques et al., 2010). The main idea is simply to calculate the mean pixel positions weighted by the intensity of the image data. However, the precision of this method is limited.

A more accurate algorithm is known as fluoroBancroft (Sun and Andersson, 2007) and it is implemented in LivePALM (Hedde et al., 2009). The real power of the algorithm is that it can be written down as a single closed-form formula, which makes it much faster then iterative fitting methods, yet the accuracy is better than other non-fitting algorithms (Shen and Andersson, 2011).

Another algorithm finds the sub-pixel position of a molecule by determining the point with maximal radial symmetry in the data as described in (Parthasarathy, 2012) and implemented in (Ma et al., 2012). The general idea is to find the origin of radial symmetry (i.e., the center of a molecule) as the point with the minimum distance to gradient-oriented lines passing through all data points. The calculation of each molecular position is very fast due to an analytical solution. Radial symmetry is a robust feature in SMLM data, making the algorithm resistant to noise. It was demonstrated that the algorithm exhibits a very good precision and is even faster than the fluoroBancroft (Ma et al., 2012).

A template matching approach was applied in palm3d (York et al., 2011). The location of a molecule is determined by finding maximum of sub-pixel cross-correlation of the region of interest with an oversampled model PSF.

Fitting methods

The response of a microscope to a point-like source of light is described by the point spread function (PSF). Because a single molecule emitter can be treated as a point source in SMLM data, the result of fitting a PSF model to an image of a single molecule is an estimate of the sub-diffraction molecular position and its intensity, see Figure 2.8. The most commonly used model is a Gaussian function and its variations listed in Section 2.2. A firmly established representative of a software that utilizes fitting methods is rapidSTORM (Wolter et al., 2012).

To perform the fitting, one can use (weighted) least squares, which assume normally (Gaussian) distributed noise. Maximum likelihood estimation (MLE) assumes a Poission noise model, which more accurately describes the photon counting process dominant in the extreme low light conditions which are present when imaging single molecules (Smith et al., 2010). When using MLE, the pixel values must be expressed in photons, requiring a calibrated camera. With higher photon counts, weighted least squares methods provide a good approximation to the MLE results.

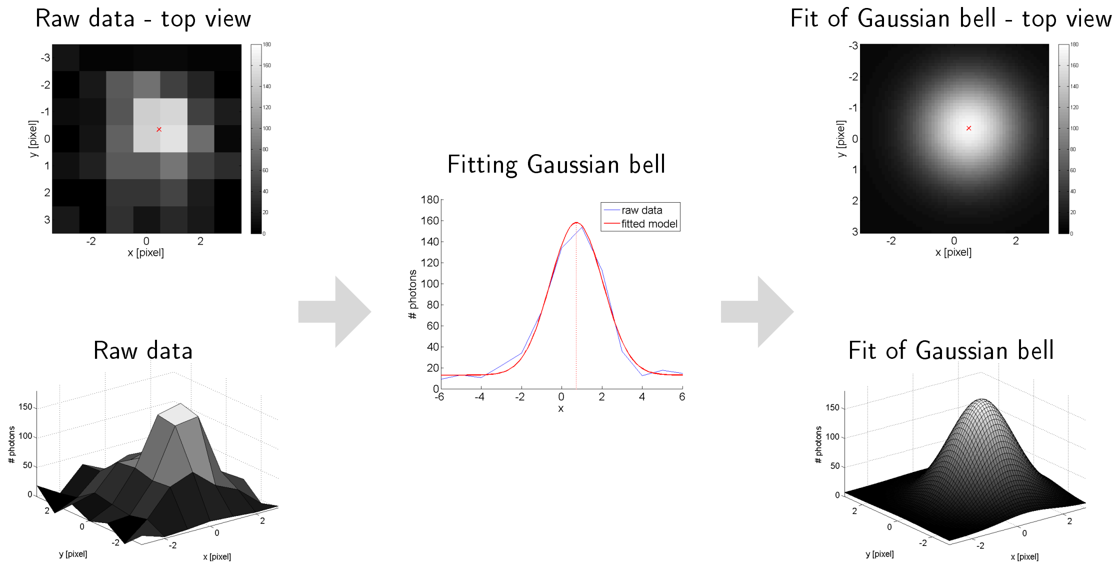

Fig. 2.8 Example of a fitting process.

2.3.4 The *crowded field* problem

A critical requirement on algorithms for sub-pixel localization is that only a single activated molecule is present in the sub-image where the localization is performed. However, high spatial densities of activated molecules can result in a *crowded field* problem, in which single molecules are not adequately resolved. When there are too many photo-activated molecules in a single camera frame, their images start to overlap. Thus a more sophisticated solution is needed.

One approach for solving the high density problem uses multi-emitter fitting (Huang et al., 2011). Here sub-images are fit with multi-modal 2D Gaussian functions. First, the algorithm fits a single molecule. Then PSF of this molecule is subtracted from the raw data and the position of the maximum intensity value in the residual image is taken as an approximate position of a second molecule. The fitting is now repeated on the raw data with two molecules. Again, the result of the fit is subtracted from the raw data to find an approximate position of a third molecule in the residual image. The process is repeated until the number of molecules reaches a user-defined limit. A similar algorithm was also described in (Babcock et al., 2012).

An interesting fact is that in early days of localization microscopy, the *crowded field* problem was an unwanted phenomenon. However, new algorithms that can solve this problem with high accuracy were developed which lead researchers to intentionally increase the density of photo-activated molecules to allow faster data acquisition. We discuss this technique in more detail in Chapter 5.

2.4 SMLM data analysis

Once the initial analysis is complete and we have the coordinates of single molecules, SMLM experiments can be further analyzed in several ways. An obvious option is to render a super-resolution image that can be analyzed visually. However, quantitative methods, such as evaluating co-localization or clustering of molecules, are often required to better analyze the data.

Similarly to the raw image analysis, also this stage of processing requires a systematic approach to the analysis. Again, specialized software is needed, however, this is often not provided by SMLM software and the analysis immediately becomes tedious. One option for researchers is to use a generic software, e.g., Matlab, MS Excel, or Python. Another option is to use some of the pre-written scripts developed for SMLM data analysis, such as PyME[1] or ZhuangLab tools[2]. This is still quite inconvenient since it requires certain skills of working with Python scripts. A much more user-friendly option is to use either PALMsiever (Pengo et al., 2014), or our software - ThunderSTORM (Ovesný et al., 2014a). Both of these have intuitive user interface and are interactive so the user can see results of his actions immediately. We discuss some of the methods implemented in ThunderSTORM in Section 3.8.

---

[1] *Python Microscopy Environment* available at https://bitbucket.org/david_baddeley/python-microscopy

[2] *ZhuangLab tools* available at https://github.com/ZhuangLab

2.5 Experimental evaluation of SMLM algorithms

An integral part of developing a process for SMLM image analysis is a testing in a controlled environment and quantitative evaluation of performance of individual SMLM algorithms. Monte Carlo simulations can be used for this purpose (Křížek et al., 2011). We believe the simulations should be informed by real measurements. For example, how many photons are detected from each molecule? The distribution of molecular photon rates can be measured in a real experiment and that distribution (its shape, mean value, and standard deviation) can be incorporated into the simulation. Similarly, what is the density of photoactivated molecules in each frame? What is the background signal level? What kind of noise is introduced by the camera? Knowledge of these factors help make the simulations realistic.

The basic steps in creating this kind of simulation are as follows: 1) build simulation based on measured values by introducing artificial molecules into a blank image; 2) process the simulated data with the software package of choice using (if possible) a variety of settings for the filtering and detection steps; 3) evaluate the results with respect to detection rate and localization accuracy.

2.6 Chapter summary

In this chapter we briefly reviewed the field of localization microscopy, which has in recent years become one of the chief tools for biologists and one of the most attractive interdisciplinary research area combining efforts from mathematics, physics, chemistry, and biology. State of the art optical elements, photodetectors, data processing methods, labeling protocols, and fluorescent probes are all equally important for achieving high-quality results. We have described the working principle of localization microscopy including multiple methods for extracting information about the 3D position of individual molecules. Moreover, we discussed methods used for image processing and data analysis.

Because this kind of microscopy is computation-heavy, the algorithms for analysis are essential for obtaining any results. This fact sparked research in image processing and data analysis for localization microscopy. In 2013 the SMLM Challenge[3] was held to evaluate and compare state of the art algorithms for SMLM image analysis. We participated in the challenge with our software called ThunderSTORM. Using a quantitative experimental evaluation ThunderSTORM was the best of all submitted software to analyze long image sequences (Sage et al., 2015). Chapter 3 is dedicated to ThunderSTORM. Recently a new SMLM Challenge was announced in 2016[4] to specifically evaluate software with respect to 3D localization accuracy.

---

[3] *SMLM Challenge 2013* available at http://bigwww.epfl.ch/smlm/challenge2013/

[4] *SMLM Challenge 2016* available at http://bigwww.epfl.ch/smlm/challenge2016/

Chapter 3

ThunderSTORM

Our solution for SMLM data analysis is called ThunderSTORM (Ovesný et al., 2014a). ThunderSTORM is open-source, interactive, modular software, which provides a complete set of tools for automated processing, visualization, simulation, and quantitative analysis of data acquired by SMLM methods including STORM, dSTORM, SPDM, PALM, and fPALM. The software is distributed as an ImageJ plugin (Abramoff et al., 2004), can run on computers with different operating systems, supports the ImageJ macro language, and is also compatible with other ImageJ-based applications such as Fiji (Schindelin et al., 2012) or μManager (Edelstein et al., 2010). ThunderSTORM was developed using a home-built SMLM system, but the software has been tested, and works well with data acquired using commercially available Nikon N-STORM and Zeiss Elyra systems, and offers several unique capabilities compared to the analysis packages offered by these companies. Our philosophy in developing ThunderSTORM has been to offer an extensive collection of processing and post-processing methods which were developed based on extensive testing with both real and simulated data. We also provide a very detailed description of the implemented methods and algorithms as well as a detailed user's guide. ThunderSTORM and the documentation is available at the project website https://github.com/zitmen/thunderstorm/.

When processing data using ThunderSTORM, we typically recommend use of the default settings (wavelet based filtering and thresholding, detection of local maxima, and PSF fitting by maximum likelihood methods using a Gaussian PSF model), which in our hands produced good results on many datasets acquired with dSTORM and PALM protocols. However, experienced users may process the data using any combination of the implemented analysis methods. Each possible combination represents an algorithm for detection of molecules in the raw data. Many of these algorithms have not been reported in the literature as unique solutions and are therefore novel in ThunderSTORM. Moreover, some of the existing software solutions for SMLM data analysis offer little or no details about how or even whether these critical steps are performed. A feature exclusively unique to ThunderSTORM is the possibility to specify the threshold for detection of molecules using a mathematical expression. This allows computing the threshold value systematically for unknown input images, where the global intensity may slowly fluctuate.

ThunderSTORM is also capable of generating a sequence of SMLM-like images in which the ground-truth positions of the molecules are known. This allows users to perform Monte Carlo simulations (Křížek et al., 2011), and to quantitatively evaluate the performance of applied localization algorithms by calculating, e.g., the Jaccard index or F1 score. In addition to the image size and sequence length, users can specify the intensity, imaged size, and spatial density of the generated molecules. The resulting images can be subjected to sample drift. Noise in the generated images can simulate the behavior of CCD or EMCCD cameras.

In the remainder of this section we describe the image analysis in more detail. Although ThunderSTORM offers many different methods, here we do not describe all of them, since the comprehensive documentation is available directly in the software and at the project website.

3.1 Step 1: Image filtering and feature enhancement

ThunderSTORM provides several low-pass and band-pass convolution-based image filters. Users may also choose not to use a filter and leave the input data as it is for further processing. The default option in ThunderSTORM is a wavelet filter.

Input: A raw image I of size $m \times n$ pixels.

Output: A filtered image F of size $m \times n$ pixels.

Convolution A two-dimensional discrete convolution is defined as

$$(I * K)(x,y) = \sum_{-\infty}^{+\infty} \sum_{-\infty}^{+\infty} I(u,v) K(x-u, y-v) , \tag{3.1}$$

where I is an image of size $m \times n$, and K is a convolution kernel of arbitrary size. Values outside the domains of I and K are set to zero.

Convolution can be a time demanding operation when implemented according to the definition in Equation (3.1). To speed up the algorithms, we use a method known as convolution with separable kernels. This allows one to calculate the convolution of the image I with the kernel K as

$$F = I * K = (I * \boldsymbol{k}) * \boldsymbol{k}^{\top} \tag{3.2}$$

if the kernel K can be written as $K = \boldsymbol{k}\boldsymbol{k}^{\top}$. Here the kernel K is an $l \times l$ matrix and $\boldsymbol{k} = [k_1, k_2, \ldots, k_l]^{\top}$. Using the method of separable kernels reduces the time complexity of the convolution from $\mathcal{O}\left(mnl^2\right)$ to $\mathcal{O}(mnl)$.

Wavelet filter The wavelet transform is commonly used in modern signal-processing applications. This type of wavelet filter applies the *à trous* algorithm (Izeddin et al., 2012; Starck and Murtagh, 2002) which is an undecimated scheme in which the filter responses are up-sampled, thereby inserting holes (*trous* in French) between the filter coefficients. The output of each filter level, therefore, contains the same number of samples as the input.

The wavelet transform of the input data at level $j = 1, \ldots, N$ is computed as

$$F_j = V_{j-1} - V_j , \tag{3.3}$$

where

$$V_j = \left(V_{j-1} * \boldsymbol{k}_j\right) * \boldsymbol{k}_j^{\top} . \tag{3.4}$$

Here $V_0 = I$ is the input image, $\boldsymbol{k}_j$ is a filter kernel at the corresponding level, and l is the kernel size. The number of levels is given by N.

The expression in Equation (3.3) acts as a band-pass filter. Each wavelet level thus corresponds to a different range of spatial frequencies. The first level F_1 contains mainly the high spatial frequencies present in the input image including noise. Higher levels contain ranges of lower and lower image frequency components. In our case, the output of the wavelet filter is the second wavelet level F_2. The standard deviation of values obtained in the first wavelet level F_1 can be used as a molecular detection threshold in the filtered image (Izeddin et al., 2012), see Section 3.2.

The wavelet filter typically uses a convolution kernel based on normalized B-spline basis functions (Izeddin et al., 2012; Starck and Murtagh, 2002). In our case, the B-spline basis function of order $q \in \mathbb{Z}_{>0}$ in the variable $t \in \mathbb{R}$, written as $\mathrm{B}_q(t)$, is defined recursively as follows. For $q = 1$,

$$\mathrm{B}_1(t) = \begin{cases} 1 & \text{if } 0 \leq t < 1\,, \\ 0 & \text{otherwise}\,, \end{cases} \tag{3.5}$$

and for $q > 1$,

$$\mathrm{B}_q(t) = \frac{t}{q-1}\mathrm{B}_{q-1}(t) + \frac{q-t}{q-1}\mathrm{B}_{q-1}(t-1)\,. \tag{3.6}$$

Here $\mathrm{B}_q(t)$ has non-zero values only in the interval $0 \leq t < q$.

The first wavelet level F_1 is computed using the convolution kernel $\boldsymbol{k}_1 = \left[k_{1,1}, \ldots, k_{1,l}\right]$, where $k_{1,i} = a\mathrm{B}_q\left(\frac{x}{s} + \frac{q}{2}\right)$, $i = 1, \ldots, l$, $x = i - (l+1)/2$, and $l = 2\left\lceil\frac{qs}{2}\right\rceil - 1$. Here $s > 0$ defines a scaling factor of the variable x, and a is a scaling factor such that $\sum_i k_{1,i} = 1$. Kernels for higher wavelet levels are obtained by inserting zeros between the kernel coefficients. Users need to input the order q of the B-spline basis function and the scaling factor s.

In our implementation, the default kernel uses a B-spline basis function of the third order with a scaling factor $s = 2$. These settings yield kernels $\boldsymbol{k}_1 = \left[\frac{1}{16}, \frac{1}{4}, \frac{3}{8}, \frac{1}{4}, \frac{1}{16}\right]^\top$ and $\boldsymbol{k}_2 = \left[\frac{1}{16}, 0, \frac{1}{4}, 0, \frac{3}{8}, 0, \frac{1}{4}, 0, \frac{1}{16}\right]^\top$, as suggested in (Izeddin et al., 2012; Starck and Murtagh, 2002). Examples of kernels based on B-spline basis functions are shown in Figure 3.1.

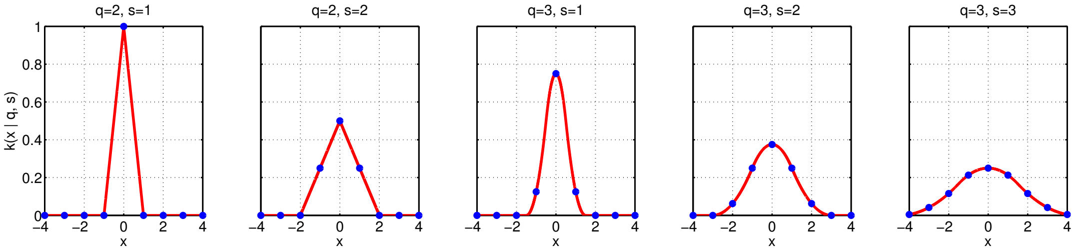

Fig. 3.1 Examples of convolution kernels generated with B-spline basis functions. Blue points correspond to sampling of the B-spline basis function (in red).

3.2 Step 2: Finding approximate positions of molecules

Finding approximate positions of the molecules in the input images follows the image filtering and feature enhancement step described above. ThunderSTORM offers three algorithms for this purpose: detection of local intensity maxima, non-maximum suppression (also called *maxima filter*), or calculation of the centroid of connected components of segmented objects. All three methods need a user-specified threshold defining an intensity below which possible molecular detections will be rejected. The default detector used in ThunderSTORM is a non-maximum suppression with 3 × 3 square kernel, which is an equivalent of finding a local maxima in an 8-connected neighborhood. Although they produce exactly same results, we prefer the more general formulation by non-maximum suppression because it can be simply modified just by changing size of the kernel, which is advantageous for example when analyzing images of large beads or when pixel-size is small.

Input: A filtered image F of size $m \times n$ pixels.

Output: A list of coordinates $\left\{ \left(\tilde{\theta}_x, \tilde{\theta}_y\right) \right\}$ with approximate molecular positions.

Non-maximum suppression

Our implementation of non-maximum suppression is based on morphological gray-scale dilation (Šonka et al., 2007) defined by the formula

$$(F \oplus S)(x,y) = \max_{(x',y') \in D_S} \left\{ F\left(x-x', y-y'\right) + S\left(x',y'\right) \right\} , \tag{3.7}$$

where F is the filtered image, S is a structuring element (or kernel), and D_S is the domain of S. Note that the structuring element can have an arbitrary form.

Threshold selection

When finding the approximate position of molecules, choosing the right threshold value is critical for obtaining good results, because the threshold influences the number of missed molecules (false negatives) and the number of erroneous detections of non-existing molecules (false positives). ThunderSTORM uses a single-valued intensity threshold which is updated for every raw input image I and applied to the filtered image F. The threshold value can be specified by users as an expression combining mathematical functions and operators with variables based on the current raw or filtered image. This is a powerful option, because users can specify the threshold value systematically for unknown input images, in which the global intensity may slowly fluctuate over time. In (Izeddin et al., 2012) authors suggested to use the second wavelet level F_2 as the filtered image F and to choose the threshold value between 0.5 and 2 times the standard deviation of the intensity values from the first wavelet level F_1, see Section 3.1 for the definition of wavelet levels. Thus the default value of threshold used in ThunderSTORM is `std(Wave.F1)` (consult the project website for full description of syntax for thresholding).

3.3 Step 3: Sub-pixel localization of molecules

Sub-pixel localization of single molecules with an accuracy below the diffraction limit is the basis of SMLM methods. ThunderSTORM supports the following localization methods: calculation of the centroid of the local neighborhood (Henriques et al., 2010), the radial symmetry method (Parthasarathy, 2012), and fitting of point spread function models by (weighted) least-squares methods or by maximum likelihood estimation (Kendall and Stuart, 1979; Mortensen et al., 2010). Users may also choose not to use any of the methods, thereby using the approximate positions of the molecules determined in the previous step. Note that the choice of method for sub-pixel localization of molecules is independent of the pre-processing methods described above. The default option in ThunderSTORM is fitting of PSF model by one of weighted least squares or maximum likelihood methods.

Input: A raw image I of size $m \times n$ pixels and a list of coordinates $\left\{ \left(\tilde{\theta}_x, \tilde{\theta}_y \right) \right\}$ with approximate molecular positions.

Output: A list of coordinates $\left\{ \left(\hat{\theta}_x, \hat{\theta}_y \right) \right\}$ with sub-pixel positions of the molecules.

Fitting point-spread function models

The impulse response of a microscope to a point-like source is described by the point-spread function (PSF). Because a single molecule emitter can be treated as an incoherent point source in SMLM data, the result of fitting a PSF model to an image of a single molecule is an estimate of the molecular position, its imaged size, and its intensity. Common PSF models used by different imaging techniques are listed in Section 2.2. ThunderSTORM offers a choice between several PSF models and fitting procedures based on (weighted or unweighted) least-squares methods and maximum likelihood estimation (Kendall and Stuart, 1979; Mortensen et al., 2010). For 2D analysis we use a Gaussian PSF model $\mathrm{h_G}(x,y \mid \theta)$ defined in Equation (2.1). For 3D analysis ThunderSTORM supports biplane and astigmatic imaging with an elliptic Gaussian PSF model $\mathrm{h_{EG}}(x,y \mid \theta, \phi)$ defined in Equation (2.2). Since specification of an estimation algorithm is independent of the PSF model used, in the following paragraphs we define $\mathrm{h}(x,y \mid \theta)$ as a placeholder PSF which can be substituted for a specific PSF model.

Definition of the fitting region Given the approximate position of a molecule $\left(\tilde{\theta}_x, \tilde{\theta}_y\right)$ and a user-specified fitting "radius" $r > 0$, we define domain

$$\mathscr{D} = \left\{ (x,y) \mid x \in \left\{ \tilde{\theta}_x - r, \ldots, \tilde{\theta}_x + r \right\}, y \in \left\{ \tilde{\theta}_y - r, \ldots, \tilde{\theta}_y + r \right\} \right\} . \tag{3.8}$$

Least-squares methods To approximate the data with a point-spread function, least-squares methods (Bevington and Robinson, 2003; Kendall and Stuart, 1979; Mortensen et al., 2010) are employed to minimize the sum of (weighted) squared residuals defined by

$$\chi^2(\theta \mid \mathscr{D}) = \sum_{(x,y)\in\mathscr{D}} \mathrm{w}(x,y)\left(I(x,y) - \mathrm{h}(x,y \mid \theta)\right)^2 . \tag{3.9}$$

Here the residual value for the (x,y) data point is defined as the difference between the observed image intensity $I(x,y)$ and the value approximated by the $\mathrm{h}(x,y \mid \theta)$, where θ are the PSF parameters. The residual value can be further weighted by $\mathrm{w}(x,y) = 1$, making all measurements equally significant, or weighted by $\mathrm{w}(x,y) = 1/I(x,y)$, which takes into account the uncertainty in the number of detected photons.

The search for parameters $\hat{\theta}$ which minimize $\chi^2(\theta \mid \mathscr{D})$, leads to an optimization problem formulated as

$$\hat{\theta} = \arg\min_{\theta} \chi^2(\theta \mid \mathscr{D}) , \tag{3.10}$$

which we solve by the Levenberg-Marquardt algorithm as implemented in the Apache Commons Math library. The starting point for the optimization process is computed from the data in the fitting region as the difference between the maximum and the minimum intensity values for the molecular intensity θ_N, and as the minimum intensity value for the background offset θ_o. The initial position is $\theta_x = \tilde{\theta}_x$, $\theta_y = \tilde{\theta}_y$, and $\theta_z = 0$.

Maximum-likelihood estimation This approach assumes that the number of photons collected by a single camera pixel follows the Poisson distribution. Thus, the probability of κ photons arriving at a camera pixel, where the expected number of photons is λ, is given by

$$p(\kappa \mid \lambda) = \frac{\lambda^{\kappa} \exp(-\lambda)}{\kappa!} . \tag{3.11}$$

Suppose that samples are drawn independently from the Poisson distribution, with the expected photon count $\lambda = \mathrm{h}(x,y \mid \theta)$ given by the point-spread function model, and the observed photon count $\kappa = I(x,y)$ given by the image intensity expressed in photons. The likelihood (Huang et al., 2011; Kendall and Stuart, 1979; Mortensen et al., 2010; Smith et al.,

2010) of the parameters θ can be modeled as

$$\mathcal{L}(\theta \mid \mathscr{D}) = \prod_{(x,y)\in\mathscr{D}} \frac{\mathrm{h}(x,y \mid \theta)^{I(x,y)} \exp\left(-\mathrm{h}(x,y \mid \theta)\right)}{I(x,y)!}. \tag{3.12}$$

The maximum likelihood estimate of the parameters θ is, by definition, the value that maximizes the likelihood $\mathcal{L}(\theta \mid \mathscr{D})$. Intuitively, the estimate $\hat{\theta}$ corresponds to the value θ that best agrees with the data. After simplification by applying the natural logarithm, the maximization problem has the form of

$$\hat{\theta} = \arg\max_{\theta} \sum_{(x,y)\in\mathscr{D}} \left\{ I(x,y) \ln\left(\mathrm{h}(x,y \mid \theta)\right) - \mathrm{h}(x,y \mid \theta) \right\}, \tag{3.13}$$

which we solve by the Nelder-Mead method (O'Neill, 1971). The starting point for the optimization process is computed from the data in the fitting region as the difference between the maximum and the minimum intensity values for the molecular intensity θ_N, and as the minimum intensity value for the background offset θ_o. The initial position is $\theta_x = \tilde{\theta}_x$, $\theta_y = \tilde{\theta}_y$, and $\theta_z = 0$.

Constraining parameters of PSF models The Levenberg-Marquardt algorithm and the Nelder-Mead method both search for values of the parameters θ over an infinite interval. The optimization process can therefore converge to a solution with negative values which is impossible for variables corresponding to image intensity or to the background offset. We therefore limit the interval of possible values by transforming the relevant parameters and using $\mathrm{h}\left(x,y \mid \bar{\theta}\right)$ in Equations (3.10) and (3.13) instead of $\mathrm{h}(x,y \mid \theta)$. The transformation for a 2D Gaussian PSF model is $\bar{\theta} = \left\{\theta_x, \theta_y, \theta_z, \theta_N^2, \theta_o^2\right\}$. The optimization process is still unconstrained but will result in positive PSF parameters.

Localization uncertainty In ThunderSTORM the localization uncertainty is calculated for each molecule to provide a piece of information upon which the user can determine whether the molecule should be considered in the final result, or not. The uncertainty is derived from the Cramer-Rao lower bound (CRLB), which is the lower bound for variance of an unbiased estimator.

Let $\hat{\theta}_\sigma$ be the standard deviation of a fitted Gaussian PSF in nm, a is the backprojected pixel size in nm, $\hat{\theta}_N$ is estimate of the number of photons detected for a given molecule, and $\hat{b}$ is the background signal level in photons calculated as the standard deviation of the residuals between the raw data and the fitted PSF model. The uncertainty of least-squares or maximum-likelihood estimates of the lateral position of a molecule is estimated as

$$\begin{aligned} (\Delta\hat{\theta}_{xy})^2\big|_{\mathrm{LSQ}} &= \tfrac{g\hat{\theta}_{\sigma^2}+a^2/12}{\hat{\theta}_N}\left(\tfrac{16}{9}+4\tau\right) , \\ (\Delta\hat{\theta}_{xy})^2\big|_{\mathrm{MLE}} &= \tfrac{g\hat{\theta}_{\sigma^2}+a^2/12}{\hat{\theta}_N}\left(1+4\tau+\sqrt{\tfrac{2\tau}{1+4\tau}}\right) , \end{aligned} \tag{3.14}$$

respectively. Here

$$\tau = \frac{2\pi(\hat{b}^2+r)(\hat{\theta}_\sigma^2+a^2/12)}{a^2\hat{\theta}_N} . \tag{3.15}$$

The uncertainty for least-squares estimate is also known as the Thompson-Larson-Webb formula (Thompson et al., 2002), which has been modified with the correction factor of $\frac{16}{9}$ as suggested by (Mortensen et al., 2010). The uncertainty for maximum-likelihood was derived in (Rieger and Stallinga, 2014). Finally, the compensation for readout noise r and EM gain g has been added by following (Quan et al., 2010), who suggested that when using EMCCD cameras, the correction factors should be set to $r = 0$, $g = 2$ and when using CCD or sCMOS cameras the readout noise in electron counts should be set to $r = g = 2$.

3.4 Additional steps involved in 3D localization

ThunderSTORM supports 3D localization of molecules using the astigmatic imaging approach introduced by (Huang et al., 2008b), who used the elliptic Gaussian PSF model $\mathrm{h}_{\mathrm{EG}}(x,y \mid \theta,\phi)$ defined in Equation (2.2).

Recall that in a PSF model based on a Gaussian function its imaged width $\sigma(\theta_z)$ depends on the z-coordinate. Obviously an elliptic Gaussian has two perpendicular axes, therefore, also two widths $\sigma_{\mathrm{x}}(\theta_z)$ and $\sigma_{\mathrm{y}}(\theta_z)$. The relationship between the axial position of a molecule and its imaged widths along two perpendicular axes is given by

$$\begin{aligned}
\sigma_{\mathrm{x}}(z) &= \tfrac{w_{0x}}{2}\sqrt{1+\left(\tfrac{z-c_x}{d_x}\right)+a_x\left(\tfrac{z-c_x}{d_x}\right)^2+b_x\left(\tfrac{z-c_x}{d_x}\right)^4}\,, \\
\sigma_{\mathrm{y}}(z) &= \tfrac{w_{0y}}{2}\sqrt{1+\left(\tfrac{z-c_y}{d_y}\right)+a_y\left(\tfrac{z-c_y}{d_y}\right)^2+b_y\left(\tfrac{z-c_y}{d_y}\right)^4}\,.
\end{aligned} \tag{3.16}$$

Here $w_{0x}, a_x, b_x, c_x, d_x$ and $w_{0y}, a_y, b_y, c_y, d_y$ are unknown parameters of the model which are determined by the calibration process prior to the analysis.

Calibration of the imaging system

Calibration is a procedure which determines the orientation angle ϕ of the imaged ellipsoids, and the relationship between the axial position z of the molecules and their imaged widths $\sigma_{\mathrm{x}}(z), \sigma_{\mathrm{y}}(z)$. The calibration is typically performed using a z-stack of images of sub-diffraction fluorescent beads. We use a sparse sample with about 10 to 50 beads in the image and a z-stack image sequence with an axial range of about 2 μm and a step size of 10 nm.

Determining the orientation angle

1. A sequence of images from a z-stack is processed slice-by-slice and the imaged beads are fit independently using the elliptical Gaussian $\mathrm{h}_{\mathrm{EG}}(x, y \mid \theta, \phi)$ with rotation angle ϕ as a free parameter.

2. Results close to circular are discarded as the angle ϕ cannot be determined.

3. The final orientation angle is calculated as the circular mean of all remaining measurements

$$\phi = \frac{1}{4}\operatorname{atan2}\left(\frac{1}{n}\sum_{i=1}^{n}\sin\varphi_i, \frac{1}{n}\sum_{i=1}^{n}\cos\varphi_i\right), \tag{3.17}$$

where $\varphi_i = 4\left(\phi_i \bmod \frac{\pi}{2}\right)$ adjusts the fitted angles ϕ_i, and n is the number of measured beads.

Ellipticity as a function of an axial position

1. Using the approximate positions of the beads in multiple z-planes and the orientation angle ϕ, both determined in the previous step, the images of the beads are fit again using the elliptical Gaussian PSF $\mathrm{h}_{\mathrm{EG}}(x, y \mid \theta, \phi)$, but now with a fixed angle ϕ determined in the previous step.

2. To estimate the coefficients for the defocusing model given by Equation (3.16), we first fit the pair of defocusing curves for each bead separately using an iteratively reweighed least-squares algorithm which automatically discards outliers.

3. From the fitted models, we determine a common focal plane of the beads as $\frac{c_x + c_y}{2}$ and shift the data along the z-axis such that all beads are positioned at the same focal plane.

4. The final coefficients are obtained by fitting the pair of defocusing curves to all shifted data points. The "zero" axial position is given by the intersection of the two polynomials.

3D Localization uncertainty The lateral uncertainty is calculated in the same way as in Equation (3.14), but τ differs because of the axial defocus (PSF spreads and is never focused in both planes simultaneously, thus the overall uncertainty is worse). This has been derived in (Rieger and Stallinga, 2014) as

$$\tau = \frac{2\pi(\hat{b}^2 + r)(\hat{\theta}_{\sigma_x}\hat{\theta}_{\sigma_y}(1 + l^2/d^2) + a^2/12)}{a^2 \hat{\theta}_N}. \tag{3.18}$$

Since the axial position is estimated from $\hat{\theta}_{\sigma_x}$ and $\hat{\theta}_{\sigma_y}$, the axial uncertainty is calculated from the uncertainty of these parameters

$$\begin{aligned} (\Delta\hat{\theta}_{\sigma_j})^2\big|_{\mathrm{LSQ}} &= \frac{g\hat{\theta}_{\sigma_j^2} + a^2/12}{\hat{\theta}_N}(1 + 8\tau), \\ (\Delta\hat{\theta}_{\sigma_j})^2\big|_{\mathrm{MLE}} &= \frac{g\hat{\theta}_{\sigma_j^2} + a^2/12}{\hat{\theta}_N}\left(1 + 8\tau + \sqrt{\tfrac{9\tau}{1+4\tau}}\right), \end{aligned} \tag{3.19}$$

where j can be substituted for x and y to calculate uncertainty of $\hat{\theta}_{\sigma_x}$ and $\hat{\theta}_{\sigma_y}$ respectively. Then from error propagation it follows

$$F^2 = \frac{4l^2\hat{\theta}_z^2}{(l^2+d^2+\hat{\theta}_z^2)^2}, \tag{3.20}$$

$$(\Delta F)^2 = (1-F^2)\left[\left(\frac{\Delta\hat{\theta}_{\sigma_x}}{\hat{\theta}_{\sigma_x}}\right)^2 + \left(\frac{\Delta\hat{\theta}_{\sigma_y}}{\hat{\theta}_{\sigma_y}}\right)^2\right], \tag{3.21}$$

$$(\Delta\hat{\theta}_z)^2 = (\Delta F)^2\frac{(l^2+d^2+\hat{\theta}_z^2)^4}{4l^2(l^2+d^2-\hat{\theta}_z^2)^2}, \tag{3.22}$$

where $2l$ is the distance between focal planes given by the astigmatic lens and the geometry of the setup and d is a measure of focal depth, which can be generally calculated as half the axial Rayleigh unit, thus $d = \lambda\eta/(\mathrm{NA})^2$, where λ is the emission wavelength and η is the refractive index of the mounting/immersion media. Nonetheless, these quantities can be estimated - in fact they are already known during the 3D fitting process, because l^2 corresponds to c_xc_y and d^2 corresponds to d_xd_y, which are parameters of the defocus curves defined in Equation (3.16).

3.5 Special case: the *crowded field* problem

To solve this problem, ThunderSTORM uses a multiple-emitter fitting analysis (MFA) approach similar to the algorithm described in (Huang et al., 2011).

The multiple-emitter fitting analysis approach uses a PSF model defined as

$$\mathrm{h}_N(x,y \mid \Theta) = \sum_{i=1}^{N}\mathrm{h}(x,y \mid \theta_i), \tag{3.23}$$

where N is a number of molecules allowed in the fitting region, and $\Theta = [\theta_1,\ldots,\theta_N]$ are parameters describing position and shape of the imaged molecules modeled by the PSF.

The fitting of multiple-emitter models to the raw data proceeds according to the following algorithm. First, the algorithm fits $\mathrm{h}_1(x,y \mid \theta_1)$ (a single molecule model). The fitted PSF is subtracted from the raw data and the position of the maximum intensity value in the residual image is taken as an approximate position of a second molecule. The fitting is now repeated on the raw data with $\mathrm{h}_2(x,y \mid \theta_1,\theta_2)$ (a model containing two molecules) and with the initial positions estimated in the previous steps. The result of the fit is subtracted from the raw data to find an approximate position of a third molecule in the residual image. This routine is repeated until the maximum number of molecules allowed in the fitting region is reached. Note that initial positions of the molecules are further adjusted, during the multiple-emitter fitting analysis, by a "Push&Pull" process, see (Huang et al., 2011). To find the optimal number of molecules, statistical tests are required.

Users can specify the size of the fitting region, the maximum number of molecules allowed in one fitting region, the type of PSF, and a fitting method. Optionally, users can constrain the multiple-emitter fitting algorithm such that all fitted molecules have the same intensity or an intensity in a given range. The background offset is constrained to the same intensity for all fitted molecules.

Model selection

Because a model with more parameters will always be able to fit the data at least as well as a model with fewer parameters, statistical tests are required to determine whether the more complex model provides a significantly better fit of the underlying data. Statistical tests are usually based on pair-wise model comparison. Here a fit by h_1 is compared with a fit by h_2, the better of the two is compared with a fit by h_3, etc. Pair-wise comparisons are based on an F-test if least squares fitting is used, otherwise a log-likelihood ratio test is used. Note that the model selection based on a fitting method, and the application of the F-test in particular, is a unique feature in ThunderSTORM.

F-test An F-test (Bevington and Robinson, 2003) arises in the case of fitting by least squares methods, when we need to compare significance of the fit between two models, where one model (the null model) is a special case of the other (the alternative model) for some choice of parameters. The F-test statistic computed from the data is given by the formula

$$F_{\chi^2}(\mathscr{D}) = \frac{\left(\chi^2(\Theta_0 \mid \mathscr{D}) - \chi^2(\Theta_1 \mid \mathscr{D})\right) / (v_1 - v_0)}{\chi^2(\Theta_1 \mid \mathscr{D}) / (n - v_1)}, \tag{3.24}$$

where the sum of squared residuals $\chi^2(\Theta \mid \mathscr{D})$ computed for a model with parameters Θ is defined by Equation (3.9), vectors Θ_0 and Θ_1 are parameters of the null and alternative model, respectively, v_0 and v_1 (where $v_0 < v_1$) represent the number of free parameters of the null and alternative model, respectively, and $n = l^2$ is the number of data points within the fitting region $\mathscr{D}$.

Assuming the null hypothesis that the alternative model does not provide a significantly better fit than the null model, the F-test statistics computed in Equation (3.24) has an F-distribution with $(v_1 - v_0, n - v_1)$ degrees of freedom. The null hypothesis is rejected if $F_{\chi^2}(\mathscr{D})$ computed from the data is greater than the critical value of the $F_{v_1 - v_0, n - v_1}$ distribution for a user-specified p-value.

Log-likelihood ratio test

To compare between the fits of two models, in the case of fitting by a maximum likelihood method, we use a model selection criteria based on a log-likelihood ratio test (Huang et al., 2011). Assuming that one model (the null model) is a special case of the other (the alternative model) for some choice of parameters, the log-likelihood ratio is given by the formula

$$\Lambda(\mathscr{D}) = -2 \ln \left[\frac{\mathcal{L}(\Theta_0 \mid \mathscr{D})}{\mathcal{L}(\Theta_1 \mid \mathscr{D})}\right], \tag{3.25}$$

where the likelihood $\mathcal{L}(\Theta \mid \mathscr{D})$ of parameters Θ is defined by Equation (3.13), Θ_0 and Θ_1 are the parameters of the null and alternative model, respectively, and $\mathscr{D}$ is a fitting region.

The probability distribution of the log-likelihood ratio computed in Equation (3.25), assuming the null hypothesis that the alternative model does not provide a significantly better fit than the null model, can be approximated by the χ^2 distribution with $v_1 - v_0$ degrees of freedom. This approximation is usually valid even for small sample sizes (Kendall and Stuart, 1979). Here v_0 and v_1 (where $v_0 < v_1$) represent the number of free parameters of the null and alternative models, respectively. The null hypothesis is rejected if the log-likelihood ratio

$\Lambda(\mathscr{D})$ computed from the data is greater than the critical value of the $\chi^2_{\nu_1-\nu_0}$ distribution for some p-value specified by the user.

3.6 Post-processing

In addition to the methods for image analysis, ThunderSTORM also provides a variety of post-processing tools which can be applied to the results obtained from previously analyzed SMLM images. The software includes methods for correcting the data by removing molecules with, e.g., poor localization accuracy or small local density, for merging molecules present in subsequent images, and for position correction of molecules caused by lateral drift of the sample and/or by axial stage scanning.

Input: A list of coordinates with sub-pixel positions of the molecules.

Output: A corrected list of coordinates with sub-pixel positions of the molecules.

3.6.1 Removing molecules with poor localization

ThunderSTORM can remove unwanted molecules according to user-defined criteria, or display molecules in a user-specified region. The filtering criteria is formulated as an expression combining mathematical and logical functions and operators with parameters from the table of results obtained from previous data analysis. All molecules with parameters not accepted by the criteria are removed. Note that users can also display histograms of particular measured parameters and select thresholds to define the filtering criteria.

3.6.2 Local density filtering

Local density filtering effectively removes noise created by, e.g., isolated localizations. The method works by calculating the number of neighbors at a given radius (in a circle or a sphere) for every localization event. A localization event is discarded if the number of neighbors is below a user-specified threshold.

3.6.3 Merging of reappearing molecules

In some SMLM experiments, a single photoactivated molecule may appear in several sequential images, then disappear for a while, appear again, and finally bleach completely. If this is the case, ThunderSTORM identifies such sequences of molecular locations and combines them into one single molecule. This feature is especially important in PALM or STORM experiments where we want to count the number of molecules in a sample. The new position, imaged size, and the background offset of the resulting signal is calculated as the mean value of the original data, while the intensity and the background signal level is calculated as the sum. The localization uncertainty of the merged molecule is calculated from the new values. The distance within which molecules are merged together in the subsequent frames, as well as the allowed number of frames in which the molecule can disappear, are user-specified values. Users can also specify a maximum number of consecutive frames such that a repeating event is still considered a single molecule, see the timing diagram in Figure 3.2. The merging algorithm is based on finding nearest-neighbors between active molecules from the previous frame and the current frame.

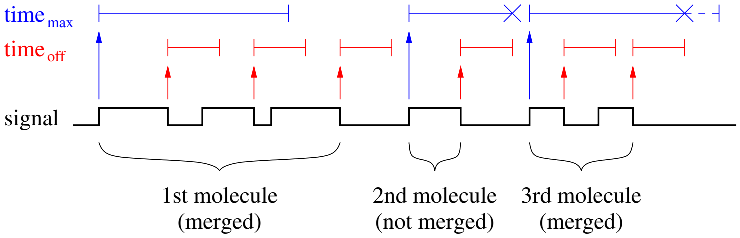

Fig. 3.2 Timing diagram of the merging algorithm.

3.6.4 Removing duplicates

Repeated localizations of single molecules in one frame may occur due to overlapping fitting sub-regions when using the multiple-emitter analysis approach. To deal with this problem, ThunderSTORM uses a post-processing method suggested by (Huang et al., 2011). Here molecules with a mutual distance smaller than their localization uncertainty are grouped together, and in each group, only the molecule with the smallest localization uncertainty is kept. The other molecules are rejected. ThunderSTORM generalizes this algorithm by allowing users to specify the distance threshold for grouping the molecules as a mathematical expression. A different distance threshold can be applied to individual molecules.

3.6.5 Lateral drift correction

Long time-series data acquisitions usually suffer from sample drift. Correcting for this negative effect can significantly improve resolution of reconstructed images as displayed in Figure 3.3. ThunderSTORM supports two methods for lateral drift correction. The first is based on tracking fiducial markers inserted into the sample, and the second on cross-correlation of similar structures in reconstructed super-resolution images. The trajectory of the relative sample drift can be saved to a file and applied later, possibly to a different dataset. For example, drift estimated from a sub-region of the data can be applied to the whole dataset, or drift estimated from one channel can be applied to correct drift in another channel.

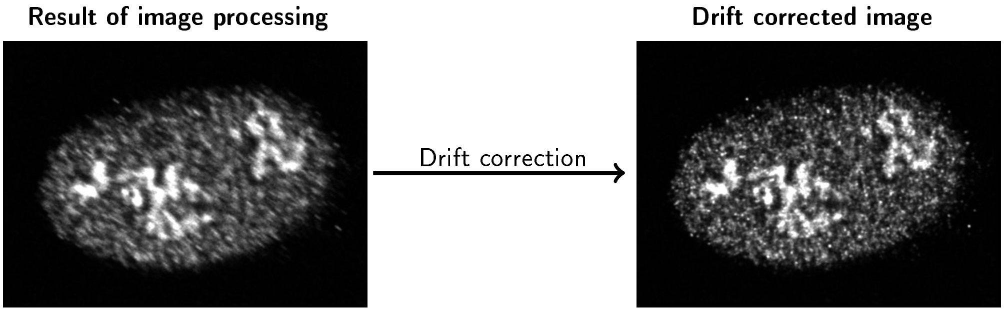

Fig. 3.3 Example of drift correction.

Fiducial markers

A common approach for correcting drift is performed by tracking fiducial markers present in the sample and then subtracting their relative motion from the molecular localizations. ThunderSTORM can identify fiducial markers automatically from the localization results as molecules that stay in the “on” state at one position for a substantial amount of time. Therefore, all localizations that arise from more than a user-specified number of frames are considered as fiducial markers and are used for the drift correction. Assigning molecular localizations in subsequent frames to a single fiducial marker is performed by the merging algorithm described above, in Section 3.6.3.

The sample drift is obtained by averaging the relative trajectories of all identified fiducial markers into a single trajectory. The sample drift at each frame $t = 1, \ldots, T$, is computed (for x and y) according to the formula

$$\bar{x}_t = \frac{1}{M} \sum_{i=1}^{M} (x_{i,t} - \theta_i) \ . \tag{3.26}$$

Here M is the number of fiducial markers, $x_{i,t}$ is the absolute position of the i-th marker at frame t, $i = 1, \ldots, M$, and θ_i is an unknown offset which has to be subtracted from the absolute marker position to obtain the relative position.

The offset θ_i is estimated by least squares minimization of the sum of squared differences between the relative marker positions and the relative sample drift, summed over all markers and frames. The optimization is defined by the formula

$$\hat{\theta} = \underset{\theta = \{\theta_1, \ldots, \theta_M\}}{\arg\min} \sum_{t=1}^{T} \sum_{i=1}^{M} \left((x_{i,t} - \theta_i) - \bar{x}_t \right)^2 , \tag{3.27}$$

where $\hat{\theta} = \left\{ \hat{\theta}_1, \ldots, \hat{\theta}_M \right\}$ are the values of the estimated offset for each of the markers.

In reality, some of the points $x_{i,t}$ may be missing because the markers might not be localized in some frames. If this is the case, the relative sample drift in Equation (3.26) is computed only from the corresponding number of fiducial markers. For the missing markers, the corresponding sum of squared differences in Equation (3.27) is set to zero.

The final drift trajectory is smoothed by robust locally weighted regression (Cleveland, 1979). Users can specify the maximum merging distance and the minimum number of frames in which a molecule must appear to be considered as a fiducial marker, and the trajectory smoothing factor.

Note that analyzing samples with fiducial markers yields localizations of both the blinking fluorophores and the fiducial markers. This may slow down the merging algorithm used for automatic identification of the markers. For faster marker identification, the merging process can be limited to regions containing only the fiducial markers. The drift trajectory can then be saved to a file and applied later to the whole dataset.

Cross-correlation

ThunderSTORM also supports lateral drift correction using the method of (Mlodzianoski et al., 2011). Here, the list of localized molecules is split into $n+1$ batches based on the frame in which they appeared. Each batch is used to create one super-resolution image. The presumption of this method is that similar structures will appear in all reconstructed images. Cross-correlation methods are used to determine the shift between the first image and each of the subsequent images. This leads to n cross-correlation images, where the shift in the position caused by the drift corresponds to the relative position between the global intensity maximum peaks. The localized peaks are assigned to the central frame of each batch sequence and the drift for intermediate frames is determined by local regression using third degree polynomials. The original molecular coordinates are corrected for drift using the estimated values.

In our implementation, super-resolution images are created by the average shifted histograms method described in Section 3.8.1, cross-correlation images are computed using the Fast Fourier Transform, and the location of global intensity maximum peaks is determined with sub-pixel precision using the radial symmetry method (Parthasarathy, 2012). The number of batches n and the magnification of super-resolution images is defined by the user. For better stability of the solution, intensity maximum peaks are first localized in cross-correlation images computed from reconstructed images with a magnification of one. The peak position is refined afterwards using cross-correlation images computed from super-resolution images with a user specified magnification. The final position of the peak is obtained as a local intensity maximum in close proximity to the peak obtained at lower magnification.

3.6.6 Z-stage scanning

To extend the axial field of view in 3D SMLM experiments, data can be acquired in multiple z-stage positions (Huang et al., 2008a). However, the astigmatism method described in Section 2.2 can estimate only the relative axial positions of molecules with respect to the focal plane. To find the absolute z coordinates, the correct offset must be added to the axial positions of each molecule. The new z coordinate can be determined as

$$z_{\text{abs}} = z_0 + z_{\text{rel}} + z_{\text{step}} \left(\left\lfloor \frac{f-1}{n_{\text{im}}} \right\rfloor \bmod n_{\text{pos}} \right) , \tag{3.28}$$

where z_0 is the initial z-stage offset, z_{rel} is the estimated molecular position relative to the focal plane ($z_{\text{rel}} = 0$ for 2D data), z_{step} is the step between two positions of the z-stage, f is the image frame in which a given molecule appeared, n_{im} is the number of images taken in each z-stage position, and n_{pos} is the number of z-stage positions. All z variables are in nm.

An example of z-stage scanning on real data processed by ThunderSTORM is shown in Figure 3.4.

3.7 Experimental evaluation of SMLM algorithms

An integral part of developing a process for SMLM image analysis is a testing in a controlled environment and quantitative evaluation of performance of individual SMLM algorithms. Monte Carlo simulations can be used for this purpose (Křížek et al., 2011).

Our simulation engine implemented in ThunderSTORM is capable of generating realistic sequences of SMLM-like images in which the ground-truth positions of the molecules are known. A grayscale mask can be used to vary the spatial density of molecules. When the localization data and the ground-truth positions of molecules are available, ThunderSTORM can quantitatively evaluate the performance of localization algorithms by calculating, e.g., the Jaccard index or F1 score as described below in Section 3.7.4. In addition to the image size and sequence length, users can specify the intensity, imaged size, and spatial density of

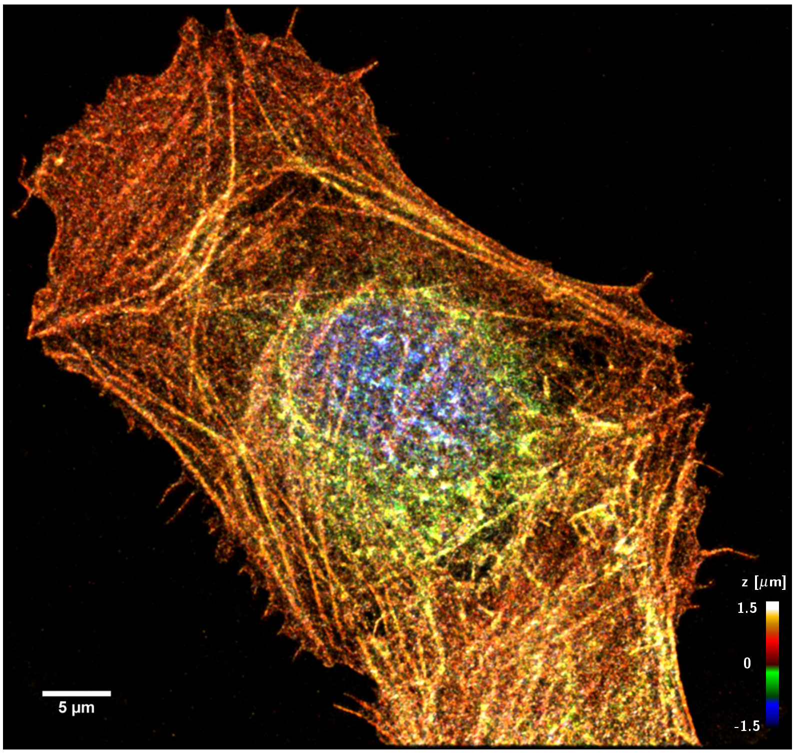

Fig. 3.4 Imaging Atto565-phalloidin labeled actin in U2-OS cells using z-stage scanning (9 planes, 9000 frames in total). This way, we were able to image deeper into the cell than with just astigmatism. We can see several "layers" in the image, especially in the area of the cell nucleus where the cell is the thickest.

the generated molecules. The resulting images can be subjected to sample drift. Noise in the generated images simulates the behavior of CCD or EMCCD cameras.

3.7.1 Image formation model

For each frame, we first create an ideal, noise free, SMLM-like image to simulate the expected number of photons detected in each camera pixel. Image formation starts by creating a list of molecules with intensity chosen randomly in user-specified range, and with random positions of molecules given by a user-specified spatial density, see Section 3.7.2. Users can also specify any of the implemented PSF models, including 3D models described in Section 2.2, to create the simulated images of molecules. The generated molecules are added sequentially to the final image. A user-specified offset is added to the generated image sequence to simulate a background. Alternatively, a gray-scale image, in which each pixel value is normalized to the unit interval, can be used as a weighting factor of the offset level in different parts of the generated images to simulate an irregular background as might be encountered in real samples.

In order to simulate the photon counting process in the generated images, each pixel value expressed in photons is modified by a Poisson-distributed random number. The data generator can optionally simulate EM gain of EMCCD cameras. In this case we use a stochastic model described in (Hirsch et al., 2013), where the electron multiplication is modeled by the Gamma distribution $\Gamma(k,g)$. The shape k is given by the number of photons detected in the simulated CCD register and the scale g is given by the user-specified value of gain.

Finally, the signal in the camera register is digitized by converting the photons to digital counts. The CCD sensitivity (in photons per A/D count), and the camera digitizer offset (in A/D counts) are user-specified in the camera setup, as well as the camera pixel size (in nanometers) as projected to the sample plane.

3.7.2 Fixed or spatially varying density of molecules

Users can specify a fixed or spatially varying density of simulated molecules in the generated images. The variability is achieved by a user-supplied gray-scale mask M, in which each pixel value is normalized to the unit interval and used to represent the weighting factor, see Figure 3.5. The average number of molecules at a given integer pixel position (x,y) is then computed as

$$\overline{d}\left(x,y\right) = a^2 M\left(x,y\right) d_{\mathrm{max}}\,, \tag{3.29}$$

where a is the camera pixel size as projected to the sample plane, and d_{max} is the maximum spatial density of molecules per unit area as specified by users.

The procedure for generating molecular positions follows the spatial Poisson point process (Kendall and Stuart, 1979). Thus for each value $\overline{d}\left(x,y\right)$, a random number of events (molecules) is created in the pixel (x,y) using a Poisson random number generator. Molecular centers are placed uniformly and randomly within that pixel.

Note that the mask M should be at least the same size as the desired super-resolution image in order to preserve high resolution in the final reconstruction. The coordinates of the molecular centers are down-scaled appropriately.

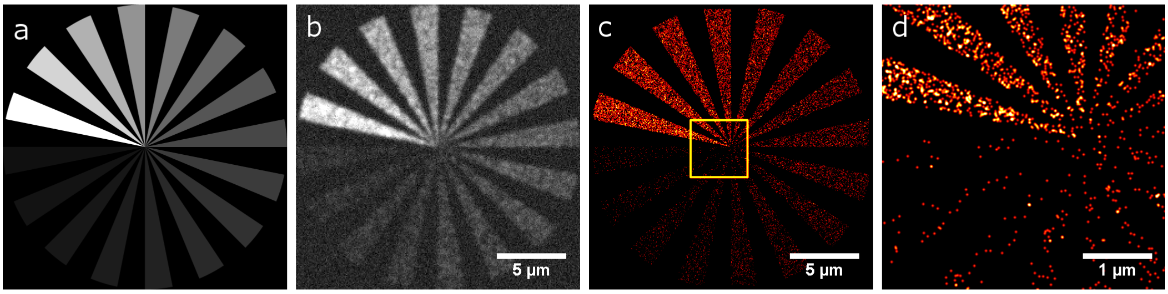

Fig. 3.5 SMLM data generated with variable spatial density of molecules. (a) gray-scale mask, (b) average intensity time projection of raw data, (c) SMLM data reconstruction, (d) zoomed region indicated in (c).

3.7.3 Additional sample drift

The generated molecular positions in the image sequence can be subjected to a lateral sample drift. Users need to specify the speed and direction of the drift, which is constant throughout the image sequence.

3.7.4 Performance evaluation

The process of performance evaluation starts by pairing the localized molecules with the closest molecule in the ground-truth data, see Figure 3.6. The numbers of correctly and incorrectly identified molecules are counted as follows: if the distance between the paired molecules is smaller than a user-specified radius, then the localization is counted as a true positive (TP) detection and the localized molecule is associated with the ground-truth position. If the distance is greater than or equal to that radius, then the localization is counted as a false positive (FP) detection. Ground-truth molecules which were not associated with the localized molecules are counted as false negatives (FN). With a growing density of molecules it becomes more important how the algorithm performs the matching. To solve the problem of finding the correct matching between localized molecules and the ground-truth data, the

Gale-Shapley algorithm (Gale and Shapley, 1962) is applied. Moreover, KD-trees (Knuth, 1997) are employed for an effective implementation.

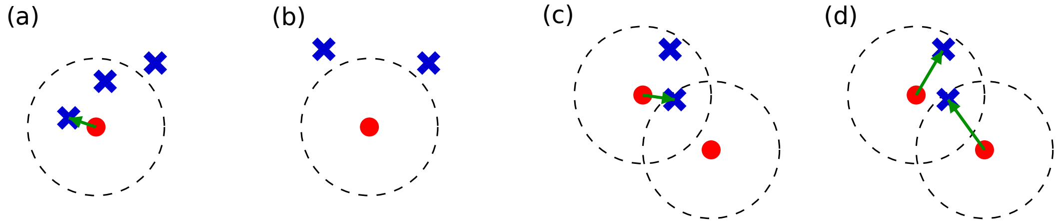

Fig. 3.6 Counting localized and missed molecules. Red dot - ground-truth position of a molecule, blue cross - localized molecule, green arrow - association of a localized molecule with ground-truth position, dashed circle - detection tolerance radius. (a) 1 TP + 2 FP, (b) 1 FN + 2 FP, (c)-(d) example of a situation, where (c) greedy approach fails by finding 1 TP + 1 FP + 1 FN, and where (d) Gale-Shapley algorithm finds a correct solution with 2 TP.

Precision and recall

Statistical measures related to the number of correctly or incorrectly detected molecules, or missed molecules, are the recall r (also called sensitivity) and the precision p (also called positive predictive value) (Tan et al., 2005). Their definitions are given by

$$\begin{aligned} r &= \frac{\mathrm{TP}}{\mathrm{TP}+\mathrm{FN}}, \\ p &= \frac{\mathrm{TP}}{\mathrm{TP}+\mathrm{FP}}. \end{aligned} \tag{3.30}$$

Recall measures the fraction of correctly identified molecules, and precision measures the portion of correctly identified molecules in the set of all localizations. The theoretical optimum is achieved for values of recall and precision both equal to 1.0.

F1 score

For purposes of comparison between multiple algorithms, it is convenient to combine precision and recall into a single measure of performance with some trade-off between both values. A traditional method for this applies the F_1 score (Tan et al., 2005) defined by

$$F_1 = \frac{2pr}{p+r}. \tag{3.31}$$

Values of the F_1 score close to zero indicate both bad recall and precision while values approaching 1 signify a good ratio between recall and precision.

RMS distance

For all molecules identified as true positives, we also calculate the root-mean square distance between the ground-truth positions of the molecules and their localizations.

3.8 SMLM data analysis

Once the initial analysis is complete and we have coordinates of molecules, SMLM experiments can be further analyzed either by visual examination of a rendered super-resolution image, or by some quantitative methods, such as evaluating co-localization or clustering of molecules. Here we discuss some of the methods implemented in ThunderSTORM.

3.8.1 Visualization methods

Visualization (rendering) of SMLM data involves creation of a new super-resolution image based on the coordinates of the localized molecules. ThunderSTORM offers several methods, all of which support both two-dimensional visualization and slice-by-slice three-dimensional visualization. In the three-dimensional case, each image slice contains a visualization of molecules with axial positions in the user-specified range. The desired magnification ratio of the new super-resolution image to the original image is user-specified. Note that some software such as PALMsiever or ViSP (El Beheiry and Dahan, 2013) are also able to render the “clouds” of 3D points as an iso-surface, however, although it’s a nice feature, such images are rarely useful in SMLM analysis due to significant loss of information.

Input: A list of coordinates with sub-pixel positions of the molecules.

Output: A super-resolution image with user-specified size and magnification.

Scatter plot

Scatter plot visualization (Baddeley et al., 2010) is the simplest method, and does not usually provide high quality results. A simple binary image is created with pixel intensity values set to one at locations corresponding to molecular positions. All other pixel intensity values are set to zero. This method is fast but does not reflect the density of molecules.

Histogram

Histograms are used to estimate the density of data by counting the number of observations that fall into each of the bins. In our case, a two-dimensional histogram of molecular positions is created with the bin size corresponding to the pixel size of the final super-resolution image (Baddeley et al., 2010). Thus, for every localized molecule, the bin value (i.e., the image brightness) at the corresponding molecular positions is incremented by one.

The histogram visualization optionally supports “jittering” (Křížek et al., 2011). When enabled, a random number drawn from the normal distribution, with a standard deviation equal to the computed (or user-specified) localization uncertainty, is added to the coordinates of every molecular position before creating the histogram. This step is applied multiple times and all generated histograms are averaged together. As the number of jitters increases, the final image approaches the result of the Gaussian rendering described in Section 3.8.1. For a small number of jitters, the histogram visualization is much faster than the Gaussian rendering but the resulting images may appear noisy.

Gaussian rendering

This method draws a normalized symmetric 2D or 3D Gaussian function integrated over the voxel volume for every localized molecule, with a standard deviation equal to the computed, or user-specified localization uncertainty. The visualized molecules are added sequentially to the final super-resolution images. The contribution of one molecule to the voxel intensity at the integer position (x,y,z) is computed as

$$v\left(x,y,z \mid \theta_x, \theta_y, \theta_z, \sigma_{xy}, \sigma_z\right) = \mathrm{E}(x \mid \theta_x, \sigma_{xy})\mathrm{E}(y \mid \theta_y, \sigma_{xy})\mathrm{E}(z \mid \theta_z, \sigma_z)\,, \tag{3.32}$$

where $(\theta_x, \theta_y, \theta_z)$ is position of a molecule, σ_{xy} is the corresponding lateral localization uncertainty, and σ_z is the axial localization uncertainty,

$$\begin{aligned}
\mathrm{E}(x \mid \theta_x, \sigma_{xy}) &= \tfrac{1}{2}\operatorname{erf}\left(\frac{x-\theta_x+\frac{1}{2}}{\sqrt{2}\sigma_{xy}}\right) - \tfrac{1}{2}\operatorname{erf}\left(\frac{x-\theta_x-\frac{1}{2}}{\sqrt{2}\sigma_{xy}}\right), \\
\mathrm{E}(y \mid \theta_y, \sigma_{xy}) &= \tfrac{1}{2}\operatorname{erf}\left(\frac{y-\theta_y+\frac{1}{2}}{\sqrt{2}\sigma_{xy}}\right) - \tfrac{1}{2}\operatorname{erf}\left(\frac{y-\theta_y-\frac{1}{2}}{\sqrt{2}\sigma_{xy}}\right), \\
\mathrm{E}(z \mid \theta_z, \sigma_z) &= \tfrac{1}{2}\operatorname{erf}\left(\frac{z-\theta_z+\frac{\Delta_z}{2}}{\sqrt{2}\sigma_z}\right) - \tfrac{1}{2}\operatorname{erf}\left(\frac{z-\theta_z-\frac{\Delta_z}{2}}{\sqrt{2}\sigma_z}\right),
\end{aligned} \tag{3.33}$$

and $\triangle_z$ is the size of a voxel in the axial direction. Contributions from one molecule are limited to an interval given by a circle with radius of $3\sigma_{xy}$ around the position of the molecule in the lateral dimension and by $3\sigma_z$ in the axial direction. For data visualization in the 2D case, $z = 0$ and $\mathrm{E}(z \mid \theta_z, \sigma_z) = 1$.

Averaged shifted histograms

This visualization algorithm uses a density estimation approach based on averaged shifted histograms (Scott, 1985). In the one-dimensional case, this method works by averaging n histograms with the same bin width w, but with the origin of each histogram shifted by $\frac{w}{n}$ from the previous histogram. In the multidimensional case, there are n^d multidimensional histograms averaged in total, i.e., for n shifts in each of the d dimensions. In our implementation, the width of the histogram bin is determined as $w = na$, where a is the pixel size of the super-resolution image. The number of shifts n in the lateral and axial directions can be specified independently. This rendering method has been first published in (Ovesný et al., 2014a) and its advantages are that it is very fast and gives very nice results. That is why it is the default rendering method used in ThunderSTORM.

Comparison of visualization methods

All visualization methods described above, except for the scatter plot, result in molecular density maps. The time complexity of rendering is $\mathcal{O}(N)$, where N is the number of molecules to visualize. However, the real speed of visualization depends on the number of histograms to average in the case of histogram based methods, or on the volume to render in the case of Gaussian rendering. The Gaussian rendering approach is slow but it can show the calculated localization accuracy for each molecule. The method based on averaging histograms with jittered molecular positions approximates the Gaussian rendering approach for a large number of jitters. This method is fast for small number of jitters but the resulting images appear very noisy. The proposed method based on the average shifted histogram approach provides similar results as Gaussian rendering with a constant standard deviation, therefore the result does not show the localization uncertainty for each molecule. However, the average shifted histogram approach is orders of magnitude faster than Gaussian rendering. For more information about other visualization methods see (Baddeley et al., 2010).

Figures 3.7 and 3.8 show a comparative overview of the rendering algorithms available in ThunderSTORM. We tested the methods both on simulated and real data.

Simulated data were created using the module "Generator of simulated data" within ThunderSTORM. The raw image sequence consists of 1000 images of size 256×256 pixels with a pixel size of $80\ \mathrm{nm}/\mathrm{pixel}$. The spatial density was set to $0.5\ \mathrm{molecules}/\mu\mathrm{m}^2$ and was modulated by a Siemens-star pattern. The Siemens star pattern is commonly used to test the resolution of optical instruments. Other camera and data generator settings were kept at default values. About eighty thousand molecules were generated and localized. The results of different visualization methods with different parameter settings are shown in Figure 3.7.

For real data, we used the image sequence "Tubulin AF647"[1]. The raw image sequence consists of 9990 frames of size 128×128 pixels with a pixel size of $100\ \mathrm{nm}/\mathrm{pixel}$. Data were processed by ThunderSTORM with the default settings. About sixty thousand molecules were localized and drift correction was applied. Super-resolution images visualized by different methods are shown in Figure 3.8.

3.8.2 Co-localization

Co-localization analysis is a commonly used approach to the measure spatial overlap between two (or more) different fluorescent labels, each having a different emission wavelength. Traditional co-localization analysis of laser scanning confocal microscopy images has several

---

[1] A dataset from *SMLM Challenge 2013* available at http://bigwww.epfl.ch/smlm/challenge2013/

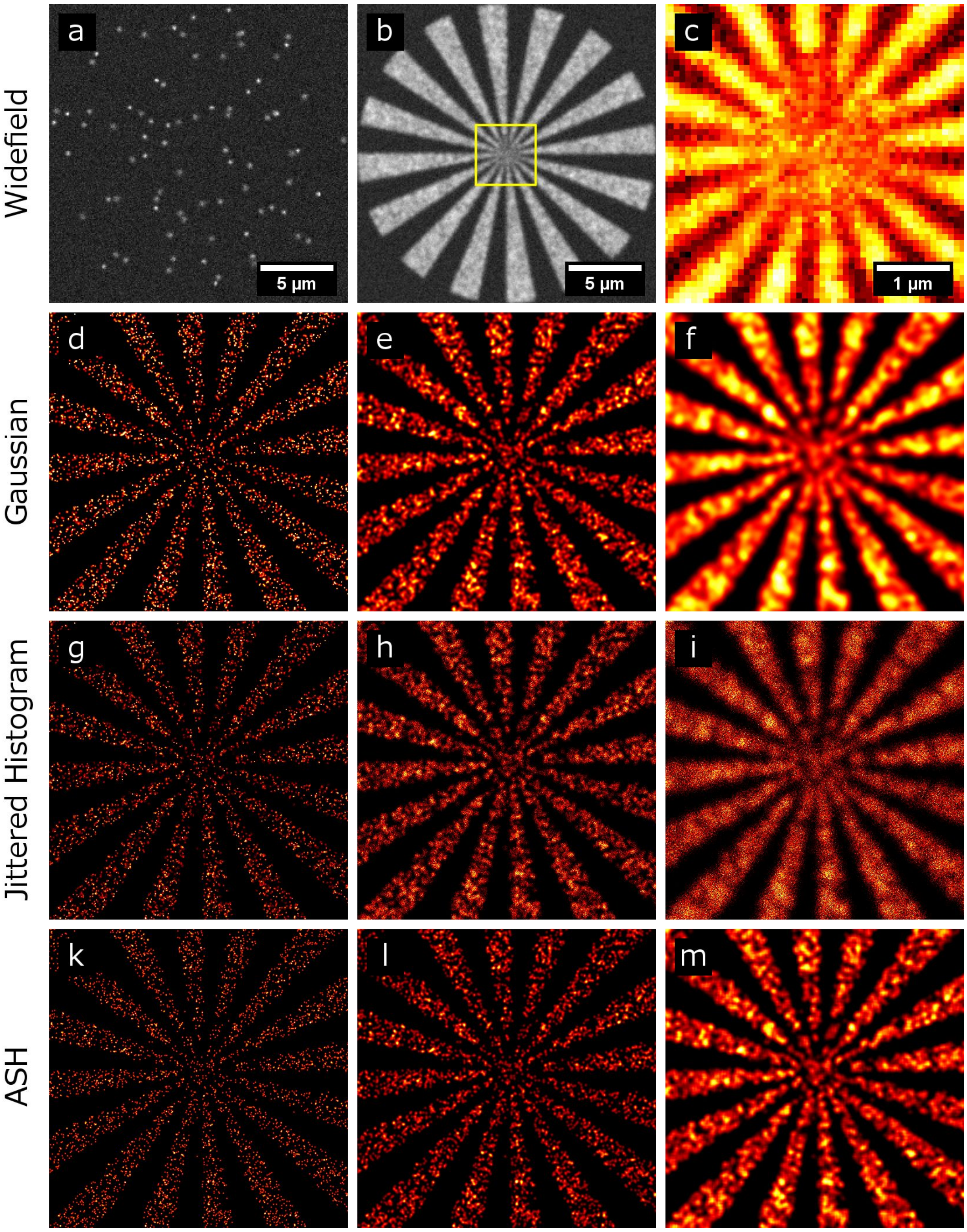

Fig. 3.7 Comparison of visualization methods on simulated data. Widefield images: (a) a single frame of raw data, (b) average intensity time projection, (c) zoomed region indicated in (b). (d)-(m) Super-resolution SMLM images of the region indicated in (b) magnified 10×. Gaussian rendering with lateral uncertainty set to: (d) computed localization uncertainty, (e) 20 nm, (f) 50 nm. Jittered Histogram with number of averages set to 100 and with lateral uncertainty set to: (g) computed localization uncertainty, (h) 20 nm, (i) 50 nm. Average Shifted Histogram with the number of lateral shifts set to: (k) 2, (l) 4, (m) 8.

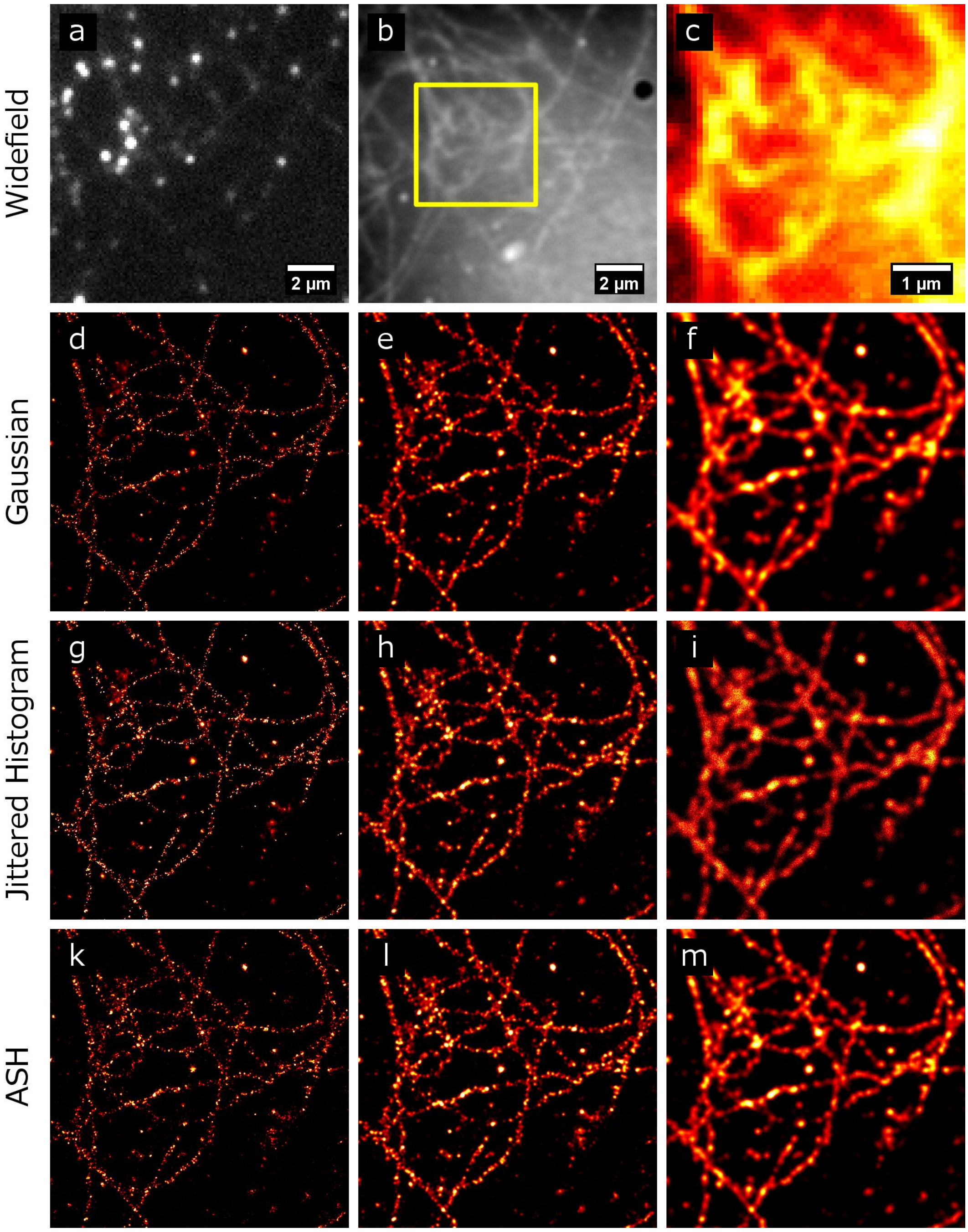

Fig. 3.8 Comparison of visualization methods on Tubulin AF647. Widefield images: (a) a single frame of raw data, (b) average intensity time projection, (c) zoomed region indicated in (b). (d)-(m) Super-resolution SMLM images of the region indicated in (b) magnified 10×. Gaussian rendering with lateral uncertainty set to: (d) computed localization uncertainty, (e) 20 nm, (f) 50 nm. Jittered Histogram with number of averages set to 100 and with lateral uncertainty set to: (g) computed localization uncertainty, (h) 20 nm, (i) 50 nm. Average Shifted Histogram with the number of lateral shifts set to: (k) 2, (l) 4, (m) 8.

limitations (Ronneberger et al., 2008), see Figure 3.9. However SMLM methods offer a new paradigm for co-localization studies due to the coordinate-based nature of the data (Gunkel et al., 2009; Malkusch et al., 2012; Smirnov et al., 2014).

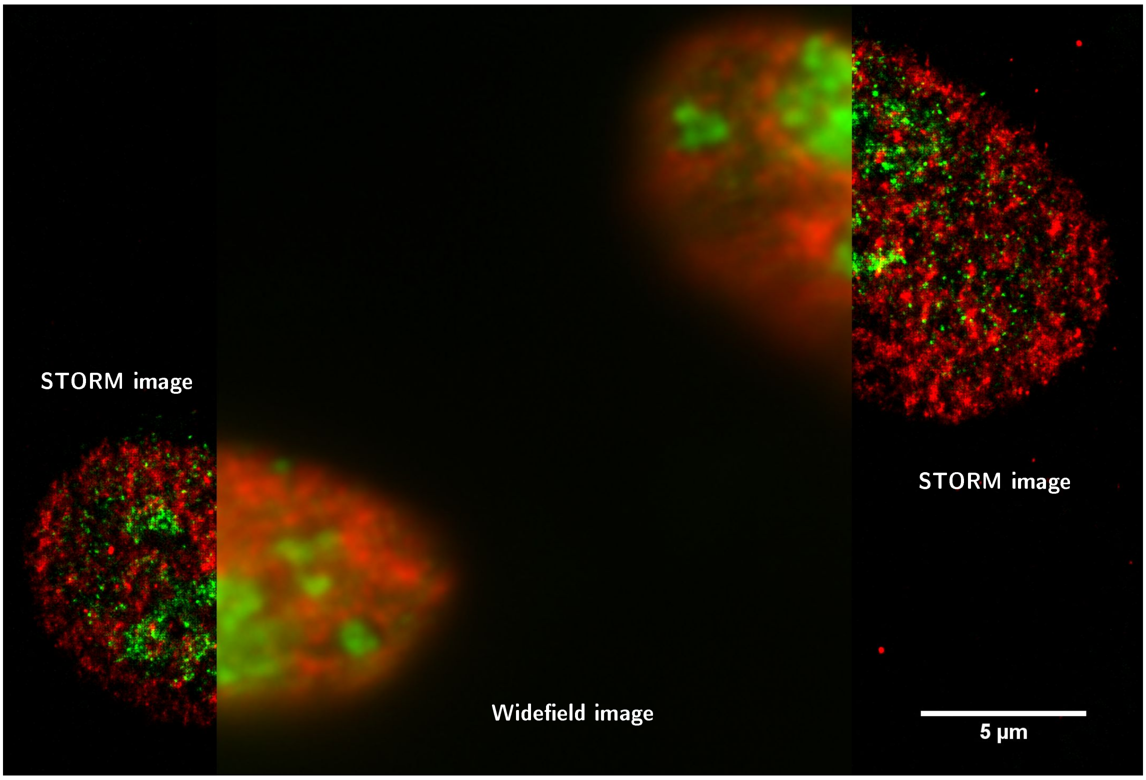

Fig. 3.9 Comparison of visual co-localization analysis using a widefield and SMLM image. Imaging HeLa cells, (red) replicating DNA labeled with Alexa 647-EDU, (green) mRNA from transcriptionally active genes labeled with Fluoroudine, detected with anti-BrDU antibody. The data was processed with ThunderSTORM's default settings, drift correction was applied, and it was rendered with averaged shifted histogram methods.

Coordinate based co-localization

Traditional co-localization analysis of conventional, dual-color fluorescence microscopy images suffers from a limited spatial resolution and chromatic errors (Ronneberger et al., 2008). Coordinate based co-localization (CBC) of dual-color super-resolution images provides much better approach as it allows one to determine co-localization on a molecular level and it is not sensitive to cross talk (Malkusch et al., 2012). For an example see Figure 3.10.

Input: Two lists of coordinates with sub-pixel positions of localized molecules.

Output: CBC value for every molecule.

Calculation of the CBC value around a given molecule A_i, according to (Malkusch et al., 2012), starts by determining two distributions of distances

$$\begin{aligned} \mathrm{D}_{A_i,A}(r) &= \frac{\mathrm{N}_{A_i,A}(r)}{\mathrm{N}_{A_i,A}(r_{\max})} \frac{r_{\max}^2}{r^2}, \\ \mathrm{D}_{A_i,B}(r) &= \frac{\mathrm{N}_{A_i,B}(r)}{\mathrm{N}_{A_i,B}(r_{\max})} \frac{r_{\max}^2}{r^2}. \end{aligned} \tag{3.34}$$

Here $\mathrm{N}_{A_i,A}(r)$, resp. $\mathrm{N}_{A_i,B}(r)$, is the number of localized molecules in channel A, resp. B, within the distance $0 \leq r \leq r_{\max}$ around A_i. These distributions are corrected for the area given by r and normalized by the number of localizations within the largest observed distance $r_{\max}$.

Having these two distributions of distances, Sperman's rank correlation coefficient $\mathrm{S}_{A_i}(r) = \left\langle \mathrm{D}_{A_i,A}(r), \mathrm{D}_{A_i,B}(r) \right\rangle$ is calculated. The co-localization value is determined for every single molecule according to

$$\mathrm{C}_{A_i}(r) = \mathrm{S}_{A_i}(r) \exp\left(-\frac{E_{A_i,B}}{r_{\max}}\right), \tag{3.35}$$

where $E_{A_i,B}$ is a distance from localization A_i to the nearest neighbor localization in channel B.

In ThunderSTORM, the input data for channels A and B are provided as a table of results and a ground-truth table, respectively. Computed values with the co-localization coefficient $\mathrm{C}_{A_i}(r)$, with the distance to the nearest neighbor $E_{A_i,B}$, and with the number of neighbors $\mathrm{N}_{A_i,B}(r)$ within a radius $0 \leq r \leq r_{\max}$, are displayed in the table of results as new columns.

3.8.3 Cluster analysis

Another important application is the analysis of molecular clustering. Several methods have been suggested for identifying and analyzing clusters of molecules, especially cell membrane proteins (Owen et al., 2010, 2012; Rossy et al., 2014). Indeed, measurements

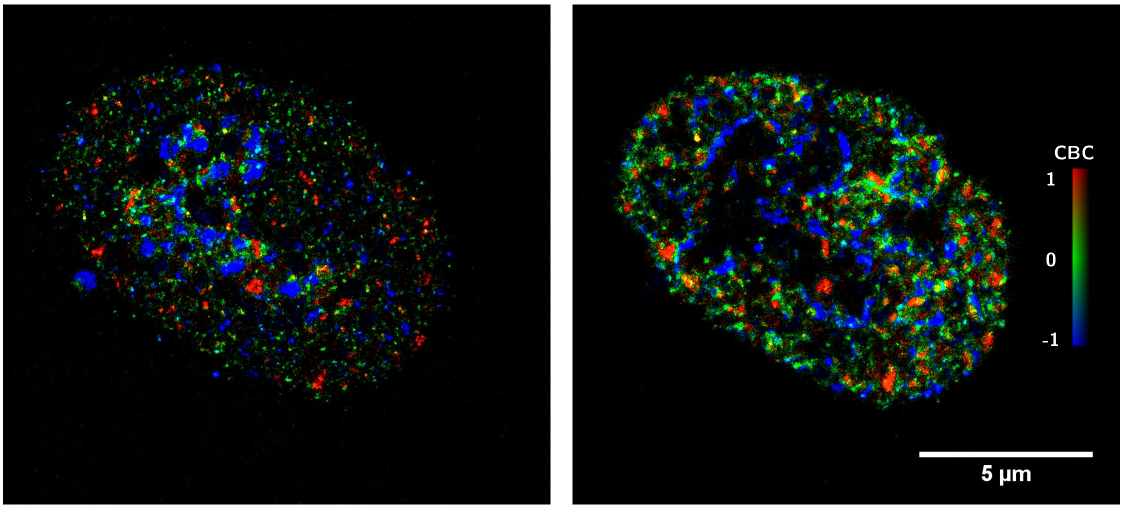

Fig. 3.10 Demonstration of CBC on HeLa cells: red channel - replicating DNA labeled with Alexa 647-EDU; green channel - mRNA from transcriptionally active genes labeled with Fluoroudine, detected with anti-BrDU antibody. In the image colors code CBC values: (left) from green to red channel, (right) from red to green channel. Here we used 10 steps with 10 nm distance increments.

and visualization of potential interactions of membrane proteins has been reenergized by the advent of super-resolution imaging.

Input: A list of coordinates with sub-pixel positions of localized molecules.

Output: Descriptive clustering statistics and set of clusters with the molecules assigned to them.

Although ThunderSTORM currently doesn't implement a cluster classification algorithm, the CBC discussed in the previous section can be, and often is, used for evaluating clustering tendency. This is an important part of the data analysis, which is often performed prior the actual cluster classification. The clustering tendency can be simply calculated by applying CBC algorithm on a single channel, thus setting the channels $A = B$.

3.9 Discussion

Here we discuss some of the decisions that made ThunderSTORM perform well on variety of input data. Since there are plenty of different image filters, spot detectors, and parameter estimators, we decided to perform series of Monte Carlo simulations where we tried different combinations of filters, detectors and estimators to find the best possible processing pipeline. The experiments were performed with different input data with changing signal to noise ratios (SNR).

3.9.1 Effect of image filtering on detection rate

In Sections 3.1 and 3.2 we already described that the detection part of the processing pipeline consists of a wavelet based band pass filter and maximum detector in 8-connected neighborhood with a threshold calculated as the standard deviation of the first wavelet level. Because molecule detection is essential for obtaining high quality results, we demonstrate why the described setting was chosen. We generated several sequences of 1000 frames of 256 × 256 pixels. Each frame contains 70 molecules with fixed FWHM of 300 nm and with different intensities between 200 and 1000 photons. A nonuniform background slowly varying from 3 to 30 photons was added and the resulting image was subjected to Poisson noise. An example of a raw image is displayed in Figure 3.11. Then we analyzed the data using different filters, but with fixed threshold (4× the standard deviation of values in each filtered image) and local maxima detector. Sub-pixel localization step was skipped in this experiment. The detection rate was evaluated using the F1-score.

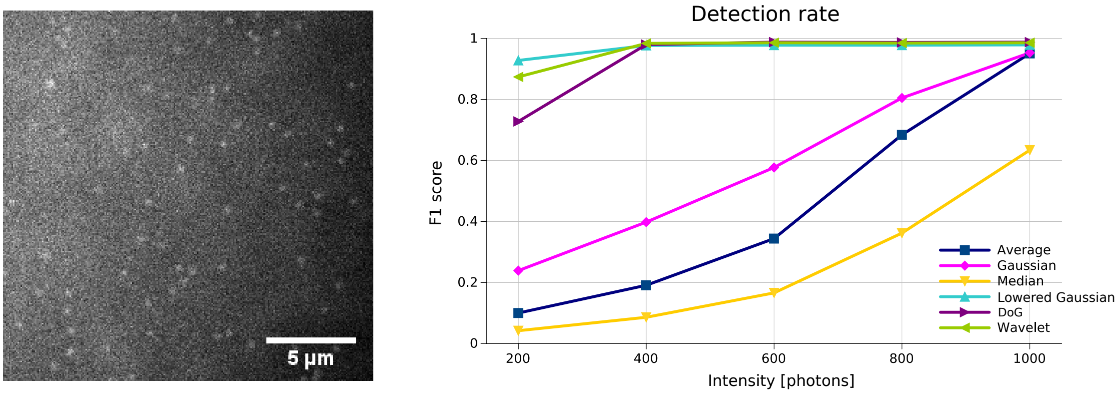

Fig. 3.11 Effect of image filtering on detection rate. Example of raw image (intensity of molecules is 200 photons) on the left, results of the experiment on the right.

The results are shown in Figure 3.11. The bad performance of Gaussian, average, and median filters is due to the fact a nonuniform background was present in the input data and these filters can't remove it because they are low pass filters. On the other hand, lowered Gaussian, difference of Gaussians, and wavelet are all band pass filters, which remove both high frequency noise and low frequency background. See more details about these filters in the supplementary note of (Ovesný et al., 2014a). The reason we chose the wavelet filter for the processing pipeline rather then the other band pass filters is related to the threshold calculation. By testing on multiple artificial and real datasets we determined that a threshold calculated as the standard deviation of the first wavelet level is the most universal and automatically provides great results without any additional input from the user.

3.9.2 Strategies for estimation of axial position

For parameter estimation, it is known that maximum-likelihood estimation (MLE) with an assumption of Poisson noise yields the best results (Mortensen et al., 2010). Although in practice when analyzing data with high SNR, weighted least-squares (WLSQ) give comparable and sometimes even slightly better results. We attribute this to a better numeric stability of our WLSQ implementation compared to our MLE implementation. Also weighted least-squares estimation is much faster since the optimization algorithm uses an analytic Jacobian. Nonetheless, maximum likelihood is still the default option in our processing pipeline.

A more important factor in the localization procedure is the strategy for the determination of z-position. In previously published algorithms, parameters of an elliptic Gaussian $\mathrm{h}_{\mathrm{EG}}\left(x, y \mid \theta_x, \theta_y, \theta_{\sigma_x}, \theta_{\sigma_y}, \theta_N, \theta_o\right)$ were estimated. Then the z-coordinate was determined from calibration curves by least-squares fits of θ_{σ_x} and θ_{σ_y}. In ThunderSTORM we reversed this logic to make σ_x and σ_y functions of a free parameter θ_z, hence the axial position is estimated directly from the PSF model $\mathrm{h}_{\mathrm{EG}}\left(x, y \mid \theta_x, \theta_y, \theta_z, \theta_N, \theta_o\right)$.

To compare the two strategies, we designed an experiment in which we measured the root mean square (RMS) error of axial localizations in a simulated data set. The data was generated similar to the detection experiment described in the previous section. The only differences are that the molecules were generated with intensities uniformly distributed in a range from 500 to 2500 photons and placed on a uniform background of 30 photons. Also, molecules were uniformly distributed along the *z*-axis within a range of ±400 nm and rendered by elliptic Gaussian function to simulate astigmatism. An example of a raw image is displayed in Figure 3.12.

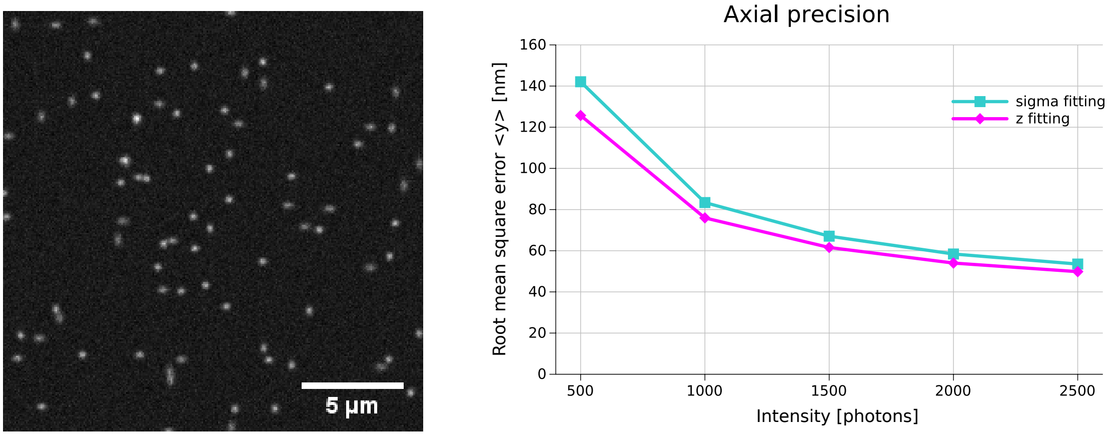

Fig. 3.12 Comparison of different strategies for axial localization. (Left) example of raw image (intensity of molecules is 1500 photons), (Right) results of the Monte-Carlo simulation.

Figure 3.12 shows that our approach performs better across all signal to noise ratios we experimented with. Removing the extra step from the estimation improves the numeric properties of the algorithm. The reason being that the older approach performs a fitting of the widths of the elliptic Gaussian without constraining their mutual relationship. Because of this, the estimator can converge to a combination of widths which are nowhere near the values determined by the calibration curves and consequently we obtain an inaccurate estimate of *z*. In our approach the *z*-position is a free parameter which directly restricts the values of the widths of the elliptic Gaussian during the fitting.

3.10 Chapter summary

ThunderSTORM introduces several new features and concepts for 2D and 3D SMLM data analysis. The software combines several algorithms for SMLM analysis into one comprehensive environment. One of the main features is the ability to process the data using any combination of the implemented feature-enhancing, spot detection, and fitting methods. An important feature in ThunderSTORM is the possibility of specifying the threshold for detection of molecules using mathematical expressions. This allows users to systematically maximize the efficiency of molecule detection in the raw data by searching for the optimum combination, which may vary from experiment to experiment. ThunderSTORM also offers a much higher degree of user-interactivity during data post-processing compared to other SMLM software packages, and introduces a new and fast visualization method which creates high quality results. A realistic data generator within ThunderSTORM allows users to run multi-dimensional Monte-Carlo simulations while evaluating the performance of localization methods. We have found ThunderSTORM's flexibility and performance to be of critical importance when analyzing data with low molecular brightness.

In 2013 a SMLM challenge was held[2] to evaluate nearly 30 software packages using several different simulated and real sets of SMLM data. We submitted ThunderSTORM for the evaluation. As it turned out ThunderSTORM was declared the overall winner in long sequence analyses (Sage et al., 2015), which was one of two categories of the challenge. Recently, a new challenge oriented on 3D SMLM data analysis was announced[3].

---

[2] *SMLM Challenge 2013* available at http://bigwww.epfl.ch/smlm/challenge2013/

[3] *SMLM Challenge 2016* available at http://bigwww.epfl.ch/smlm/challenge2016/

Chapter 4

Dual-objective microscope

Although the astigmatism (Huang et al., 2008a,b) and biplane detection (Juette et al., 2008) offer 3D super-resolution imaging, there can be considerable uncertainty in the estimate of the axial position of each molecule. To improve z-axis localization, the most recent innovations in STORM involve dual-objective detection. These designs collect fluorescence emission from both sides of the sample using two objectives. Published approaches have included interferometric PALM (iPALM) (Shtengel et al., 2009) and 4Pi detection of single molecules (Aquino et al., 2011). Both of these methods offer greatly improved Z-axis localization precision. These approaches both rely on interferometric detection. Unfortunately, it is typically difficult to align and to maintain proper alignment of such systems. Also, the required number of detectors, optical elements and precision optomechanical devices makes these setups prohibitively expensive; for example the original iPALM setup used 3 EMCCD cameras (Shtengel et al., 2009).

A simpler method is dual-objective STORM (Xu et al., 2012, 2013). Here, two images of each molecule are formed on a single camera. This approach roughly doubles the number of collected photons, improving STORM image resolution. It also offers two independent measurements of the axial position of each molecule. This has the effect of dramatically reducing the uncertainty of each axial localization (Xu et al., 2012).

Dual objective STORM offers several advantages over the conventional approach. Because light is detected from both sides of the sample by two objectives, roughly twice the number of photons are collected from each molecule, improving image resolution by a factor of approximately $\sqrt{2}$ (Thompson et al., 2002; Xu et al., 2012). When combined with astigmatic imaging (Huang et al., 2008a,b), the elliptically shaped sub-images of each molecule will be oriented in different directions. These angles are expected to precisely correspond to known angles from calibration data acquired using fluorescent beads. These complementary effects combine to improve the final result by greatly reducing the uncertainty in the axial localization of each molecule. Also, we expect to see each single molecule blinking in unison in the sub-images from the two objectives. This helps distinguish pairs or groups of molecules from truly isolated molecules, thereby reducing false positive detections which degrade the quality of the reconstructed STORM image.

3D super-resolution microscopy based on dual-objective detection will greatly enhance the axial resolution of our images (Xu et al., 2012, 2013). This is crucial for some our projects such as studies of IR and IGF1R receptor clusters, their activation and their signaling pathways as it is required to discriminate between true membrane species and molecules located in early endosomes which are close to the membrane. This is particularly a problem in the very thin CHO cells we wish to use.

Here we introduce our design of a novel dual-objective super-resolution microscope, describe methods for image analysis, and show some of our preliminary results.

4.1 Microscope setup

Our design is based on that of Xu, et al. (Xu et al., 2012, 2013), but it is somewhat simpler, while also being easier to align. A schematic, and photographs of the dual-objective microscope are shown in Figure 4.1. The microscope is equipped with two 100×/1.35NA oil immersion objectives, 405, 473, 532, and 650 nm lasers, and an Andor EMCCD camera. The current sample carrier consists of a micrometer-actuated XYZ stage. The sample is mounted between two high-precision coverslips, then held with rare earth magnets to a piezo-controlled focusing device. This combination allows coarse sample adjustment and focusing followed by nanometer-accurate axial scanning.

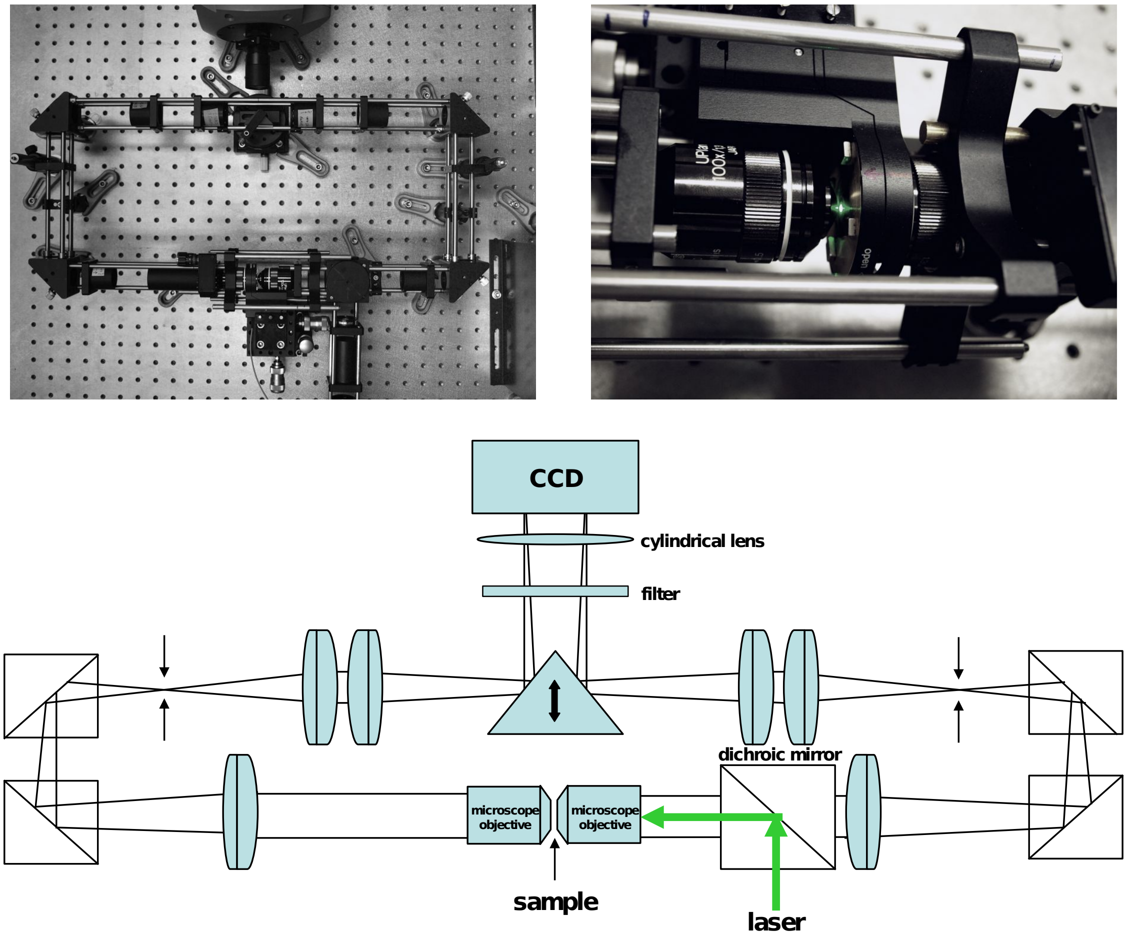

Fig. 4.1 Dual-objective super-resolution microscope built in our lab. Top: Schematic diagram showing the principal components. Bottom: overview photograph and close-up of the piezo-controlled sample holder with two 100×/1.35NA oil immersion objectives.

4.2 Image analysis

Raw data acquired by a dual-objective microscope consist of images of two focal planes (see Figure 4.2 for an example), one for each objective. In analysis, we need to find three-dimensional coordinates of photo-active emitters. Note that there are few options how to setup the acquisition. There might be a cylindrical lens placed in front of the camera to introduce astigmatism in both images (Xu et al., 2012) or there might be no astigmatism so only the defocus between the planes is used to determine the z-position (Ram et al., 2007, 2009) or it can be a hybrid setup such as in (Min et al., 2014a), where astigmatism is introduced in just one image. Our microscope is set up for simultaneous acquisition of two images and a cylindrical lens is optionally introduced in front of the camera, similar to (Xu et al., 2012). This way we are able to acquire information from up to four focal planes at once with a relatively simple setup. Each objective can be focused in a different plane and both images are additionally defocused into two other focal planes using the astigmatism. This in combination with doubled photon counts leads to significantly improved resolution in the z-axis.

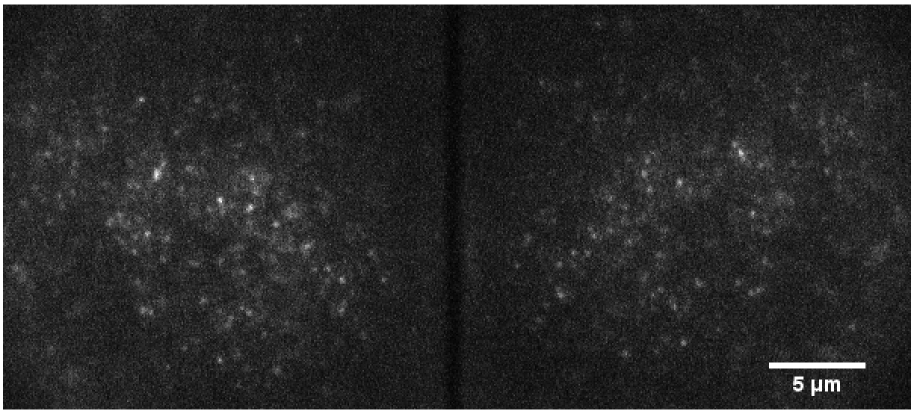

Fig. 4.2 Example of raw image acquired by our dual-objective microscope with astigmatism.

4.2.1 Calibration

First, a calibration needs to be performed. The calibration is performed on a stack of images of fluorescent beads of subdiffraction size and high photon emission rate. Once the stack is acquired, we need to find a geometric transform from one image to the other so the spots can be paired up as images of individual emitters. Then defocusing curves are estimated.

The algorithms described below expect two image sequences of the same dimensions on the input, one for each objective. However, possible extension for more images is straightforward. For emitter fitting we use the elliptic Gaussian function as defined in Equation (2.2). If astigmatism is not used, it is straightforward to fix $\theta_{\sigma_x} = \theta_{\sigma_y}$, $\phi = 0$ and skip the angle estimation step during the calibration. Other than that, everything is identical for all the variations of the microscope setup.

Determining the orientation angle

First, localization is run in both images separately with orientation angle as a free parameter. Then the angle is determined as described in Section 3.4. Once the angle is known, the parameters of the elliptic Gaussian are estimated with the fixed angle. The result for each image is a set of 2D positions in the image, widths of the Gaussian, integral intensity of the fluorescent bead, and DC offset. All these parameters are determined for each slice of the calibration stack with known z-step, just like in calibration for astigmatic imaging. Spots found in different slices of the stack located around the same lateral position are grouped together as they likely are created by the same bead. Groups with low number of assigned spots are eliminated from further processing.

Finding the homography

For each group found in the previous step we calculate the mean lateral position of all assigned spots. The input for this step of the algorithm is a set containing the mean positions $(x_i^{(1)}, y_i^{(1)})$, $(x_i^{(2)}, y_i^{(2)})$ representing beads found in the first and in the second image respectively.

For homography estimation we use a normalized direct linear transform (DLT) algorithm (Hartley, 1997; Longuet-Higgins, 1981). Since the DLT algorithm assumes pairs of coordinates as the input and the mutual correspondences of molecular coordinates are not known, the random sample consensus (Fischler and Bolles, 1981) (RANSAC) algorithm is used to randomly sample the coordinates to make the pairs. This is a common approach for homography estimation in computer vision (Hartley and Zisserman, 2003). Individual steps of the algorithm are carried out in more detail below.

2D Direct Linear Transform algorithm Working in homogeneous coordinates, the mapping between two corresponding points $(x_i^{(1)}, y_i^{(1)})$ and $(x_i^{(2)}, y_i^{(2)})$ can be written as

$$\begin{pmatrix} x_i^{(2)} \\ y_i^{(2)} \\ 1 \end{pmatrix} = H \begin{pmatrix} x_i^{(1)} \\ y_i^{(1)} \\ 1 \end{pmatrix}, \tag{4.1}$$

where $H = \begin{pmatrix} h_1 & h_2 & h_3 \\ h_4 & h_5 & h_6 \\ h_7 & h_8 & h_9 \end{pmatrix}$ is a transformation matrix. By expanding the previous equation and normalizing with respect to the homogeneous component, we obtain

$$x_i^{(2)} = \frac{h_1 x_i^{(1)} + h_2 y_i^{(1)} + h_3}{h_7 x_i^{(1)} + h_8 y_i^{(1)} + h_9} \quad \text{and} \quad y_i^{(2)} = \frac{h_4 x_i^{(1)} + h_5 y_i^{(1)} + h_6}{h_7 x_i^{(1)} + h_8 y_i^{(1)} + h_9} \,. \tag{4.2}$$

Vectorizing H to $\boldsymbol{h} = \begin{pmatrix} h_1 & h_2 & h_3 & h_4 & h_5 & h_6 & h_7 & h_8 & h_9 \end{pmatrix}$ and rearranging the Equation (4.2) yields the following two linear equations

$$\begin{aligned} \begin{pmatrix} x_i^{(1)} & y_i^{(1)} & 1 & 0 & 0 & 0 & -x_i^{(2)} x_i^{(1)} & -x_i^{(2)} y_i^{(1)} & -x_i^{(2)} \end{pmatrix} \boldsymbol{h} = 0\,, \\ \begin{pmatrix} 0 & 0 & 0 & x_i^{(1)} & y_i^{(1)} & 1 & -y_i^{(2)} x_i^{(1)} & -y_i^{(2)} y_i^{(1)} & -y_i^{(2)} \end{pmatrix} \boldsymbol{h} = 0\,, \end{aligned} \tag{4.3}$$

which can be further rewritten as $A_i \boldsymbol{h} = 0$. It is obvious that one pair of corresponding points yields two equations. Picking four pairs directly leads to an eight-point algorithm forming an 8×9 matrix. Thus to find the transform H, we need to solve

$$\hat{h} = \arg\min_{h} \|A\boldsymbol{h}\| \text{ subject to } \|\boldsymbol{h}\| = 1\,, \tag{4.4}$$

where $A = \begin{pmatrix} A_1 & A_2 & A_3 & A_4 \end{pmatrix}^{\top}$. The solution of the previous equation is the eigenvector of $A^{\top}A$ associated with the smallest eigenvalue.

Normalization It is well known that one can experience numerical issues with the DLT algorithm. It was proposed (Hartley, 1997) to normalize the input points such that the centroid $(\bar{x}, \bar{y})$ of all points on each image is at the origin $(0,0)$. The average Euclidean distance of all points from the centroid is then $\sqrt{2}$. This normalization yields a transformation matrix acting as a preconditioner to make the DLT algorithm more numerically stable.

Working with a single image and set of input points (x_i, y_i), we look for a normalizing similarity transform T such that

$$\begin{pmatrix} \tilde{x}_i \\ \tilde{y}_i \\ 1 \end{pmatrix} = T \begin{pmatrix} x_i \\ y_i \\ 1 \end{pmatrix} = \begin{pmatrix} s & 0 & t_x \\ 0 & s & t_y \\ 0 & 0 & 1 \end{pmatrix} \begin{pmatrix} x_i \\ y_i \\ 1 \end{pmatrix}, \tag{4.5}$$

where $(\tilde{x}_i, \tilde{y}_i)$ is a normalized point, $(t_x = -s\bar{x}, t_y = -s\bar{y})$ is a translation vector towards the centroid, and s is an isotropic scale

$$s = \frac{\sqrt{2}}{\frac{1}{n}\sum_{i=1}^{n} \sqrt{(x_i - \bar{x})^2 + (y_i - \bar{y})^2}}. \tag{4.6}$$

The normalized DLT algorithm works as follows:

1. For both images find the normalizing transforms and normalize the input points to obtain T_1, T_2 and $\left(\tilde{x}_i^{(1)}, \tilde{y}_i^{(1)}\right)$, $\left(\tilde{x}_i^{(2)}, \tilde{y}_i^{(2)}\right)$.
2. Estimate the normalized homography $\tilde{H}$ using the DLT algorithm on the input points $\left(\tilde{x}_i^{(1)}, \tilde{y}_i^{(1)}\right)$, $\left(\tilde{x}_i^{(2)}, \tilde{y}_i^{(2)}\right)$.
3. The final estimated homography is $\hat{H} = T_2^{-1} \tilde{H} T_1$.

Finding point correspondences Since correspondences of points between the images are not known in advance and the DLT algorithm assumes that the points are paired so the homography can be correctly estimated, this motivates application of a randomized iterative algorithm such as RANSAC (Fischler and Bolles, 1981). Applied to our problem, the algorithm is as follows:

1. Randomly select 4 points from each image.
2. Solve the homography H using the normalized DLT algorithm using the selected pairs.
3. Transform all points $(x_i^{(1)}, y_i^{(1)})$ using H to $(\hat{x}_i^{(1)}, \hat{y}_i^{(1)})$. Pair up the points using the Gale-Shapley algorithm (Gale and Shapley, 1962) with the Euclidean distance used as

weights on the edges of a complete bipartite graph representing all possible pairs of points. Mark the pairs within a threshold distance ε as inliers.

4. If the fraction of inliers is greater or equal to the best result found in previous iterations, re-estimate the homography H using the normalized DLT algorithm using all the pairs marked as inliers. Store the homography H with more inliers as the best result. If the number of inliers of the new model equals the number of inliers of the previously estimated model, pick the one with the minimum sum of mutual distances as the best one.

5. Repeat the steps 1 through 4 n times.

The number of iterations n is chosen high enough to find a good homography. There are different probabilistic tools in the literature (Fischler and Bolles, 1981; Hartley and Zisserman, 2003) to find n and to determine preverification steps to stop the iterations when the result is good enough according to a certain criteria. However, in our calibration data we deal with a low number of points and the time of computation is not an issue, thus, we fix $n = 1000$, which in our experiments gives reliable results with low run time ($\approx 1s$).

Estimating the defocusing curves

At this point, we already know the orientation angle ϕ and other parameters of the PSF model $\theta = \left\{\theta_x, \theta_y, \theta_{\sigma_x}, \theta_{\sigma_y}, \theta_N, \theta_o\right\}$ for each emitter and we also know which pair of spots represent each individual calibration bead. Now recall the defocusing curves from Equation (3.16), which describe the widths of Gaussians as functions of the axial position of emitters. The estimation procedure is the same as described in Section 3.4, only with the exception that since there are now two images per z-position for a single emitter, there are four defocusing curves $\sigma_x^{(1)}(z)$, $\sigma_y^{(1)}(z)$, $\sigma_x^{(2)}(z)$, $\sigma_y^{(2)}(z)$. See Figure 4.3 for example.

4.2.2 3D position estimation

A simple way to perform the estimation would be to follow (Xu et al., 2012), where the authors run parameter estimation separately for each plane, then they filter out molecules

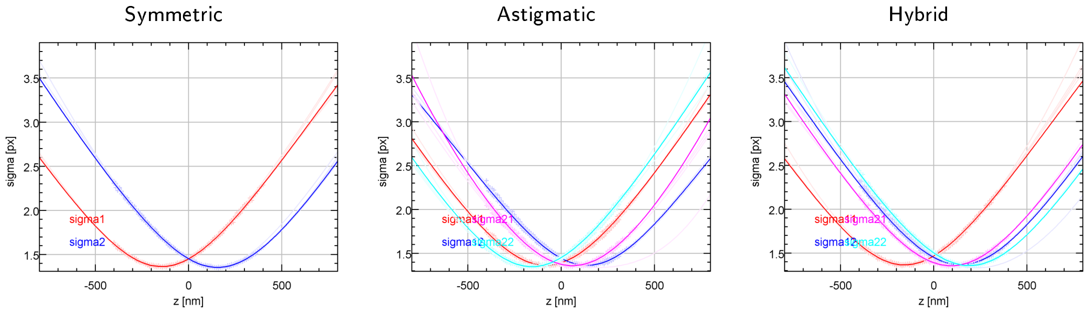

Fig. 4.3 Example of calibration curves. The graphs are results of ThunderSTORM's calibration procedure on calibration data sets generated to simulate different combinations of biplane and astigmatism, i.e., symmetric (no astigmatism), astigmatic (astigmatism in both planes), hybrid (astigmatism in a single plane). Here $\sigma_x^{(1)} = \text{sigma11}$, $\sigma_y^{(1)} = \text{sigma12}$, $\sigma_x^{(2)} = \text{sigma21}$, $\sigma_y^{(2)} = \text{sigma22}$. In the symmetric setup $\sigma_y^{(1)} = \sigma_x^{(1)}$ and $\sigma_y^{(2)} = \sigma_x^{(2)}$.

which have parameters that differ more than a certain threshold. Finally, the parameters for each molecule are averaged together to obtain a better estimate. This is certainly one possible algorithm, but it does not utilize all the information during the fitting. A much better approach is to run the parameter estimation in both original images simultaneously. The issue here is the two images are not aligned. An intuitive solution would be to apply the homography to transform the first image to align with the second one and then run the fitting. This would create an interpolation error even before we start the estimation, thus again the information content would be hindered.

Our solution, integrated in ThunderSTORM, performs simultaneous fitting in both imaged planes. To maintain as much information as possible, we first precompute a grid of coordinates that maps the two images one to the other, then pair up the spots detected in the two images and make initial estimates of their parameters. Finally, we run the estimation with either the least-squares or the maximum-likelihood estimation as described in Section 3.3. No extra image transformations are required. The algorithm is carried out below:

1. Prepare grids of x,y coordinates for both images of size $w \times h$:

$$\mathcal{X}^{(1)} = \begin{pmatrix} 1 & \dots & w \\ \vdots & \ddots & \vdots \\ 1 & \dots & w \end{pmatrix}, \mathcal{Y}^{(1)} = \begin{pmatrix} 1 & \dots & 1 \\ \vdots & \ddots & \vdots \\ h & \dots & h \end{pmatrix}, \begin{pmatrix} \mathcal{X}^{(2)}_{i,j} \\ \mathcal{Y}^{(2)}_{i,j} \\ 1 \end{pmatrix} = H \begin{pmatrix} \mathcal{X}^{(1)}_{i,j} \\ \mathcal{Y}^{(1)}_{i,j} \\ 1 \end{pmatrix}, \tag{4.7}$$

where $\{i, j \in \mathbb{Z} \mid 1 \leq i \leq w, 1 \leq j \leq h\}$.

2. Use the homography H to map coordinates of spots from the first image into the second one. Then find a stable matching based on the Euclidean distance between the points from both images using the Gale-Shapley algorithm (Gale and Shapley, 1962). We further process only the pairs of points with mutual distance lower than a threshold.

3. Extract a fitting subregion $\mathscr{D}$ centered around the detected spots in both images as described in Section 3.3. Note that we introduce the following symbolic simplifications:

$$\begin{aligned} \mathfrak{h}^{(k)}(x,y) &= \mathrm{h}_{\mathrm{EG}}\left(x, y, \phi_k, \sigma_x^{(k)}, \sigma_y^{(k)} \mid \theta_x, \theta_y, \theta_z, \theta_N, \theta_{o_k}\right), \\ \mathcal{X}^{(k)}_{x,y} &= \mathcal{X}^{(k)}(x,y), \\ \mathcal{Y}^{(k)}_{x,y} &= \mathcal{Y}^{(k)}(x,y). \end{aligned} \tag{4.8}$$

For least-squares estimation we define a chi-squared function as

$$\chi^2(\theta \mid \mathscr{D}) = \sum_k \left[\sum_{(x,y)\in\mathscr{D}} \left(I^{(k)}\left(\mathcal{X}^{(k)}_{x,y}, \mathcal{Y}^{(k)}_{x,y}\right) - \mathfrak{h}^{(k)}\left(\mathcal{X}^{(k)}_{x,y}, \mathcal{Y}^{(k)}_{x,y}\right) \right)^2 \right], \tag{4.9}$$

the sum squared residuals for k-th image. Similarly, the product of likelihoods for maximum-likelihood estimation is

$$\mathcal{L}(\theta \mid \mathscr{D}) = \prod_k \left[\prod_{(x,y)\in\mathscr{D}} \frac{\mathfrak{h}^{(k)}\left(\mathcal{X}^{(k)}_{x,y}, \mathcal{Y}^{(k)}_{x,y}\right)^{I^{(k)}\left(\mathcal{X}^{(k)}_{x,y}, \mathcal{Y}^{(k)}_{x,y}\right)} \exp\left(-\mathfrak{h}^{(k)}\left(\mathcal{X}^{(k)}_{x,y}, \mathcal{Y}^{(k)}_{x,y}\right)\right)}{I^{(k)}\left(\mathcal{X}^{(k)}_{x,y}, \mathcal{Y}^{(k)}_{x,y}\right)} \right]. \tag{4.10}$$

To make the description of the algorithm complete, recall the astigmatic PSF model (Equation (2.2)) we use here

$$\mathfrak{h}^{(k)}(x,y) = \frac{\theta_N}{2\pi\sigma_x^{(k)}(\theta_z)\,\sigma_y^{(k)}(\theta_z)}\exp\left(-\frac{\mathrm{x}(x,y,\phi \mid \theta_x,\theta_y)^2}{2\sigma_x^{(k)}(\theta_z)^2}-\frac{\mathrm{y}(x,y,\phi \mid \theta_x,\theta_y)^2}{2\sigma_y^{(k)}(\theta_z)^2}\right)+\theta_o\,, \tag{4.11}$$

$$\mathrm{x}(x,y,\phi \mid \theta_x,\theta_y) = (x-\theta_x)\cos\phi-(y-\theta_y)\sin\phi\,, \tag{4.12}$$

$$\mathrm{y}(x,y,\phi \mid \theta_x,\theta_y) = (x-\theta_x)\sin\phi+(y-\theta_y)\cos\phi\,. \tag{4.13}$$

4.3 Experimental results

In the following text we first discuss and experimentally justify our choices when designing the 3D fitting algorithm for biplane microscopy and we compare the results to Xu's algorithm (Xu et al., 2012). Next, we experimentally compare different optical setups available when imaging with two objectives. Finally, we show some of our preliminary data acquired with our setup.

4.3.1 Algorithm design rationale

In (Xu et al., 2012) authors proposed to run the localization in each plane separately, then filter out inaccurate fits based on a comparison of estimates from both planes, and finally, they average the remaining fits from both planes together to further improve the estimates. Here we hypothesize that in this approach part of the information contained the raw data is actually lost when the fitting is performed separately. In our algorithm, we perform simultaneous fitting in both images to obtain better results. To show this, we designed a Monte-Carlo simulation consisting of 1000 images, each $2 \times 256 \times 256$ pixels in size and containing 10 molecules rendered as if they were imaged by a biplane setup. The molecules were axially distributed in a range of ± 400 nm and their intensity varied between 500 and 3000 photons. The molecules were placed on a uniform background of 70 photons and the images were corrupted by Poisson noise. Then we compared the two algorithms with respect to detection rate (F1-score) and localization accuracy (root mean square of 3D Euclidean distances between ground truth and the estimated positions).

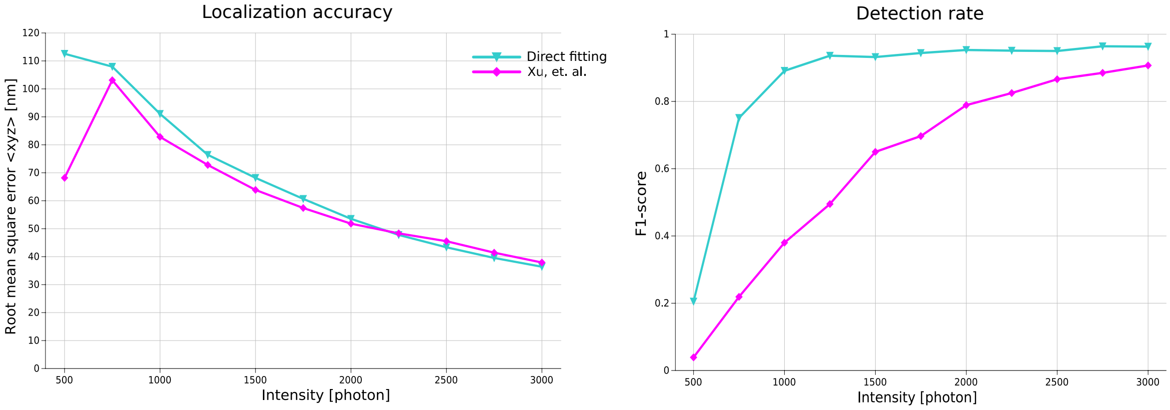

Fig. 4.4 Comparison of two different strategies for axial localization.

Figure 4.4 shows that indeed our approach provides higher detection rate. Note that a detection was counted as a true positive if it was laterally localized within a 50 nm radius around its ground truth position.

Although the graph of localization accuracy shows slightly worse performance of our method, this can be attributed to the fact that we detected many more molecules within the 50 nm radius which on average made the localization error higher. To verify this, we filtered the results of our method to contain only detections of the same ground-truth molecules as in Xu's method. Then we reevaluated the localization accuracy, which showed our method achieved slightly better precision (≈ 1 nm). Hence, we conclude the simultaneous fitting method provides overall better performance.

4.3.2 Astigmatism in a biplane setup

It is possible to add a cylindrical lens in front of the camera in a dual-objective microscope (Xu et al., 2012). It is also possible to add the lens into just one of the detection paths (Min et al., 2014a), or the imaging can be performed with no astigmatism at all. Our method is independent of such changes in the microscope setup. Thus, we want to evaluate which setup is the most advantageous to obtain the best results. For this purpose we designed an experiment where we generated three simulated data sets, one for astigmatism in both planes, second for astigmatism in a single plane and third with no astigmatism. The individual data sets consists of 1000 images, each $2 \times 256 \times 256$ pixels in size generated with the same parameters as in the previous experiment in Section 4.3.1.

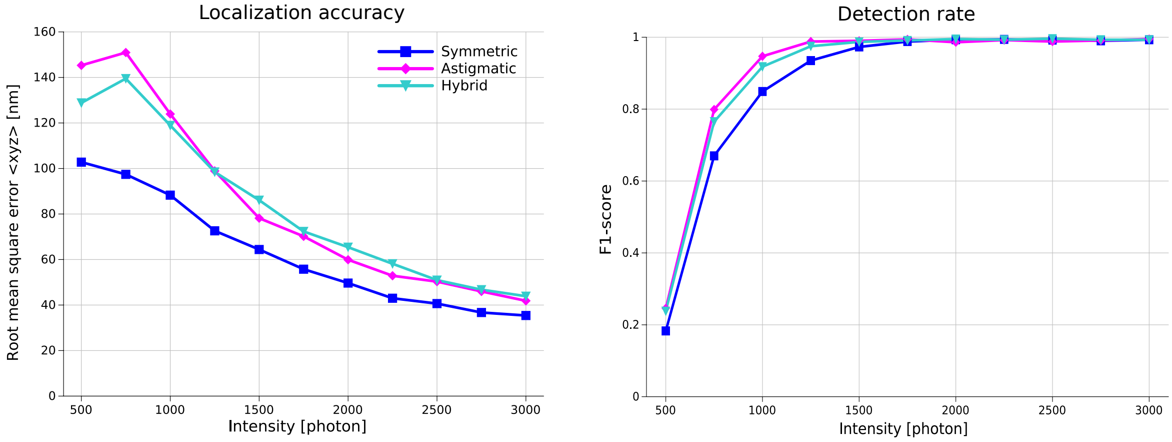

Fig. 4.5 Localization accuracy and detection rate with different PSFs.

In Figure 4.5 we see the setup with no astigmatism gives the best localization accuracy, however the detection rate is the worst of all three. Again, like in the previous experiment, these two quantities are closely related. However, even when the detection rates are equal, the precision provided by the symmetric PSF is still the best by a significant margin. Width of this margin is inversely proportional to SNR. We ascribe this to the fact that a cylindrical lens blurs the imaged PSF. Consequently, the photons detected from a molecule are distributed over a larger area in the image. This means the peak intensity of the molecule is lower and contours at the boundary of the molecule are practically invisible due to the presence of noise. When these factors are combined, it becomes difficult for an estimation procedure to find the correct parameters.

4.3.3 Real cell imaging

To show an example of real cell imaging with our dual objective microscope, we acquired 1000 frames of a U2-OS cell densely labeled for tubulin. 3D information was extracted from mutual defocus of the microscope's two objectives. Additionally, cross-correlation based drift correction was applied, and the super-resolution image was rendered. The result is shown in Figure 4.6.

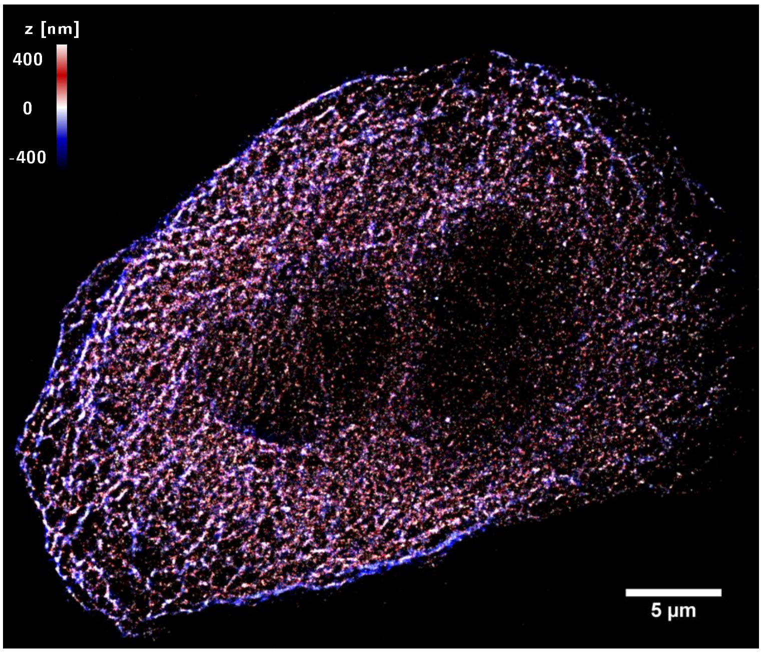

Fig. 4.6 Imaging of tubulin in U2-OS cells with dual objective microscope.

4.4 Chapter summary

We constructed a prototype dual-objective single molecule localization microscope with the objectives placed on opposite sides of the sample. This is one of only a few such systems in the world and is a completely unique project in the Czech Republic. Compared to the classical single objective solution, the new microscope further improves resolution, particularly in the axial direction. We designed and implement advanced data analysis tools, and developed the calibration and data acquisition protocols necessary for enhanced resolution. The developed methods have been added into ThunderSTORM. Moreover, we demonstrated good performance of the developed methods and showed that our approach to data analysis outperforms the previously published approach. In addition, we imaged tubulin in U2-OS cells to verify application of the microscope and the analysis tools on a real biological sample.

Although the prototype dual-objective microscope is assembled in our laboratory, it will require further development to be really useful for routine imaging. Specifically, one of the challenges is to improve the sample holder, because the current setup is susceptible to misalignment when exchanging samples. Also, we need to perform more measurements to better understand the real properties of the microscope.

One of the main applications of the microscope is for our projects concerning receptors in the plasma membrane of mammalian cells. The proposed microscope and data analysis methods will allow acquisition of multi-color, 3D super-resolution images. With this data we can measure parameters such as count of molecules and their density. We can also evaluate phenomena such as clustering directly and efficiently.

Chapter 5

Improving temporal resolution of 3D SMLM

One drawback of SMLM is the fact that recording a long sequence of diffraction limited images is required for reconstruction of a single super-resolution image. This problem has been addressed by increasing the density of photoactivated fluorophores, thus the same number of molecules can be acquired within a shorter sequence, which effectively increases the temporal resolution and thus expands the possibilities for applying SMLM to the observation of dynamic processes in live cells (Subach et al., 2010). However, when increasing the density, the images of the molecules start to overlap which poses a challenge in the analysis of such images. The goal of image analysis is then to detect the blinking events without a significant drop in spatial resolution. This renders the classical approach described in the previous chapters not applicable for high density imaging.

The first attempts to analyze such images were based on drawing a fitting region around isolated groups of molecules and then fitting multiple molecules. Some of these include multi-emitter fitting analysis (Huang et al., 2011) or DAOSTORM (Holden et al., 2011), which was further extended for 3D analysis (Babcock et al., 2012).

Later, new concepts were introduced which apply advanced techniques for spatial localization using ideas from the field of compressed sensing (Donoho, 2006) and some of them also incorporate the temporal information of intensities changing throughout the sequence.

The idea of using reconstruction techniques from compressed sensing was first introduced in CSSTORM (Zhu et al., 2012). The main trick is to estimate a super-resolution image for each frame of the sequence using an optimization program with non-linear constraints, such as non-negativity and sparsity. Then the molecules are detected as local maxima in the estimated super-resolution image. This method has proven to be robust to noise and to provide much higher detection rates compared to multiple-emitter fitting. On the other hand the method is also very computationally intensive and has high demands on memory. This was addressed by applying an ℓ_1-homotopy method (Babcock et al., 2013) which made the computation orders of magnitude faster, but this didn't solve the problem with high demands on memory. Therefore the analysis was practically limited to 2D images and only small regions could be analyzed at one time, therefore the image had to be divided into overlapping tiles which were analyzed and the results combined together. A new fast algorithm called FALCON (Min et al., 2014b) solved the issues with memory and thus could be applied to larger images and was recently extended for 3D analysis (Min et al., 2014a).

It is important to recall that low-light images are subject to photon counting noise which follows Poisson statistics (Hecht, 2001). This phenomenon can be a limiting factor for successful image reconstruction, especially when imaging in extreme low-light conditions with short exposure times. However, correctly handling Poisson distributed noise can lead to difficult optimization problems. This is perhaps one reason why most of the current algorithms based on compressed sensing use a Gaussian noise model. This was recently addressed in our new algorithm, 3denseSTORM (Ovesný et al., 2014b), where the more precise Poisson noise model was assumed. This algorithm is capable of both 2D and 3D analysis and is fast and memory efficient.

The temporal information, that is the changes in intensities throughout the sequence, can be used to isolate individual blinking events as was shown in gSHRImP (Simonson et al., 2011). It is also possible to analyze the sequence as a whole assuming blinking statistics formulated as a Markov process as was done in deconSTORM (Mukamel et al., 2012) or 3B (Cox et al., 2012). It is worth noting that even though 3B presents an interesting mathematical model which delivers state of the art results, its computational complexity is so high that a computer cluster is required to obtain any results, even in small images.

Recently, another method based on non-negative matrix factorization was introduced (Mandula et al., 2014). This method was designed to make super-resolution imaging with quantum dots possible and is also based on the analysis of the whole sequence. Using quantum dots as a fluorescent label has its specifics as they have different blinking kinetics than fluorophores usually used for STORM experiments, thus they require a specialized algorithm. But they provide greater photostability and have much higher brightness than fluorescent proteins or organic dyes so it might help to further increase the temporal resolution.

In this chapter we introduce our algorithm for localization microscopy, 3denseSTORM (Ovesný et al., 2014b), which is able to reconstruct 3D super-resolution images from a sequence of diffraction limited images with high densities of photoactivated molecules. The algorithm is based on a combination of sparse support recovery and maximum-likelihood estimation and uses a Poisson noise model. For 3D imaging experiments we use astigmatism (Huang et al., 2008b), biplane detection (Juette et al., 2008), and dual objective STORM (Xu et al., 2012) methods, however the algorithm is flexible enough to allow 3D localization of molecules by other approaches such as the double helix point spread function method (Pavani et al., 2009). We demonstrate that the proposed algorithm performs well in low-light conditions and with high molecular density, making it suitable for fast image acquisition in densely labeled samples. We also derive the theoretical resolution limits of the method. Finally, we experimentally validate the algorithm on simulated and real data and show that it outperforms the other current methods in the field.

5.1 Theory

Below we formulate the 3denseSTORM algorithm and carry out its theoretical resolution limits.

5.1.1 Problem formulation

In a SMLM experiment, imaging can be described as a convolution of photoactivated fluorophores in the sample (point-sources of light) with a kernel described by the point spread function (PSF) of the microscope. We construct the convolution operation as a matrix multiplication of the signal $\mathbf{x}$ by a Toeplitz matrix H in which each column is a shifted copy of a vectorized convolution kernel given by the PSF. Because photon counting processes follow Poisson statistics (Hecht, 2001), the image formed in the camera can be modeled by

$$\hat{\mathbf{y}} = \mathcal{P}\left(H\mathbf{x} + \mathbf{b}\right) . \tag{5.1}$$

Here $\hat{\mathbf{y}} = \left[\hat{y_1}, \ldots, \hat{y_m}\right]^\top$ is a vectorized camera image with m elements (pixels), $\mathbf{x} = \left[x_1, \ldots, x_n\right]^\top$ is a vectorized, oversampled grid with $n \gg m$ discrete pixels with values representing the intensity of molecules at the corresponding positions in the sample, $\mathbf{b} = \left[b_1, \ldots, b_m\right]^\top$ is the vectorized background intensity of the sample at corresponding camera pixels, H is a Toeplitz matrix of size $m \times n$, and $\mathcal{P}$ is the Poisson noise operator. All image intensities are expressed in photon counts.

To recover an unknown signal $\mathbf{x}$ from measurements $\mathbf{y}$ acquired by the camera, we need to solve the inverse problem posed by Equation (5.1). Suppose that the number of photons collected by a single camera pixel follows the Poisson distribution and that all measurements are independent and identically distributed. The joint density function for all measurements can be expressed as a likelihood function of unknown parameters $\mathbf{x}$ and $\mathbf{b}$,

$$p\left(\mathbf{y}|\mathbf{x}, \mathbf{b}\right) = \prod_{i=1}^{m} \left(\frac{\left(H\mathbf{x} + \mathbf{b}\right)_i^{y_i}}{y_i!} \exp\left(-H\mathbf{x} - \mathbf{b}\right)_i \right) . \tag{5.2}$$

Here y_i is the number of photons measured by a particular camera pixel $i = 1, \ldots, m$, and the expected number of photons in that pixel is given by $\bar{y}_i = \left(H\mathbf{x} + \mathbf{b}\right)_i$.

This problem is ill-posed, since $n \ll m$, and solving it by conventional maximum likelihood estimation methods would not give a stable solution. Following the principles of compressed sensing (Donoho, 2006), additional information that the signal is sparse, i.e., mostly zeroes, can be utilized by introducing a regularization term. This, together with the fact that the signal **x** is nonnegative, leads to the choice of an exponential prior

$$p(\mathbf{x}) = \prod_{j=1}^{n} \left(w_j \exp\left(-w_j x_j \right) \right) , \tag{5.3}$$

where $\mathbf{w} = [w_1, \cdots, w_n]^\top$ is a vector of nonnegative weights. With this prior information, we can transform the ill-posed maximum-likelihood problem into a well-posed maximum *a posteriori* problem

$$\left\{ \hat{\mathbf{x}}, \hat{\mathbf{b}} \right\} = \operatorname*{arg\,min}_{\mathbf{x},\mathbf{b} \in \mathbb{R}^n_{\geq 0}} \left\{ \sum_{i=1}^{m} \left[(H\mathbf{x} + \mathbf{b})_i - y_i \ln (H\mathbf{x} + \mathbf{b})_i \right] + \sum_{j=1}^{n} w_j x_j \right\} . \tag{5.4}$$

This optimization problem is difficult to solve, because the Poisson log-likelihood term does not have a Lipschitz-continuous gradient, therefore the Hessian matrix, which is often used by optimization algorithms, is severely ill-conditioned and the optimization fails to converge. This problem has become a topic of an active research and recently there have been several solutions proposed, mainly based on relaxation or approximation schemes. The simplest approach is to apply a variance stabilizing transform such as the Anscombe transform (Dupé et al., 2009). Another method uses a linear approximation of the Hessian around the point of evaluation (Harmany et al., 2009). Other methods apply variable splitting and the augmented Lagrangian method (Figueiredo and Bioucas-Dias, 2009), which together form the basis for the alternating direction of multiplier method (ADMM) (Figueiredo and Bioucas-Dias, 2010) and its close relative, the split Bregman method (Setzer et al., 2010). There are also other probability-based methods employing maximum-likelihood expectation-maximization algorithms (Mukamel et al., 2012).

5.1.2 Detection of molecules using sparse support recovery

Our approach is based on ADMM (Figueiredo and Bioucas-Dias, 2010), mainly because of the fast convergence of this algorithm and positive results reported in the literature. Following the ADMM optimization scheme, we decomposed the complex problem in Equation (5.4) into a series of simpler sub-problems described by Equations (5.5)-(5.9).

The optimization process is based on the following iterative scheme, where $k = 0, 1, 2, \ldots$ denotes the iteration. First, the sample background $\hat{\mathbf{b}}^{(k)}$ is estimated from the image $\hat{\mathbf{y}}^{(k)}$ using an iterative low-pass filtering algorithm (Galloway et al., 2009). Then a vector of weights for the regularization term in Equation (5.4) is chosen proportional to the local uncertainty of the background (Min et al., 2014b). Because the data follows a Poisson distribution we use $\mathbf{w}^{(k)} = \mathrm{f}\left(\beta\sqrt{\hat{\mathbf{b}}^{(k)}}\right)$. Here $\mathrm{f}(\cdot)$ is a function which interpolates the estimated low-resolution background image $\hat{\mathbf{b}}^{(k)}$ to each element of the high-resolution signal $\mathbf{x}$. Next, the iterative scheme alternates between regularized least-squares estimates $\hat{\mathbf{x}}^{(k)}$ of the unknown signal $\mathbf{x}$ in Equation (5.5) and maximum-likelihood estimates $\hat{\mathbf{y}}^{(k)}$ of the measured image $\mathbf{y}$ in Equation (5.6). Simultaneously, sparse and non-negative solutions are enforced by Equation (5.7). The overall scheme can be written as

$$\hat{\mathbf{x}}^{(k+1)} = \underset{\mathbf{x}\in\mathbb{R}^n}{\arg\min}\left\{\left\|H\mathbf{x} + \hat{\mathbf{b}}^{(k)} - \left(\hat{\mathbf{y}}^{(k)} + \mathbf{y}^{(k)}\right)\right\|_2^2 + \mu\left\|\mathbf{x} - \left(\tilde{\mathbf{x}}^{(k)} + \mathbf{e}^{(k)}\right)\right\|_2^2\right\}, \tag{5.5}$$

$$\hat{\mathbf{y}}^{(k+1)} = \underset{\bar{\mathbf{y}}\in\mathbb{R}^m_{\geq 0}}{\arg\min}\left\{\sum_{i=1}^{m}\left[\bar{y}_i - y_i\ln(\bar{y}_i)\right] + \frac{\eta}{2}\left\|\bar{\mathbf{y}} - \left(H\hat{\mathbf{x}}^{(k+1)} + \hat{\mathbf{b}}^{(k)} - \mathbf{d}^{(k)}\right)\right\|_2^2\right\}, \tag{5.6}$$

$$\tilde{\mathbf{x}}^{(k+1)} = \underset{\mathbf{x}\in\mathbb{R}^n_{\geq 0}}{\arg\min}\left\{\sum_{j=1}^{n}\left|w_j^{(k)}x_j\right| + \frac{\mu}{2}\left\|\mathbf{x} - \left(\hat{\mathbf{x}}^{(k+1)} - \mathbf{e}^{(k)}\right)\right\|_2^2\right\}, \tag{5.7}$$

$$\mathbf{d}^{(k+1)} = \mathbf{d}^{(k)} - \left(H\hat{\mathbf{x}}^{(k+1)} + \hat{\mathbf{b}}^{(k)} - \hat{\mathbf{y}}^{(k+1)}\right), \tag{5.8}$$

$$\mathbf{e}^{(k+1)} = \mathbf{e}^{(k)} - \left(\hat{\mathbf{x}}^{(k+1)} - \tilde{\mathbf{x}}^{(k+1)}\right). \tag{5.9}$$

The algorithm is initialized with $k = 0$, $\hat{\mathbf{y}}^{(0)} = \mathbf{y}$, $\tilde{\mathbf{x}}^{(0)} = \mathbf{e}^{(0)} = 0_{n\times 1}$, and $\mathbf{d}^{(0)} = 0_{m\times 1}$ and terminates when there is no further significant improvement of the solution, or when the maximum number of iterations is reached. The user-specified parameters η and μ control the speed of the convergence of the algorithm and play an important role in balancing the solutions of sub-problems in Equations (5.5)-(5.7). The user-specified parameter β sets the minimum signal to noise ratio of detected molecules. We empirically determined the parameters $\beta = 2.44$, $\eta = 9 \cdot 10^{-3}$, and $\mu = 0.1$. In our experience, when analyzing data with very low signal to noise ratios, it may be useful to set the value of η about ten times smaller to slow down the convergence of the algorithm thereby acquiring more detections.

The algorithm can be simply modified to account for a Gaussian noise model by setting $\hat{\mathbf{y}}^{(k+1)} = \mathbf{y}$ in Equation (5.6) and $\mathbf{d}^{(k+1)} = \mathbf{0}_{m\times 1}$ in Equation (5.8), i.e., by iterating only over Equations (5.5), (5.7), and (5.9). This yields the same update scheme that is used in FALCON (Min et al., 2014b).

5.1.3 Extension to 3D (3denseSTORM)

Each column of the measurement matrix H is created as a shifted copy of a vectorized PSF. This can be extended for 3D imaging by creating the measurement matrix such that it contains Toeplitz blocks of vectorized sections of the 3D PSF at different axial positions. This approach is applicable for any PSF model in general, including measured PSFs. Figure 5.1 shows an example of construction of Toeplitz blocks in the measurement matrix H for 2D and for 3D SMLM imaging methods. In our experiments, the PSF for 2D imaging is created as a rotationally symmetric Gaussian function, while the PSF for 3D astigmatic imaging uses an elliptical Gaussian function with a defocusing curve as described in (Babcock et al., 2012). For 3D biplane imaging there are two PSFs, one for each plane. Both are modeled as rotationally symmetric Gaussian functions, using a defocusing curve described in (Gu et al., 2014).

5.1.4 Theoretical density limits for resolving molecules

The theoretical upper bound for the density of molecules, at which an algorithm based on sparse support recovery can still correctly resolve two molecules, can be derived based on the restricted isometry property (RIP) (Candes and Tao, 2005) of the measurement matrix H. In general, a matrix is said to satisfy the RIP of order k if there exists a constant $0 \leq \delta_k \leq 1$

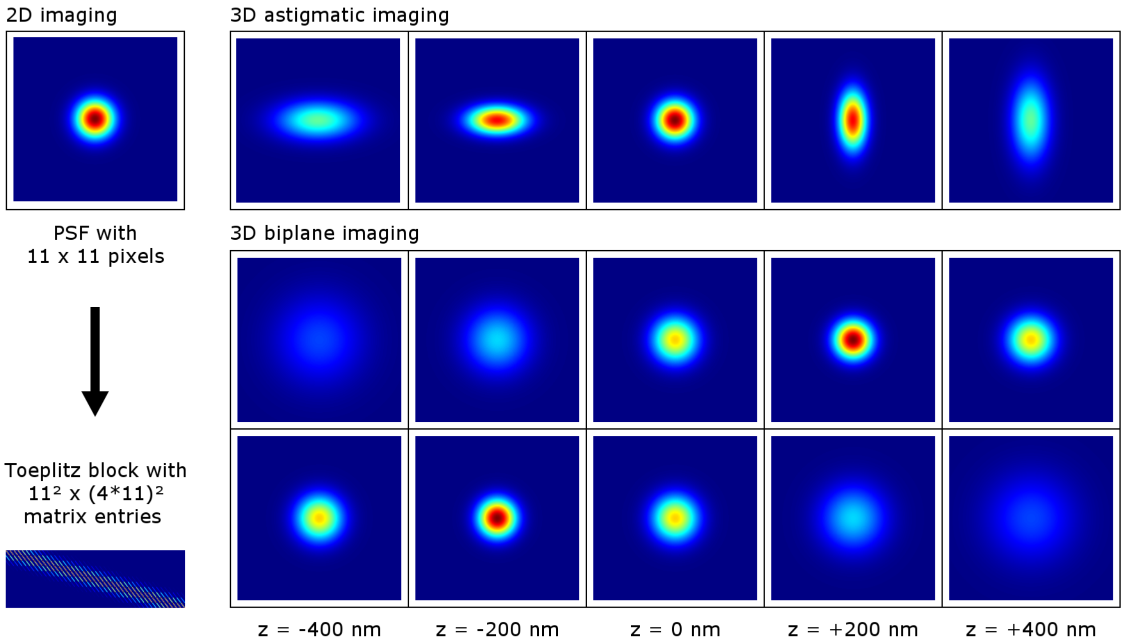

Fig. 5.1 Example of construction of the measurement matrix H for 2D and 3D SMLM imaging methods. The left-hand panel shows vectorization and conversion of a 2D PSF into a Toeplitz block matrix with 4-times image oversampling. The right-hand panels show the PSF in the camera image at different axial positions for 3D methods based on astigmatism and biplane imaging.

such that the inequality

$$(1-\delta_k)\|\mathbf{x}\|_2^2 \leq \|H\mathbf{x}\| \leq (1+\delta_k)\|\mathbf{x}\|_2^2 \tag{5.10}$$

holds for any possible signal $\mathbf{x}$ with at most k non-zero entries. The isometry constant is the smallest number such that the RIP is satisfied. The isometry constant quantifies how far H is from being an orthogonal system and determines the accuracy and stability of the signal recovery from noisy measurements. It has been shown (Candès, 2008) that signals with k non-zero elements can be perfectly recovered with ℓ_1 relaxation if $\delta_{2k} < \sqrt{2}-1$.

In practice, it is nearly impossible to compute the constant δ_k using the RIP concept due to high combinatorial complexity. Instead, mutual coherence of the matrix H can be used as it has been shown (Eldar and Kutyniok, 2012) that if H has unit-norm columns, then H satisfies the RIP of order k with $\delta_k = (k-1)\mu(H)$ for all $k < \mu(H)^{-1}$. The mutual coherence of the matrix H is defined as the largest absolute inner product between any two columns

$$\mu(H) = \max_{1 \leq i \neq j \leq n} \frac{|\mathbf{h}_i^\top \mathbf{h}_j|}{\|\mathbf{h}_i\|^2 \|\mathbf{h}_j\|_2}, \tag{5.11}$$

where $\mathbf{h}_i$ are columns of the matrix H.

2D case

The theoretical limit for resolving two molecules in the 2D case can be derived using the mutual coherence defined in Equation (5.11). Figure 5.2 shows a plot of the mutual coherence as a function of multiples of the full-width at half-maximum (FWHM) of PSF for 2D SMLM imaging. Our results indicate that the closest distance at which two molecules can be resolved using a sparse support recovery algorithm based on norm regularization is approximately $0.78 \cdot \mathrm{FWHM}$. This corresponds to a maximum molecular density of $1.84/\mathrm{FWHM}^2$.

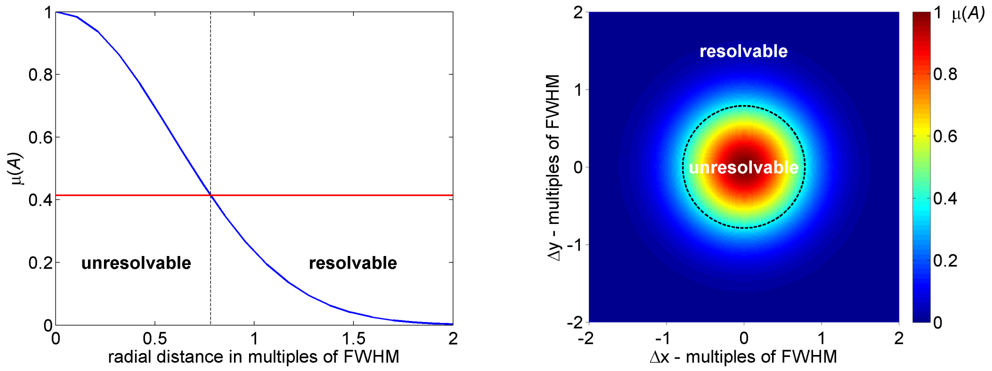

Fig. 5.2 Plot of mutual coherence as a function of multiples of the imaged PSF diameter. Here the PSF is modeled by a rotationally symmetric 2D Gaussian function. Left: radial profile. Right: mutual coherence in 2D space. The threshold value is based on the RIP concept.

3D case

The situation in the 3D case is more complicated, because the mutual coherence of the PSF needs to be calculated for every focal plane with respect to all other focal planes. The results are displayed in Figure 5.3. As expected, the diameter of the imaged PSF is larger when a molecule is further away from the focal plane and the value of the mutual coherence increases. Consequently, the reconstructed lateral resolution for 3D data is expected to be worse than in the 2D case.

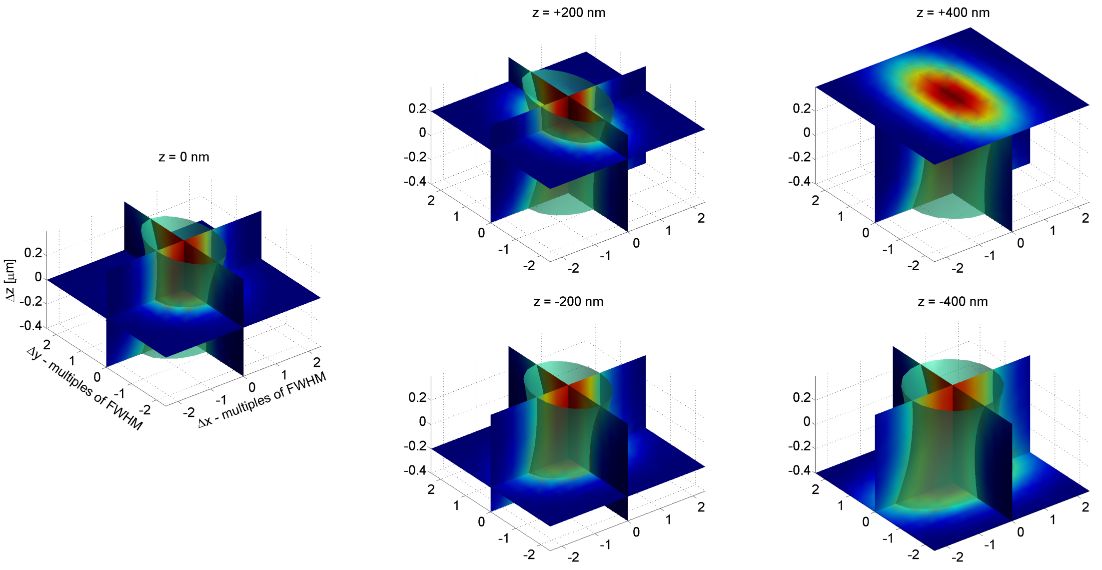

Fig. 5.3 Mutual coherence for astigmatism-based 3D SMLM. Each graph contains a plot of the mutual coherence between the current PSF section (shown as a horizontal plane) and all other sections. The threshold value is displayed as a "tube." and is based on the RIP concept. Resolvable molecules lie outside the tube in blue areas.

5.1.5 Summary of 3denseSTORM algorithm

The flowchart in Figure 5.4 indicates multiple steps to localize molecules performed by 3denseSTORM. First, the support of the input signal is determined using the sparse support recovery scheme in a $3\times$ oversampled grid with a 100 nm step in the axial direction. Because the ℓ_1-regularization term in Equation (5.7) introduces a bias towards zero of the recovered molecular intensities, we perform debiasing with a fixed spatial support (Min et al., 2014b). This ensures good starting conditions for further processing. Next, approximate positions and intensities of molecules are extracted and continuous refinement is performed by maximum-likelihood estimation according to (Babcock et al., 2012; Laurence and Chromy, 2010). Finally, post-processing can be applied, such as removal of outliers, drift correction, etc.

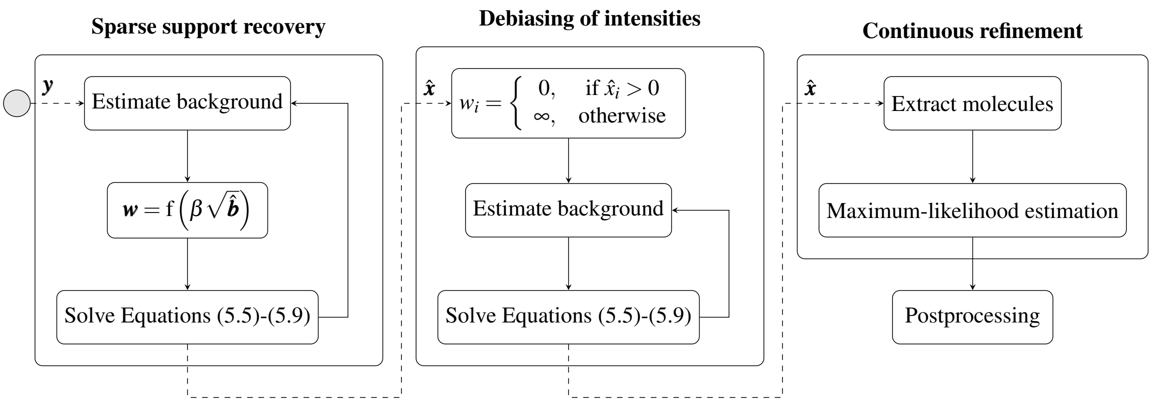

Fig. 5.4 Flowchart of 3denseSTORM algorithm. Both sparse support recovery and debiasing of intensities are iterative processes. Equations Equations (5.5)-(5.9) are each solved in single steps since they all have closed form solutions. The debiasing step is performed with a fixed spatial support ensured by zero/infinity weights. For completeness we define $0 \cdot \infty = 0$.

5.2 Efficient implementation

The way in which the measurement matrix H is formed is important for practical use, because the full representation of the matrix leads to very large memory consumption (H scales quadratically with the size of the input image) and thus time consuming calculations. Algorithms such as CSSTORM (Zhu et al., 2012), L1H (Babcock et al., 2013), or 3D CS analysis (Gu et al., 2014), use this full representation which makes them practically impossible to use for analysis of larger images or for 3D analysis where the size of the measurement matrix grows even faster than in the 2D case. 3denseSTORM benefits from the fact that each of the minimization problems in Equations (5.5)-(5.9) has a closed form solution (Figueiredo and Bioucas-Dias, 2010) and that the calculations involving the measurement matrix can be effectively performed in the frequency domain. Furthermore, the discrete Fourier transform diagonalizes the measurement matrix and thus only the diagonal elements are required for the calculations.

An efficient implementation is essential for the algorithm to have all the properties discussed above. Here we discuss individual steps of the algorithm.

5.2.1 Sparse support recovery

Closed form solutions

Here we derive the closed form solutions of Equations (5.5)-(5.7). Given an arbitrary optimization problem $\hat{\mathbf{x}} = \arg\min_{\mathbf{x}} \{\mathrm{o}(\mathbf{x})\}$, o is the objective function.

Now we find an extreme of the objective function from Equation (5.5):

$$\mathrm{o}(\mathbf{x}) = \left\| H\mathbf{x} + \hat{\mathbf{b}}^{(k)} - \left(\hat{\mathbf{y}}^{(k)} + \mathbf{y}^{(k)}\right) \right\|_2^2 + \mu \left\| \mathbf{x} - \left(\tilde{\mathbf{x}}^{(k)} + \mathbf{e}^{(k)}\right) \right\|_2^2, \tag{5.12}$$

$$\frac{\partial \mathrm{o}(\mathbf{x})}{\partial \mathbf{x}} = 2H^\top \left[H\mathbf{x} + \hat{\mathbf{b}}^{(k)} - \left(\hat{\mathbf{y}}^{(k)} + \mathbf{y}^{(k)}\right) \right] + 2\mu \left[\mathbf{x} - \left(\tilde{\mathbf{x}}^{(k)} + \mathbf{e}^{(k)}\right) \right], \tag{5.13}$$

$$\hat{\mathbf{x}}^{(k+1)} = \left(H^\top H + \mu I\right)^{-1} \left[H^\top \left(\hat{\mathbf{y}}^{(k)} + \mathbf{y}^{(k)} - \hat{\mathbf{b}}^{(k)}\right) + \mu \left(\tilde{\mathbf{x}}^{(k)} - \mathbf{e}^{(k)}\right) \right], \tag{5.14}$$

where I is the identity matrix. Now let's find an extreme of the objective function from Equation (5.6):

$$\mathrm{o}(\bar{\mathbf{y}}) = \sum_{i=1}^{m} \left[\bar{y}_i - y_i \ln(\bar{y}_i)\right] + \frac{\eta}{2} \left\| \bar{\mathbf{y}} - \left(H\hat{\mathbf{x}}^{(k+1)} + \hat{\mathbf{b}}^{(k)} - \mathbf{d}^{(k)}\right) \right\|_2^2, \tag{5.15}$$

$$\frac{\partial \mathrm{o}_i(\bar{\mathbf{y}})}{\partial \bar{y}_i} = \mu \bar{y}_i^2 + \left[1 - \mu \left(H\hat{\mathbf{x}}^{(k+1)} + \hat{\mathbf{b}}^{(k)} - \mathbf{d}^{(k)}\right)_i \right] \bar{y}_i - y_i, \tag{5.16}$$

and given the non-negativity constraint $\bar{\mathbf{y}} \in \mathbb{R}^m_{\geq 0}$ the solution is

$$\hat{y}_i^{(k+1)} = \frac{\mu \left(H\hat{\mathbf{x}}^{(k+1)} + \hat{\mathbf{b}}^{(k)} - \mathbf{d}^{(k)}\right)_i - 1 + \sqrt{\left[1 - \mu \left(H\hat{\mathbf{x}}^{(k+1)} + \hat{\mathbf{b}}^{(k)} - \mathbf{d}^{(k)}\right)_i\right]^2 + 4\mu y_i}}{2\mu} \tag{5.17}$$

Finally, we derive an extreme for the objective function from Equation (5.7):

$$\mathrm{o}(\mathbf{x}) = \sum_{j=1}^{n} \left| w_j^{(k)} x_j \right| + \frac{\mu}{2} \left\| \mathbf{x} - \left(\hat{\mathbf{x}}^{(k+1)} - \mathbf{e}^{(k)} \right) \right\|_2^2 , \tag{5.18}$$

$$\frac{\partial \mathrm{o}(\mathbf{x})}{\partial \mathbf{x}} = \sum_{j=1}^{n} \frac{\partial \left| w_j^{(k)} x_j \right|}{\partial x_j} + \mu \sum_{j=1}^{n} \left[x_j - \left(\tilde{x}_j^{(k+1)} - e_j^{(k)} \right) \right] , \tag{5.19}$$

where

$$\frac{\partial \left| w_j^{(k)} x_j \right|}{\partial x_j} = \begin{cases} \in w_j^{(k)} \operatorname{sgn}(x_j) & , \forall x_j \neq 0 \\ \in \left[-w_j^{(k)}, +w_j^{(k)} \right] & , \forall x_j = 0 \end{cases} , \tag{5.20}$$

thus,

$$x_j \neq 0 : w_j^{(k)} \operatorname{sgn}(x_j) + \mu \left[x_j - \left(\hat{x}_j^{(k+1)} - e_j^{(k)} \right) \right] = 0 , \tag{5.21}$$

and given the constraint $\mathbf{x} \in \mathbb{R}^n_{\geq 0}$ we obtain a result which is known as *soft thresholding*:

$$\tilde{x}_j^{(k+1)} = \max \left\{ \hat{x}_j^{(k+1)} - e_j^{(k)} - \frac{w_j^{(k)}}{\mu}, 0 \right\} . \tag{5.22}$$

Fast arithmetics with the measurement matrix

Let us first show an example of a 3D measurement matrix with three different focal planes

$$H = \begin{pmatrix} H_{z_1} & H_{z_2} & H_{z_3} \end{pmatrix} . \tag{5.23}$$

It is a matrix consisting of several 2D measurement matrices, each for one focal plane z_i, joined horizontally. An example of such matrix is displayed in Figure 5.5. Similarly, images of focal planes of reconstructed signal are joined vertically

$$\mathbf{x} = \begin{pmatrix} \mathbf{x}_{z_1} \\ \mathbf{x}_{z_2} \\ \mathbf{x}_{z_3} \end{pmatrix} . \tag{5.24}$$

Because Equation (5.14) and Equation (5.17) contain multiple operations with the measurement matrix, we recall the following operations and their fast computations which exploit the convolution and the cross-correlation theorems

$$H\mathbf{x} = \sum_i \left\{ S\left[\mathcal{F}^{-1}\left(\mathcal{F}(\mathbf{h}_{z_i}) \cdot \mathcal{F}(\mathbf{x}_{z_i})\right)\right] \right\} , \tag{5.25}$$

$$H_{z_i}^{\top}\mathbf{y} = \mathcal{F}^{-1}\left(\overline{\mathcal{F}(\mathbf{h}_{z_i})} \cdot \mathcal{F}\left(S^{\top}\mathbf{y}\right)\right) , \tag{5.26}$$

where $\mathcal{F}$ is the discrete 2D Fourier transform, operator $\cdot$ performs elementwise multiplication, $\mathbf{h}_{z_i}$ is a convolution kernel from a convolution matrix H_{z_i}, and S is a sampling matrix used for downsampling and upsampling between low-resolution raw images and the high-resolution results of reconstruction. It is important to realize that in STORM experiments only a single plane is actually measured, hence, unlike in a 3D deconvolution problem, there is only a single 2D raw image $\mathbf{y}$.

Solving the matrix inversion from the Equation (5.14) poses another challenge. We start with the product

$$H^{\top}H = \begin{pmatrix} H_{z_{11}} & H_{z_{12}} & H_{z_{13}} \\ H_{z_{21}} & H_{z_{22}} & H_{z_{23}} \\ H_{z_{31}} & H_{z_{32}} & H_{z_{33}} \end{pmatrix} . \tag{5.27}$$

The result is a symmetric matrix which follows from the theorem saying that two matrices which are simultaneously diagonalizable are always commutative, e.g., $H_{z_1}H_{z_3} = FD_{H_{z_1}}F^{-1}FD_{H_{z_3}}F^{-1} = FD_{H_{z_1}}D_{H_{z_3}}F^{-1} = FD_{H_{z_3}}D_{H_{z_1}}F^{-1} = H_{z_3}H_{z_1}$, where F is a discrete Fourier matrix, which diagonalizes a convolution matrix. The symmetry is evident from Figure 5.5.

For sake of simplicity, we make substitution $G = H^\top H + \mu I$. To solve Equation (5.14), we need to find inverse of G. As mentioned above this is very different from a standard 3D deconvolution problem as the raw data $\mathbf{y}$ originate from only a single plane. Consequently, the matrix G carries more information than a standard 3D deconvolution matrix, see Figure 5.5 for example.

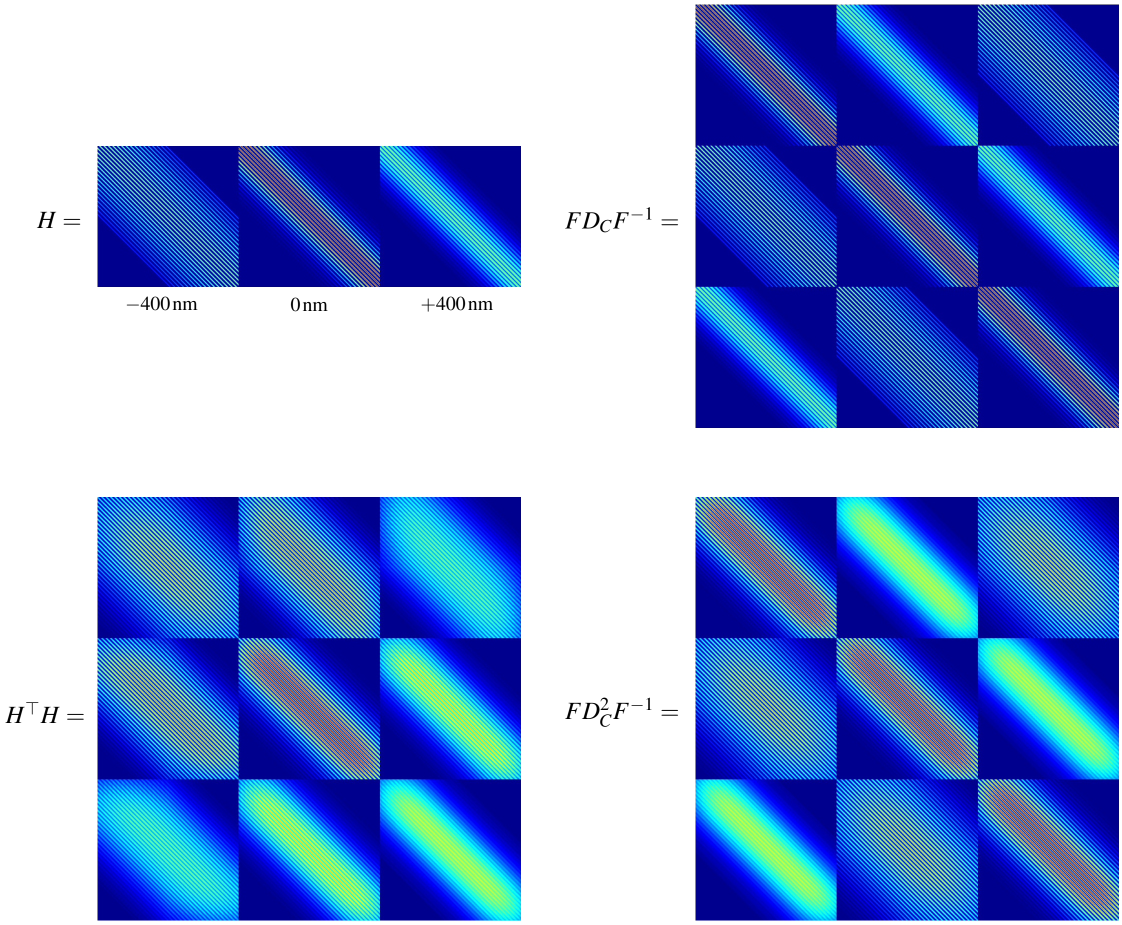

Fig. 5.5 Example of a 3D measurement matrix H with PSF sections $z = [-400, 0, +400]$ nm and 3D convolution matrix C. F is the Fourier matrix and D_C is diagonalized convolution matrix. Given $n = 3$ sections of PSF, both $H^\top H$ and $FD_C^2F^{-1}$ matrices contain $n \times n$ blocks. The squared 3D measurement matrix contains $n(n+1)/2$ distinct blocks, while the squared 3D convolution matrix contains just n distinct block.

A popular approach to solve inverse of a block matrix is to utilize LDU decomposition $G^{-1} = (LDU)^{-1} = U^{-1}D^{-1}L^{-1}$, thus exploiting the fact that it is fairly simple to invert triangular (L, U) and diagonal (D) matrices respectively. L^{-1}, U^{-1} are computed by forward and backward elimination algorithms respectively, while D^{-1} is a direct inverse of blocks on diagonal of D.

Usually LDU decomposition of a large matrix is done by recursively dividing the matrix into 2-by-2 blocks until size of the block is 1 and solving the LDU decomposition on the 4 submatrices by computing block inverse by utilizing the Schur complement. However, in our case this approach is not helpful at all, because we already work with a diagonalized block submatrices and the division algorithm would ruin this favorable property. Thus we derived the following recursive formula which exploits the structure of G:

$$\begin{aligned} M_{rc}^{(n+1)} &= G_{rc} \\ M_{rc}^{(s)} &= M_{rc}^{(s+1)} - M_{rs} M_{ss}^{-1} M_{sc} \end{aligned} \tag{5.28}$$

where $\{r, c \in \mathbb{Z} \mid 1 \leq r, c \leq n\}$ are row and column indices and $\{s \in \mathbb{Z} \mid \min(k+1, n) \leq s \leq n\}$, where $k = \max(r, c)$. Then by simple decomposition of the matrix M we obtain the matrices L, D, and U:

$$L_{rc} = \begin{cases} I & \text{for } r = c \\ M_{rc} M_{kk}^{-1} & \text{for } r > c \\ 0 & \text{for } r < c \end{cases}, \quad D_{rc} = \begin{cases} M_{rc} & \text{for } r = c \\ 0 & \text{for } r > c \\ 0 & \text{for } r < c \end{cases}, \quad U_{rc} = \begin{cases} I & \text{for } r = c \\ 0 & \text{for } r > c \\ \mathrm{M_{rc} M_{kk}^{-1}} & \text{for } r < c \end{cases}, \tag{5.29}$$

where I is an identity matrix and 0 is a zero matrix of appropriate size. When the respective matrices are computed and G^{-1} is known, Equation (5.14) is solved by a simple blockwise matrix multiplication.

Summary of sparse support recovery

Thanks to the formulae we derived in this section, computation of sparse support recovery problem is time and memory efficient. The optimization problems in Equations (5.5)-(5.7) all have closed form solutions. In addition, all the matrix operations written above can be calculated in the Fourier domain by applying convolution and cross-correlation theorems. This effectively means we do not need the full measurement matrix, but instead we just work with the convolution kernels corresponding to PSF sections from individual focal planes, thus the memory consumption is reduced significantly, which allows for processing of larger images with finer sampling.

5.2.2 Debiasing of intensities

As pointed out in (Min et al., 2014b), the ℓ_1-regularizer in the deconvolution Equation (5.7) introduces a bias of intensities towards zero. To obtain the best possible initial estimate of parameters prior to the refinement, an intermediate step is introduced to debias the intensities. The main idea from (Min et al., 2014b) is to fix the non-zero support $\mathcal{S}$ of the signal coming out of the deconvolution and run the deconvolution without the ℓ_1 term, but only on the support $\mathcal{S}$. This is achieved by replacing Equation (5.22) by

$$\tilde{x}_j^{(k+1)} = \begin{cases} \hat{x}_j^{(k+1)} - e_j^{(k)} & \text{for } i \in \mathcal{S}, \\ 0 & \text{otherwise.} \end{cases} \tag{5.30}$$

5.2.3 Continuous refinement

The input data for continuous refinement is a hi-resolution deconvoled 3D stack of clusters of bright pixels on a black background. Each cluster is considered a single molecule. As the first step, the average position and total intensity of each cluster is estimated. The position is estimated as the center of gravity in a region centered around the brightest pixel of the cluster. The total intensity of each cluster is the sum of the pixel intensities in the cluster. From this point forward, we work with molecular parameters $\theta = \{\theta_x, \theta_y, \theta_z, \theta_N, \theta_o\}$ just like in any other STORM experiment, thus the previous steps can be viewed as the detection step of a standard STORM analyzer. The refinement takes this set of preestimated parameters and performs a maximum likelihood estimation (MLE) on the raw images. The estimator is based on the Levenberg-Marquardt algorithm as adapted for MLE as described in (Laurence and Chromy, 2010).

Given a raw image in photon counts $I(x,y)$ at positions (x,y), parametrized PSF model $\mathrm{h}(x,y \mid \theta)$, and a fitting region $\mathscr{D}$, the Poisson likelihood function is

$$\mathcal{L}(\theta \mid \mathscr{D}) = \prod_{(x,y)\in\mathscr{D}} \frac{\mathrm{h}(x,y \mid \theta)^{I(x,y)} \exp\left(-\mathrm{h}(x,y \mid \theta)\right)}{I(x,y)!}. \tag{5.31}$$

Since the maximum value of the likelihood function is $\mathcal{L}(\mathscr{D}|\mathscr{D})$, in (Laurence and Chromy, 2010) authors proposed to divide the likelihood function by its maximum value to yield the following error function to be minimized:

$$\chi^2_{\mathrm{MLE}}(\theta) = -2\ln\left(\frac{\mathcal{L}(\theta \mid \mathscr{D})}{\mathcal{L}(\mathscr{D}|\mathscr{D})}\right), \tag{5.32}$$

$$\chi^2_{\mathrm{MLE}}(\theta) = 2 \sum_{\substack{(x,y)\,\in\,\mathscr{D},\\ I(x,y)\,>\,0,\\ \mathrm{h}(x,y\,\mid\,\theta)\,>\,0}} \mathrm{h}(x,y \mid \theta) - I(x,y) - I(x,y)\ln\left(\frac{\mathrm{h}(x,y \mid \theta)}{I(x,y)}\right). \tag{5.33}$$

Then the elements of gradient $\nabla_\theta \chi^2_{\mathrm{MLE}}(\theta)$ are calculated as

$$\left(\nabla_\theta \chi^2_{\mathrm{MLE}}(\theta)\right)_i = \frac{\partial \chi^2_{\mathrm{MLE}}(\theta)}{\partial \theta_i} = 2 \sum_{(x,y)\in\mathscr{D}} \left(1 - \frac{I(x,y)}{\mathrm{h}(x,y \mid \theta)}\right) \frac{\partial \mathrm{h}(x,y \mid \theta)}{\partial \theta_i} \tag{5.34}$$

and elements of Hessian $\nabla^2_\theta \chi^2_{\mathrm{MLE}}(\theta)$ are

$$\left(\nabla^2_\theta \chi^2_{\mathrm{MLE}}(\theta)\right)_{i,j} = \frac{\partial^2 \chi^2_{\mathrm{MLE}}(\theta)}{\partial \theta_i \partial \theta_j} = 2 \sum_{(x,y)\in\mathscr{D}} \left[\frac{\partial \mathrm{h}(x,y|\theta)}{\partial \theta_i} \frac{\partial \mathrm{h}(x,y|\theta)}{\partial \theta_j} \frac{I(x,y)}{\mathrm{h}(x,y|\theta)} + \left(1 - \frac{I(x,y)}{\mathrm{h}(x,y|\theta)}\right) \frac{\partial^2 \mathrm{h}(x,y|\theta)}{\partial \theta_i \partial \theta_j}\right]. \tag{5.35}$$

Following the Gauss-Newton optimization scheme we can write

$$\nabla^2_\theta \chi^2_{\mathrm{MLE}}\left(\theta^{(k)}\right)\left(\theta^{(\min)} - \theta^{(k)}\right) = -\nabla_\theta \chi^2_{\mathrm{MLE}}\left(\theta^{(k)}\right), \tag{5.36}$$

where $\theta^{(k)}$ is value of θ in k-th iteration of the Gauss-Newton algorithm and $\theta^{(\min)}$ is the best solution set found so far which minimizes χ^2_{MLE}. By a simple substitution we get the following elementwise formula for the update vector $\Delta\theta$:

$$\alpha_{ij}\Delta\theta_j = \beta_i\,. \tag{5.37}$$

In (Press, 2007) it was proposed to ignore the second derivatives in the Hessian due to their destabilizing influence, thus the above substitution is

$$\alpha_{ij} = \sum_{(x,y)\in\mathscr{D}} \frac{\partial \mathrm{h}(x,y|\theta)}{\partial\theta_i}\frac{\partial \mathrm{h}(x,y|\theta)}{\partial\theta_j}\frac{I(x,y)}{\mathrm{h}(x,y|\theta)^2},\ \beta_i = -\sum_{(x,y)\in\mathscr{D}}\left(1-\frac{I(x,y)}{\mathrm{h}(x,y|\theta)}\right)\frac{\partial \mathrm{h}(x,y|\theta)}{\partial\theta_i}\,. \tag{5.38}$$

Finally, transforming the Gauss-Newton optimization scheme to the Levenberg-Marquardt algorithm by addition of a diagonal factor λ

$$\begin{aligned} \alpha'_{ij} &= \alpha_{ij}\left(1+\lambda\delta_{ij}\right), \\ \delta_{ij} &= \begin{cases} 1 & \text{for}\, i=j \\ 0 & \text{otherwise} \end{cases} \end{aligned} \tag{5.39}$$

changes Equation (5.37) to

$$\alpha'_{ij}\Delta\theta_j = \beta_i\,. \tag{5.40}$$

In (Babcock et al., 2012) authors proposed an update step with a clamp c, which we adopted here to provide better stability of the results. The parameter vector is updated as

$$\theta^{(k+1)} = \theta^{(k)} + \left[\Delta\theta/\left(1+|\Delta\theta|/c\right)\right]. \tag{5.41}$$

If the update step fails to decrease value of the χ^2_{MLE}, the factor is adjusted $\lambda = 10\lambda$.

Flow of continuous refinement

All the molecules from the detection step are extracted into an active set. A single iteration of the refinement algorithm is applied on each molecule from the set individually. When the update step did not provide a significant improvement, i.e.,

$$|\chi^2_{\mathrm{MLE}}(\theta^{(k)}) - \chi^2_{\mathrm{MLE}}(\theta^{(k-1)})|/\chi^2_{\mathrm{MLE}}(\theta^{(k)}) < \chi^2_{\mathrm{threshold}}, \tag{5.42}$$

the particular molecule is removed from the active set. The refinement algorithm is then executed until the active set of molecules is empty or until the maximum number of iterations is reached.

5.2.4 PSF model

The choice of a PSF model is essential for good results. In our experimental part, we used an analytic model of a two-dimensional elliptic Gaussian function. However, in real experiments with 3D imaging based on astigmatism we found that this simplification is very rough and yields results of lower quality than expected due to aberrations caused by the cylindrical lens. This could be improved by using a better corrected lens or by using an adaptive optics setup. Nonetheless, there is also an option to use a real PSF instead. By measuring a 3D stack of bright fluorescent beads, we can extract an experimentally measured PSF. The PSF estimation can be performed by a simple stack averaging, a deconvolution based method like the one used in the Huygens software, etc. Fine sampling and high signal to noise ratio are key here.

The 3denseSTORM algorithm can accept such a measured PSF model. Recall that we use the Fourier domain extensively for the majority of computations, thus if a DC offset is present in the PSF stack, we apply an apodization window (e.g., Tukey) of each plane of the stack. Then the PSF is approximated by 3D cubic B-splines. From the resulting approximate model, we build up the measurement matrices for deconvolution and debiasing (but not in their full form as described in Section 5.2.1). For continuous refinement, we precompute first and second partial derivatives, which are later utilized for evaluating the PSF function and the Jacobian matrix used in the Levenberg-Marquardt algorithm.

In the refinement we work with positional parameters $(\theta_x, \theta_y, \theta_z)$, however, when working with measured PSFs we have to distinguish between discrete positions in the sampling grid

ω and real valued offsets ε. This is written as $\theta_x = \omega_x + \varepsilon_x, \theta_y = \omega_y + \varepsilon_y, \theta_z = \omega_z + \varepsilon_z$. Thus, we need to define a new discrete parameters $\omega = (\omega_x, \omega_y, \omega_z)$, which is used for indexing in the measured PSF function $\rho(x, y \mid \omega)$ and its derivatives. Putting this all together, the Jacobian is evaluated using a first-order three-dimensional Taylor expansion as follows

$$\begin{aligned}
\frac{\partial \mathrm{h}(x,y|\theta)}{\partial \theta_x} &= \theta_N \left(\frac{\partial \rho(x,y|\omega)}{\partial \omega_x} + \varepsilon_x \frac{\partial^2 \rho(x,y|\omega)}{\partial \omega_x^2} + \varepsilon_y \frac{\partial^2 \rho(x,y|\omega)}{\partial \omega_x \partial \omega_y} + \varepsilon_z \frac{\partial^2 \rho(x,y|\omega)}{\partial \omega_x \partial \omega_z} \right) , \\
\frac{\partial \mathrm{h}(x,y|\theta)}{\partial \theta_y} &= \theta_N \left(\frac{\partial \rho(x,y|\omega)}{\partial \omega_y} + \varepsilon_x \frac{\partial^2 \rho(x,y|\omega)}{\partial \omega_y \partial \omega_x} + \varepsilon_y \frac{\partial^2 \rho(x,y|\omega)}{\partial \omega_y^2} + \varepsilon_z \frac{\partial^2 \rho(x,y|\omega)}{\partial \omega_y \partial \omega_z} \right) , \\
\frac{\partial \mathrm{h}(x,y|\theta)}{\partial \theta_z} &= \theta_N \left(\frac{\partial \rho(x,y|\omega)}{\partial \omega_z} + \varepsilon_x \frac{\partial^2 \rho(x,y|\omega)}{\partial \omega_z \partial \omega_x} + \varepsilon_y \frac{\partial^2 \rho(x,y|\omega)}{\partial \omega_z \partial \omega_y} + \varepsilon_z \frac{\partial^2 \rho(x,y|\omega)}{\partial \omega_z^2} \right) , \\
\frac{\partial \mathrm{h}(x,y|\theta)}{\partial \theta_N} &= \rho(x, y \mid \omega) + \varepsilon_x \frac{\partial \rho(x,y|\omega)}{\partial \omega_x} + \varepsilon_y \frac{\partial \rho(x,y|\omega)}{\partial \omega_y} + \varepsilon_z \frac{\partial \rho(x,y|\omega)}{\partial \omega_z} , \\
\frac{\partial \mathrm{h}(x,y|\theta)}{\partial \theta_o} &= 1 .
\end{aligned} \tag{5.43}$$

Although we could use the B-splines directly for the evaluation, it makes the computation much slower with just a small improvement in precision. Since we need second partial derivatives in the Jacobian anyway, we take advantage of the already calculated derivatives to approximate the PSF function by a second-order three-dimensional Taylor expansion

$$\begin{aligned}
\mathrm{h}(x, y \mid \theta) = \theta_o + \theta_N \ \rho(x, y \mid \omega) & \\
+ \theta_N & \left(\varepsilon_x \frac{\partial \rho(x, y \mid \omega)}{\partial \omega_x} + \varepsilon_y \frac{\partial \rho(x, y \mid \omega)}{\partial \omega_y} + \varepsilon_z \frac{\partial \rho(x, y \mid \omega)}{\partial \omega_z} \right) \\
+ \theta_N & \left(\frac{\varepsilon_x^2}{2} \frac{\partial^2 \rho(x, y \mid \omega)}{\partial \omega_x^2} + \frac{\varepsilon_y^2}{2} \frac{\partial^2 \rho(x, y \mid \omega)}{\partial \omega_y^2} + \frac{\varepsilon_z^2}{2} \frac{\partial^2 \rho(x, y \mid \omega)}{\partial \omega_z^2} \right) \\
+ \theta_N & \left(\varepsilon_x \varepsilon_y \frac{\partial^2 \rho(x, y \mid \omega)}{\partial \omega_x \partial \omega_y} + \varepsilon_x \varepsilon_z \frac{\partial^2 \rho(x, y \mid \omega)}{\partial \omega_x \partial \omega_z} + \varepsilon_y \varepsilon_z \frac{\partial^2 \rho(x, y \mid \omega)}{\partial \omega_y \partial \omega_z} \right) .
\end{aligned} \tag{5.44}$$

5.3 Experimental evaluation

We designed a set of experiments to validate the algorithm and the implementation with both simulated and real data.

5.3.1 Analysis of simulated 3D SMLM data

Quantitative performance evaluation

We designed Monte-Carlo simulations to quantitatively evaluate the performance of 3denseSTORM in terms of the localization accuracy (lateral and axial), detection rate (F1-score), and recovered molecular density. We generated a series of experiments in which the density of the molecules varied from 0.1 to 20 molecules/m^2 with a step of 0.5 molecules/m^2 between each experiment (i.e., 41 independent simulations). The dataset in each experiment contained 100 images 32×32 pixels in size. The pixel size was set to 80 nm and the FWHM of in focus molecules was 260 nm. All molecules were placed randomly inside a central region of 20×20 pixels within an axial range of -400 nm to +400 nm. Each molecule was generated with an integral intensity of 2500 photons. Background offset of 70 photons was added to each image and each such image was additionally corrupted with Poisson noise. Data for astigmatic imaging were generated using ThunderSTORM, see Section 3.7.

The results were compared to standard single-molecule fitting performed by ThunderSTORM with the default settings and to 3D DAOSTORM (Babcock et al., 2012). All three methods use astigmatic imaging and refinement of localized molecules based on maximum-likelihood estimation. The main difference between these algorithms is the detection method for finding the imaged molecules. The performance of 3denseSTORM was also evaluated for biplane imaging. To demonstrate the importance of accounting for a Poisson noise model, we also show the results for 3denseSTORM with a Gaussian noise model as described in Section 5.1.2.

Detection of a molecule is counted as a true-positive if it is located within 200 nm lateral radius from its ground truth position. The F1-score was calculated according to (Křížek et al., 2011) and the recovered density as the number of true positive detections per μm^2. The localization accuracy was determined as the root mean square of displacements between true positive detections and their ground truth positions.

Our results indicate that single-molecule fitting is not able to recover densities higher than about 3.5 molecules/μm^2, while 3D DAOSTORM saturates at about 7.5 molecules/μm^2.

3denseSTORM can recover densities up to about 13.5 $\text{molecules}/\mu\text{m}^2$ for astigmatic imaging and up to about 15 $\text{molecules}/\mu\text{m}^2$ for biplane imaging and thus provides the best detection rate compared to other tested methods, see Figure 5.6. The Gaussian version of 3denseSTORM performed slightly worse than the Poisson version. The theoretical limit of 18.6 $\text{molecules}/\mu\text{m}^2$ was estimated as described in Section 5.1.4. It is important to recall that the density limit is directly related to the FWHM of PSF.

All of the evaluated algorithms achieved similar localization accuracy in the lateral direction, but single-molecule fitting consistently had the worst performance, and 3denseSTORM with biplane imaging had the best. In the axial direction, the results for single-molecule fitting are noticeably worse than for the other tested algorithms. 3denseSTORM with biplane imaging achieves a better detection rate and better localization accuracy than the astigmatic approach, which is in agreement with theoretical analysis based on Fisher information theory (Badieirostami et al., 2010).

Visual examination

For visual examination of the localization accuracy of the detected molecules, we generated a second simulated 3D SMLM dataset with molecules randomly distributed in the shape of a trefoil knot. As in the other simulations, the data consisted of 100 images of size 32×32 pixels. Each image contained 30 molecules, where every molecule was modeled with an integral intensity of 2500 photons. Background offset of 70 photons was added to each image and each generated image was corrupted with Poisson noise. The axial position of the set of molecules was modulated by the generating function of a trefoil knot (a sine function) ranging from -400 nm to +400 nm.

As expected, the low detection rate of single-molecule fitting methods makes the shape of the reconstructed knot incomplete. This is especially noticeable near the intersections, see Figure 5.7. Moreover, the recovered axial positions of many of the molecules in these areas are not correct. 3D DAOSTORM achieves much higher detection rates and the localization accuracy in the axial direction is better. 3denseSTORM provides the highest detection rate and the localized molecules preserve the shape and continuity of the 3D shape. Also the

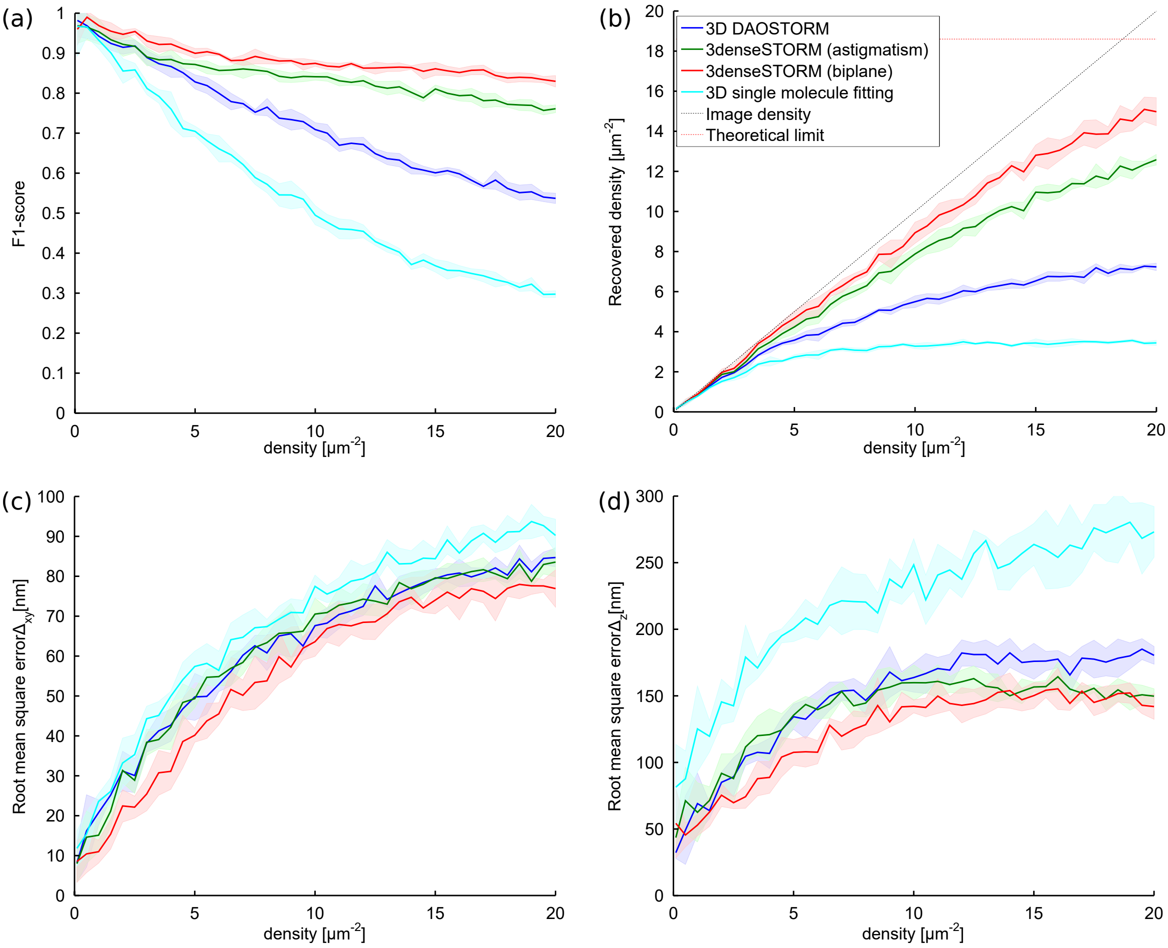

Fig. 5.6 Evaluation of high density 3D Monte-Carlo simulations. (a) F1-score, (b) recovered density calculated as the number of true-positive detections per μm^2, (c) lateral localization error, (d) axial localization error. The shaded areas correspond to the standard deviation of five repeated measurements.

color-coded axial position of the molecules is in good agreement with the ground-truth visualization of the simulation.

However, there is one key difference between results obtained by astigmatic and biplane imaging methods, see the intersections of the knot in areas indicated by arrows in Figure 5.7. Here all algorithms for astigmatic imaging fail to localize molecules correctly in the lower intersection of the knot while biplane imaging gives almost perfect results. We attribute this behavior to a coincidence of the sample structure with orientation of elliptical projections of the imaged PSF in the case of astigmatic imaging. This effect is most significant when vertically oriented ellipses lie along a horizontal structure and horizontally oriented ellipses lie along a vertical structure. This situation leads to large areas of high intensity in the raw data and the localization algorithm fails to assign the correct position to the detected molecules. Biplane imaging is less prone to this kind of problem because the PSF in each imaging plane is rotationally symmetric, making biplane imaging methods more robust in estimating the axial position. To quantify the results, we again measured the detection rate and localization error for each method, see Table 5.1.

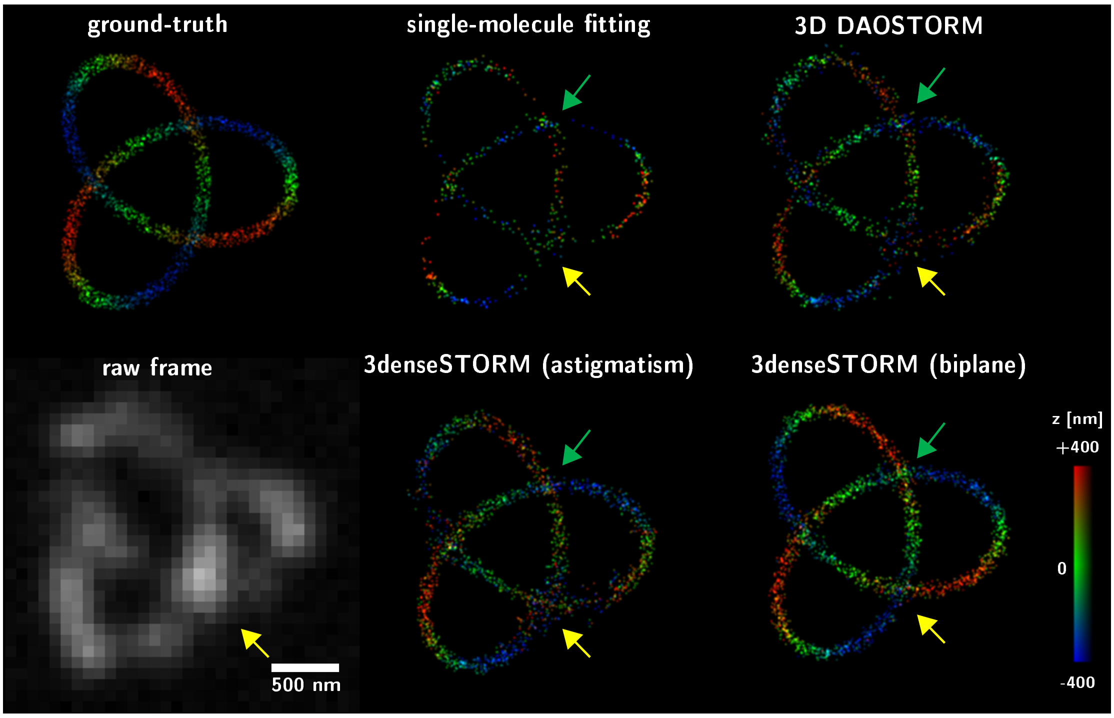

Fig. 5.7 Trefoil knot generated from 100 frames, each containing 30 molecules. The top panel shows the ground-truth data and the results for single-molecule fitting (astigmatism) and 3D-DAOSTORM (astigmatism). The bottom panel shows an example of one raw data frame and results for 3denseSTORM (astigmatic and biplane imaging).

5.3.2 Real data analysis

Cellular samples

U2-OS cells were maintained in DMEM supplemented with 10% FCS, 100 U/ml penicillin, and 100 U/ml streptomycin (all from Invitrogen, Carlsbad, CA, USA) at 37°C, 5% CO_2, and 100% humidity. Mowiol containing 1,4-diazabicyclo[2.2.2]octane (DABCO) was from

Results from Figure 5.7	Number of molecules	F1-score	Loc. accuracy (lateral, nm)	Loc. accuracy (axial, nm)
Ground truth	3000	-	-	-
Single mol. fitting (astig.)	852	0.44	70	226
3D DAOSTORM (astig.)	1498	0.67	60	153
3denseSTORM (astig.)	2000	0.79	62	136
3denseSTORM (biplane)	2295	0.83	57	88

Table 5.1 Results of the 3D simulation with trefoil knot.

Fluka (St. Louis, Missouri). Cells were grown on high precision #1.5 coverslips (Zeiss, Jena, Germany). Before imaging, cells were first washed with PBS, then fixed with methanol for 5 minutes at $-20°$C. For imaging of tubulin, we labeled the cells with mouse anti tubulin monoclonal antibody (T5168, Sigma, St. Louis, Missouri) for 30 minutes at room temperature. We then labeled the primary antibodies for 30 minutes at room temperature with Alexa 532-labeled goat anti mouse secondary antibody (A11002, Invitrogen). After washing with PBS, we finally mounted the coverslips in mowiol containing 100 mM mercaptoethylamine (Sigma) and sealed them onto clean slides with clear nail polish. 100 nm tetraspeck beads for measuring the microscope's PSF and establishing the calibration for 3D imaging were from Invitrogen.

Microscopy

We used an Olympus IX70 microscope equipped with an Olympus planapochromatic 100× / 1.40 NA oil immersion objective and a NEO sCMOS camera (Andor, Belfast, Northern Ireland). The back-projected CCD pixel size in the sample was 65 nm. A 405 nm, 10 mW diode laser and a 532 nm, 1000 mW DPSS laser (Dragon laser, ChangChun, China) were filtered using bandpass filters and combined with dichroic mirrors (Chroma, Bellows Falls, VT, USA), diffused with a laser speckle reducer (Optotune, Dietikon, Switzerland), then coupled into a 0.39 NA, 600 μm diameter multimode optical fiber (M29L01, Thor Labs, Newton, New Jersey). The fiber output was imaged into the sample using a critical illumination setup. This configuration resulted in an evenly illuminated field. We closed the microscope's field stop so that only a small area of the sample ($\approx 30\ \ \mu$m diameter) was illuminated by the full laser power. We isolated Alexa 532 fluorescence using a TIRF filter set (Chroma). For 3D imaging, we introduced a 500 mm focal length cylindrical lens in front of the sCMOS camera (LJ1144RM-A, Thor Labs). Image sequences were acquired using Andor IQ software. We typically recorded 400 frames with an exposure time of 100 ms. For the sake of simplicity we did not apply any additional corrections for pixel-dependent parameters of the sCMOS camera in any of the evaluated algorithms.

5.3.3 Results

To evaluate the quality of 2D image reconstruction with 3denseSTORM, we used a publicly available dataset from the single molecule localization challenge website[1]. The dataset, "Tubulins-high density," contributed by Nicolas Olivier, Debora Keller and Suliana Manley, consists of 500 images of 128×128 pixels. We compared 3denseSTORM with 3D DAOSTORM and with single molecule fitting performed by ThunderSTORM. We used ThunderSTORM with the default settings. 3D DAOSTORM was run in a 2D mode with the threshold set for high signal-to-noise (SNR) data. The results in Figure 5.8 show that both 3D DAOSTORM and 3denseSTORM reconstruct the data well, even after only 100 frames. Single molecule fitting performed by ThunderSTORM suffers from low detection rates. The reconstructed images produced by 3denseSTORM look sharper in high density areas compared to other processing methods, see the region indicated by the yellow square in Figure 5.8.

To further evaluate 3denseSTORM for 3D data reconstruction, we acquired a series of images of immuno-labeled microtubules in U2-OS cells using astigmatic imaging. We analyzed two datasets labeled as ROI 1 (70×70 pixels) and ROI 2 (47×58 pixels), each 400 frames long. We used an exposure time of 100 ms, so each dataset was acquired in ≈ 40 seconds. Both datasets suffer from very low SNR due to high background caused mainly by out of focus fluorescence. We adjusted the threshold in 3D DAOSTORM for

---

[1] *SMLM Challenge 2013* available at http://bigwww.epfl.ch/smlm/challenge2013/

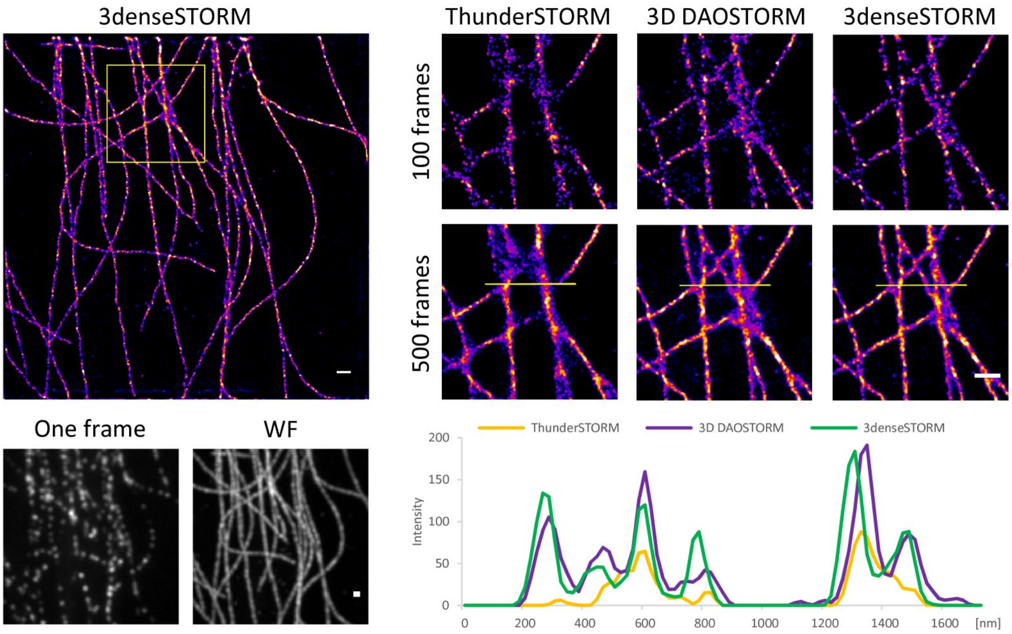

Fig. 5.8 Comparison of 3denseSTORM, 3D DAOSTORM and ThunderSTORM on real 2D high-density data. The widefield (WF) image was generated as the standard deviation of the entire sequence of 500 frames. The right panel shows a detail of an area marked by the yellow square in the left image. Intensity profiles were measured and plotted from the reconstructions of 500 frames. All scalebars are 500 nm.

low SNR data according to recommendations in the software documentation. The results displayed in Figure 5.9 show 2D intensity projections to compare how the methods reconstruct sample features. In ROI 1 the arrows indicate areas of high molecular density where 3denseSTORM clearly outperforms the other two algorithms. In ROI 2 the line segments indicate where the intensity profiles were plotted. 3denseSTORM successfully resolved two parallel microtubules while the other methods did not. We also visualized the result of 3denseSTORM as a 3D image with color-coded z-coordinates in Figure 5.9.

To provide insight into computational complexity of 3denseSTORM, we measured execution times of all three tested algorithms while processing the real datasets from Figures 5.8 and 5.9. The comparison was performed on a standard PC with Intel Core i5-3570 CPU and with NVIDIA GeForce GTX 670 GPU. The GPU was used to accelerate computation of the fast Fourier transforms used in 3denseSTORM. Data processing was performed in 4 parallel threads (one per each core of the CPU). The results are summarized in Table 5.2.

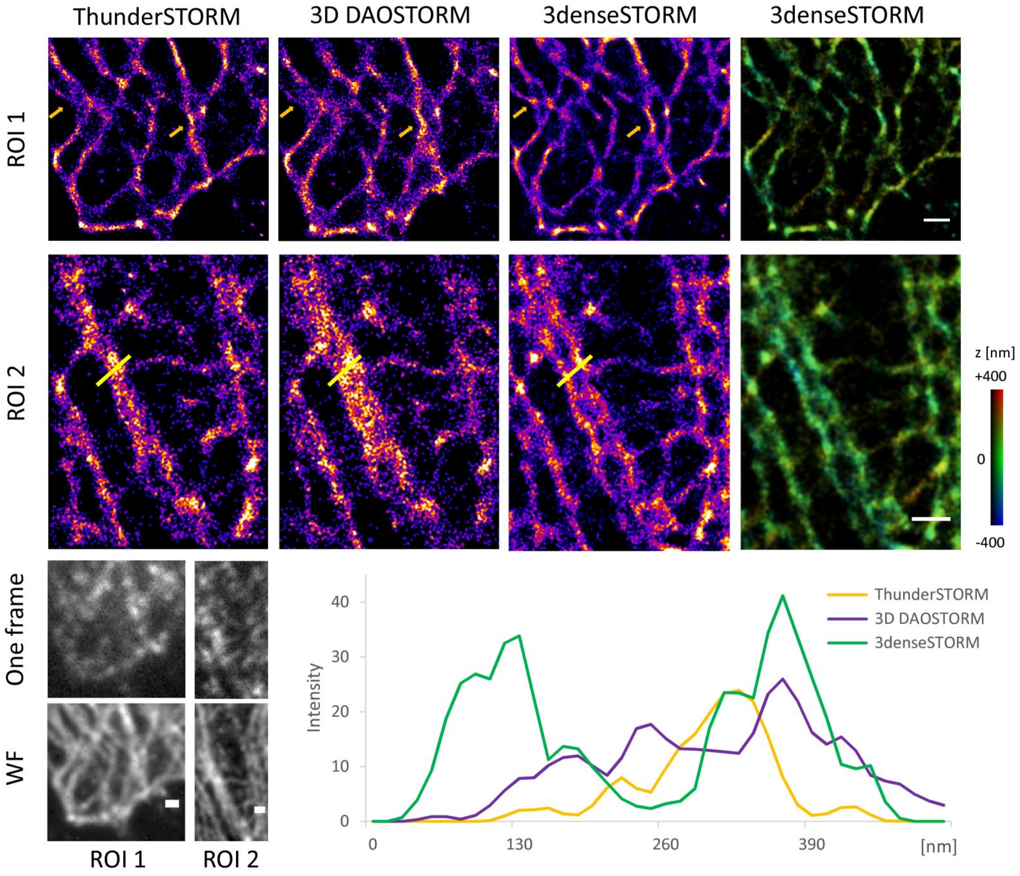

Fig. 5.9 Comparison of 3denseSTORM, 3D DAOSTORM and ThunderSTORM on real 3D high-density data (U2-OS cells immuno-labeled for tubulin). The widefield (WF) images for each ROI were generated as the standard deviation of the entire sequence of 400 frames. For visual examination, a 2D image for each method was reconstructed. The yellow arrows in ROI 1 mark high density areas. The rightmost column shows a 3D visualization with color-coded z-coordinates. Intensity profiles were measured in reconstructions in ROI 2 and plotted to compare the methods. All scale bars are 500 nm.

5.3.4 Limits of dense data analysis

Here we briefly discuss issues encountered when analyzing data with high molecular density.

Analysis of data with density higher than the theoretical limit

To further test behavior and limits of the algorithm we analyzed 2D data with uniform distribution of photoactivated fluorophores whose density reached over the theoretical maximum discussed in Section 5.1.4.

Data set (width × height × frames)	2D Tubulins (128 × 128 × 500)	3D Tubulins (ROI 1) (70 × 70 × 400)	3D Tubulins (ROI 2) (47 × 58 × 400)
ThunderSTORM	6.9 sec	1.8 sec	1.6 sec
3D DAOSTORM	5 min 7 sec	1 min 35 sec	1 min 29 sec
3denseSTORM	87 min 59 sec	25 min 26 sec	23 min 4 sec

Table 5.2 Execution times of examined algorithms on Data sets from Figures 5.8 and 5.9

In such cases the distribution of recovered molecules form an artificial honeycomb-like structure, which is not present in the input data. See Figure 5.10 for an example.

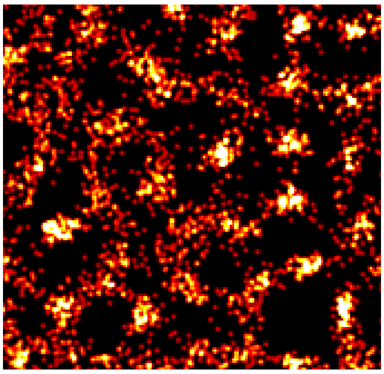

Fig. 5.10 Result of analysis of 2D data with molecular density too high for a correct recovery.

Comparison of 3D imaging methods for high-density SMLM

When we analyzed the trefoil knot in the previous section we encountered an interesting phenomenon upon which we want to expand here. We hypothesize astigmatism isn't well suited for imaging with medium to high molecular densities, because the PSF becomes oriented in a certain direction when defocusing. As the PSFs start to overlap, this can lead to incorrect parameter estimation when molecules are distributed along some oriented structure like a microtubule. In this case the estimation algorithm tends to distort the PSFs so their orientations align with the underlying structure. This causes a chain effect so parameters of a whole group of molecules are estimated incorrectly. It's worth noting this is certainly not a problem of just our algorithm. We encountered the same issue also with 3D DAOSTORM and others. We believe, this problem is specific to the astigmatic imaging and to the nature of optimization algorithms. Hence, for 3D imaging of dense data we recommend to use a biplane method instead.

To isolate the issue, we generated several datasets of molecules uniformly distributed along horizontal and vertical lines. The axial position of molecules was varied from -400 to +400 nm. Each dataset contained 10 images with 5 molecules and 10 images of 10 molecules distributed along the lines. Then we analyzed the data with 3denseSTORM. Figure 5.11 exposes the problem of astigmatism as the results with higher molecular densities show axial positions biased such that elliptical PSFs align with the lines.

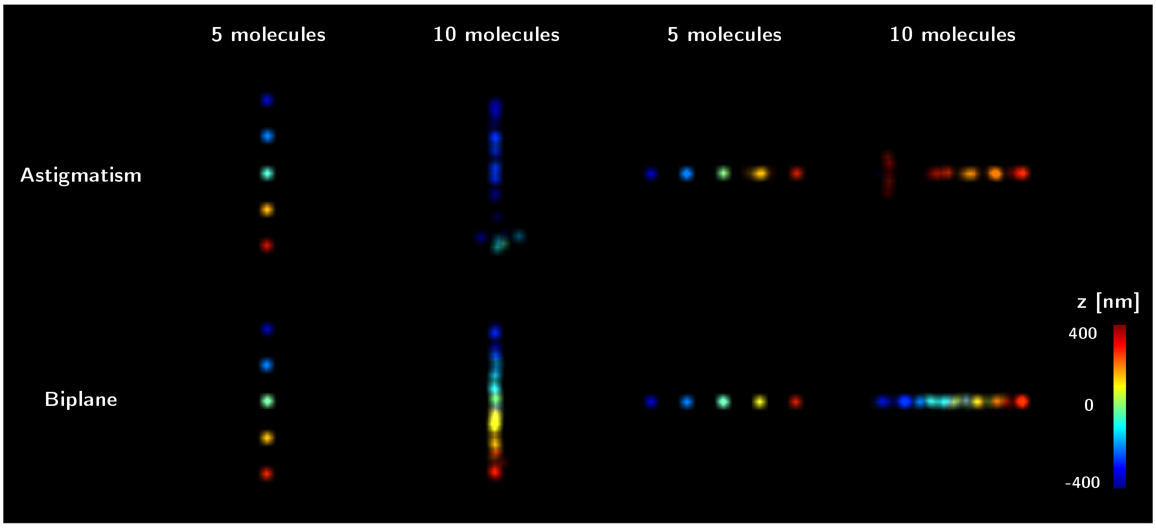

Fig. 5.11 Comparison of astigmatic and biplane 3D imaging of dense data. Each result consists of 10 averaged measurements. Consider the color bar on the bottom right as an example of ground-truth data. Each of the lines is 1.6 μm long.

5.4 Chapter summary

Previously, application of methods based on sparse support recovery for processing SMLM data was shown to outperform single-molecule or multi-emitter fitting approaches, offering better recovery of molecules at high densities and lower localization errors (Min et al., 2014b). This effectively enables imaging with a higher density of molecules, so that a super-resolution image can be reconstructed from far fewer images compared to single-molecule or multi-emitter fitting approaches. This in turn helps facilitate live cell imaging as data can be acquired much faster, potentially capturing dynamic, 3D movements in the sample.

Here we proposed a new algorithm, 3denseSTORM, aimed at processing SMLM data with high molecular density. The algorithm is capable of processing both 2D and 3D single-molecule data and can be extended for any of the commonly used PSFs. Unlike most other currently available methods based on sparse support recovery, 3denseSTORM is memory efficient (representation of the full measurement matrix is avoided), computationally efficient (closed-form solutions of all minimization problems are utilized), and uses a Poisson noise model in both the molecule detection and position refinement steps. Together, this allows for processing of larger 3D images acquired under the extreme low light conditions which are encountered when imaging single molecules. The algorithm is also robust to relatively high background levels and low SNR.

We verified the performance of 3denseSTORM using extensive Monte-Carlo simulations with 3D SMLM data. The results showed that 3denseSTORM can recover the true molecular density about 60% better than 3D DAOSTORM. Also the detection rate as measured by the F1-score and the localization accuracy in both lateral and axial directions were improved compared to other processing algorithms. We also derived the theoretical limits for the maximum density of molecules which can be recovered by methods based on sparse support recovery and we showed that 3denseSTORM achieved detection rates close to this limit. Finally, we pointed out problems typical to astigmatic imaging of dense data that are often silently neglected in the literature.

In future development we would like to add mapping between the planes in biplane mode. Our current implementation https://github.com/zitmen/3densestorm/ assumes they are both perfectly aligned. Also, 3denseSTORM does not use the temporal information contained in a SMLM sequence. Utilizing this information would certainly provide an improvement in detection rate over the current results. This is one of the options for future research. Another possible improvement could be achieved by accounting for noise characteristics of sCMOS cameras, in which each pixel has its own amplifier, therefore each has a different noise characteristics. Such correction was described in (Huang et al., 2013).

Chapter 6

Conclusion

Super-resolution microscopy is a new attractive and dynamic research field which is already producing impactful results in biomedical research. In this thesis we concentrate specifically on image processing and data analysis from single molecule localization microscopy (SMLM). We provided a compact overview of SMLM development and discussed all of its aspects, such as fluorophores, microscope design, image processing, and analysis of the results.

6.1 Contributions

Below we assess our contributions.

ThunderSTORM

We developed open-source software ThunderSTORM, which introduces several new features and concepts for 2D and 3D SMLM data analysis. The software combines several algorithms for SMLM analysis into one comprehensive environment. We introduce a novel rendering algorithm based on averaged shifted histograms and we implement multiple key improvements to provide the best results possible when imaging in real-world environment where different kinds of data exist. This was undoubtedly confirmed when ThunderSTORM won the long sequence part of SMLM Challenge 2013, where nearly 30 softwares were quantitatively compared on multiple sets of artificial and real data. Moreover, ThunderSTORM is the only software which provides such rich repertoire of features for image processing, data post-processing, data analysis, super-resolution rendering, data simulation, and performance evaluation. We currently register over 2600 unique downloads from 57 countries world wide. These numbers were measured by Google Analytics and do not include updates but only first fresh downloads, otherwise the number of downloads would be even higher.

Dual-objective microscope

We built a prototype of dual-objective fluorescence microscope, which we successfully used for multiple of 3D data acquisitions. Compared to a conventional fluorescence microscope, this new microscope doubles the count of collected photons and thus further improves resolution in STORM experiments. The design of the microscope is unique. There is only a handful of similar microscopes in the world and this is the only microscope of its kind in the Czech republic. In addition to the physical device, we also designed a calibration protocol and algorithms for data analysis and we implemented them into ThunderSTORM.

3denseSTORM

We proposed and implemented a novel algorithm, 3denseSTORM, aimed at processing SMLM data with high molecular density. Imaging with a higher density of molecules helps facilitate live cell imaging as data can be acquired much faster, potentially capturing dynamic, 3D movements in the sample. 3denseSTORM algorithm is capable of processing both 2D and 3D single-molecule data and can be extended for any kind of point spread function. The algorithm utilizes concepts from compressed sensing (CS), which was previously shown to provide unprecedented detection rates. However, compared to previously available methods based on CS, 3denseSTORM is orders of magnitude faster and more memory efficient. Moreover, it is currently the only CS based algorithm that uses a Poisson noise model in both the molecule detection and position refinement steps. Together, this allows for processing of larger 3D images acquired under the extreme low light conditions which are encountered when imaging single molecules. The algorithm is robust to high background levels and low signal to noise ratios.

6.2 Directions for future research

There are two major areas for future research and development directly coming from the results of this thesis. First one is to improve the construction of the dual-objective microscope. Specifically the sample holder is not stable enough which causes a drift. Also, a different light source or illumination path could achieve more uniform sample illumination. A second area for future research is utilization of temporal information in our algorithm for analysis of images with high molecular density. This seems to be an opportune direction since there is a pressure to apply super-resolution microscopy in live cell imaging. So, we can slowly see that for example localization microscopy and fluctuation imaging start to converge. Although it is worth noting that localization microscopy has many other applications due to its main strength of imaging individual molecules.

References

Abbe, E. (1873). Beiträge zur Theorie des Mikroskops und der mikroskopischen Wahrnehmung. *Archiv für Mikroskopische Anatomie*, 9(1):413–418.

Abraham, A. V., Ram, S., Chao, J., Ward, E. S., and Ober, R. J. (2009). Quantitative study of single molecule location estimation techniques. *Optics Express*, 17(26):23352–73.

Abramoff, M., Magalhaes, P., and Ram, S. (2004). Image processing with imagej. *Biophotonics International*, 11(7):36–42.

Ambrose, E. J. (1956). A Surface Contact Microscope for the study of Cell Movements. *Nature*, 178(4543):1194–1194.

Aquino, D., Schönle, A., Geisler, C., Middendorff, C. V., Wurm, C. A., Okamura, Y., Lang, T., Hell, S. W., and Egner, A. (2011). Two-color nanoscopy of three-dimensional volumes by 4pi detection of stochastically switched fluorophores. *Nature Methods*, 8(4):353–9.

Axelrod, D. (1981). Cell-substrate contacts illuminated by total internal reflection fluorescence. *The Journal of Cell Biology*, 89(1):141–145.

Babcock, H., Sigal, Y. M., and Zhuang, X. (2012). A high-density 3d localization algorithm for stochastic optical reconstruction microscopy. *Optical Nanoscopy*, 1(1):6.

Babcock, H. P., Moffitt, J. R., Cao, Y., and Zhuang, X. (2013). Fast compressed sensing analysis for super-resolution imaging using l1-homotopy. *Optics Express*, 21(23):28583.

Baddeley, D., Cannell, M. B., and Soeller, C. (2010). Visualization of localization microscopy data. *Microscopy and Microanalysis*, 16(1):64–72.

Badieirostami, M., Lew, M. D., Thompson, M. A., and Moerner, W. E. (2010). Three-dimensional localization precision of the double-helix point spread function versus astigmatism and biplane. *Applied Physics Letters*, 97(16):161103.

Bates, M., Huang, B., Dempsey, G. G. T., and Zhuang, X. (2007). Multicolor super-resolution imaging with photo-switchable fluorescent probes. *Science*, 317(5845):1749–53.

Betzig, E., Patterson, G. H., Sougrat, R., Lindwasser, O. W., Olenych, S., Bonifacino, J. S., Davidson, M. W., Lippincott-Schwartz, J., and Hess, H. F. (2006). Imaging intracellular fluorescent proteins at nanometer resolution. *Science*, 313(5793):1642–5.

Betzig, E. and Trautman, J. K. (1992). Near-field optics: microscopy, spectroscopy, and surface modification beyond the diffraction limit. *Science*, 257(5067):189–95.

Bevington, P. R. and Robinson, D. K. (2003). *Data reduction and error analysis for the physical sciences*. McGraw-Hill Education, 336 pages.

Biteen, J. S., Thompson, M. A., Tselentis, N. K., Bowman, G. R., Shapiro, L., and Moerner, W. E. (2008). Super-resolution imaging in live caulobacter crescentus cells using photoswitchable eyfp. *Nature Methods*, 5(11):947–949.

Bornfleth, H., Saetzler, K., Eils, R., and Cremer, C. (1998). High-precision distance measurements and volume-conserving segmentation of objects near and below the resolution limit in three-dimensional confocal fluorescence microscopy. *Journal of Microscopy*, 189:118–136.

Candes, E. E. and Tao, T. (2005). Decoding by linear programming. page 22.

Candès, E. J. (2008). The restricted isometry property and its implications for compressed sensing. *Comptes Rendus Mathematique*, 346(9-10):589–592.

Chenouard, N., Smal, I., de Chaumont, F., Maška, M., Sbalzarini, I. F., Gong, Y., Cardinale, J., Carthel, C., Coraluppi, S., Winter, M., Cohen, A. R., Godinez, W. J., Rohr, K., Kalaidzidis, Y., Liang, L., Duncan, J., Shen, H., Xu, Y., Magnusson, K. E. G., Jaldén, J., Blau, H. M., Paul-Gilloteaux, P., Roudot, P., Kervrann, C., Waharte, F., Tinevez, J.-Y., Shorte, S. L., Willemse, J., Celler, K., van Wezel, G. P., Dan, H.-W., Tsai, Y.-S., Ortiz de Solórzano, C., Olivo-Marin, J.-C., and Meijering, E. (2014). Objective comparison of particle tracking methods. *Nature Methods*, 11(3):281–9.

Churchman, L. S., Okten, Z., Rock, R. S., Dawson, J. F., and Spudich, J. A. (2005). Single molecule high-resolution colocalization of cy3 and cy5 attached to macromolecules measures intramolecular distances through time. *Proceedings of the National Academy of Sciences of the United States of America*, 102(5):1419–23.

Cleveland, W. S. (1979). Robust Locally Weighted Regression and Smoothing Scatterplots. *Journal of the American Statistical Association*, 74(368):829–836.

Cox, S., Rosten, E., Monypenny, J., Jovanovic-Talisman, T., Burnette, D. T., Lippincott-schwartz, J., Jones, G. E., and Heintzmann, R. (2012). Bayesian localization microscopy reveals nanoscale podosome dynamics. *Nature Methods*, 9(2):195–200.

Crang, R. F. E. (1988). *Artifacts in biological electron microscopy*. Kluwer Academic / Plenum Publishers, 254 pages, facsimile edition.

Daumas, F., Destainville, N., Millot, C., Lopez, A., Dean, D., and Salomé, L. (2003). Confined diffusion without fences of a G-protein-coupled receptor as revealed by single particle tracking. *Biophysical Journal*, 84(1):356–66.

Davidovits, P. and Egger, M. D. (1969). Scanning Laser Microscope. *Nature*, 223(5208):831–831.

Dempsey, G. T., Bates, M., Kowtoniuk, W. E., Liu, D. R., Tsien, R. Y., and Zhuang, X. (2009). Photoswitching mechanism of cyanine dyes. *Journal of the American Chemical Society*, 131(51):18192–18193.

Dempsey, G. T., Vaughan, J. C., Chen, K. H., Bates, M., and Zhuang, X. (2011). Evaluation of fluorophores for optimal performance in localization-based super-resolution imaging. *Nature Methods*, 8(12):1027–36.

Denk, W., Strickler, J., and Webb, W. (1990). Two-photon laser scanning fluorescence microscopy. *Science*, 248(4951):73–76.

Dertinger, T., Colyer, R., Iyer, G., Weiss, S., and Enderlein, J. (2009). Fast, background-free, 3d super-resolution optical fluctuation imaging (sofi). *Proceedings of the National Academy of Sciences of the United States of America*, 106(52):22287–92.

Deschout, H., Zanacchi, F. C., Mlodzianoski, M., Diaspro, A., Bewersdorf, J., Hess, S. T., and Braeckmans, K. (2014). Precisely and accurately localizing single emitters in fluorescence microscopy. *Nature Methods*, 11(3):253–66.

Dickson, R. M., Cubitt, A. B., Tsien, R. Y., and Moerner, W. E. (1997). On/off blinking and switching behaviour of single molecules of green fluorescent protein. *Nature*, 388(6640):355–358.

Donoho, D. (2006). Compressed sensing. *IEEE Transactions on Information Theory*, 52(4):1289–1306.

Drummen, G. P. C. (2012). Fluorescent probes and fluorescence (microscopy) techniques–illuminating biological and biomedical research. *Molecules*, 17(12):14067–90.

Dupé, F.-X., Fadili, J. M., and Starck, J.-L. (2009). A proximal iteration for deconvolving poisson noisy images using sparse representations. *IEEE Transactions on Image Processing*, 18(2):310–21.

Durisic, N., Laparra-Cuervo, L., Sandoval-Álvarez, A., Borbely, J. S., and Lakadamyali, M. (2014). Single-molecule evaluation of fluorescent protein photoactivation efficiency using an in vivo nanotemplate. *Nature Methods*, 11(2):156–62.

Dyba, M. and Hell, S. W. (2002). Focal spots of size lambda/23 open up far-field fluorescence microscopy at 33 nm axial resolution. *Physical Review Letters*, 88(16):163901.

Dyba, M. and Hell, S. W. (2003). Photostability of a fluorescent marker under pulsed excited-state depletion through stimulated emission. *Applied Optics*, 42(25):5123.

Edelstein, A., Amodaj, N., Hoover, K., Vale, R., and Stuurman, N. (2010). Computer control of microscopes using μmanager. *Current Protocols in Molecular Biology*, Chapter 14:Unit14.20.

El Beheiry, M. and Dahan, M. (2013). Visp: representing single-particle localizations in three dimensions. *Nature Methods*, 10(8):689–90.

Eldar, Y. C. and Kutyniok, G. (2012). *Compressed Sensing: Theory And Applications*. 555 pages.

Evanko, D. (2009). Method of the Year 2008. *Nature Methods*, 6(1):1–1.

Fernández-Suárez, M. and Ting, A. Y. (2008). Fluorescent probes for super-resolution imaging in living cells. *Nature Reviews Molecular Cell Biology*, 9(12):929–43.

Figueiredo, M. A. T. and Bioucas-Dias, J. M. (2009). Deconvolution of poissonian images using variable splitting and augmented lagrangian optimization. In *2009 IEEE/SP 15th Workshop on Statistical Signal Processing*, pages 733–736.

Figueiredo, M. A. T. and Bioucas-Dias, J. M. (2010). Restoration of poissonian images using alternating direction optimization. *IEEE Transactions on Image Processing*, 19(12):3133–45.

Fischler, M. A. and Bolles, R. C. (1981). Random sample consensus: a paradigm for model fitting with applications to image analysis and automated cartography. *Communications of the ACM*, 24(6):381–395.

Gale, D. and Shapley, L. S. (1962). College admissions and the stability of marriage. *The American Mathematical Monthly*, 69(1):9–15.

Galloway, C. M., Le Ru, E. C., and Etchegoin, P. G. (2009). An iterative algorithm for background removal in spectroscopy by wavelet transforms. *Applied Spectroscopy*, 63(12):1370–6.

Garcia-Parajo, M. F., Segers-Nolten, G. M. J., Veerman, J.-A., Greve, J., and van Hulst, N. F. (2000). Real-time light-driven dynamics of the fluorescence emission in single green fluorescent protein molecules. *Proceedings of the National Academy of Sciences of the United States of America*, 97(13):7237–7242.

Geissbuehler, S., Sharipov, A., Godinat, A., Bocchio, N. L., Sandoz, P. A., Huss, A., Jensen, N. A., Jakobs, S., Enderlein, J., Gisou van der Goot, F., Dubikovskaya, E. A., Lasser, T., and Leutenegger, M. (2014). Live-cell multiplane three-dimensional super-resolution optical fluctuation imaging. *Nature Communications*, 5:5830.

Göppert-Mayer, M. (1931). Über Elementarakte mit zwei Quantensprüngen. *Annalen der Physik*, 401(3):273–294.

Gordon, M. P., Ha, T., and Selvin, P. R. (2004). Single-molecule high-resolution imaging with photobleaching. *Proceedings of the National Academy of Sciences of the United States of America*, 101(17):6462–5.

Gould, T. J., Gunewardene, M. S., Gudheti, M. V., Verkhusha, V. V., Yin, S.-R., Gosse, J. A., and Hess, S. T. (2008). Nanoscale imaging of molecular positions and anisotropies. *Nature Methods*, 5(12):1027–30.

Gu, L., Sheng, Y., Chen, Y., Chang, H., Zhang, Y., Lv, P., Ji, W., and Xu, T. (2014). High-density 3d single molecular analysis based on compressed sensing. *Biophysical Journal*, 106(11):2443–2449.

Gunkel, M., Erdel, F., Rippe, K., Lemmer, P., Kaufmann, R., Hörmann, C., Amberger, R., and Cremer, C. (2009). Dual color localization microscopy of cellular nanostructures. *Biotechnology Journal*, 4(6):927–938.

Gustafsson, M. G. L. (2000). Surpassing the lateral resolution limit by a factor of two using structured illumination microscopy. *Journal of Microscopy*, 198(2):82–87.

Gustafsson, M. G. L. (2005). Nonlinear structured-illumination microscopy: wide-field fluorescence imaging with theoretically unlimited resolution. *Proceedings of the National Academy of Sciences of the United States of America*, 102(37):13081–6.

Gustafsson, M. G. L., Shao, L., Carlton, P. M., Wang, C. J., Golubovskaya, I. N., Cande, W. Z., Agard, D. A., and Sedat, J. W. (2008). Three-dimensional resolution doubling in wide-field fluorescence microscopy by structured illumination. *Biophysical Journal*, 94(12):4957–4970.

Hanley, Q. S., Verveer, P. J., Gemkow, M. J., Arndt-Jovin, D., and Jovin, T. M. (1999). An optical sectioning programmable array microscope implemented with a digital micromirror device. *Journal of Microscopy*, 196(Pt 3):317–31.

Harmany, Z. T., Marcia, R. F., and Willett, R. M. (2009). Sparse poisson intensity reconstruction algorithms. page 4.

Hartley, R. (1997). In defense of the eight-point algorithm. *IEEE Transactions on Pattern Analysis and Machine Intelligence*, 19(6):580–593.

Hartley, R. and Zisserman, A. (2003). *Multiple View Geometry in Computer Vision*. Cambridge University Press, 655 pages.

Hecht, E. (2001). *Optics*. Addison-Wesley, 680 pages, 4 edition.

Hedde, P. N., Fuchs, J., Oswald, F., Wiedenmann, J., and Nienhaus, G. U. (2009). Online image analysis software for photoactivation localization microscopy. *Nature Methods*, 6(10):689–90.

Heilemann, M., van de Linde, S., Schuttpelz, M., Kasper, R., Seefeldt, B., Mukherjee, A., Tinnefeld, P., Sauer, M., van de Linde, S., and Schüttpelz, M. (2008). Subdiffraction-resolution fluorescence imaging with conventional fluorescent probes. *Angewandte Chemie International Edition*, 47:6172–6176.

Hell, S. and Stelzer, E. H. (1992). Fundamental improvement of resolution with a 4Pi-confocal fluorescence microscope using two-photon excitation. *Optics Communications*, 93(5-6):277–282.

Hell, S. W. and Wichmann, J. (1994). Breaking the diffraction resolution limit by stimulated emission: stimulated-emission-depletion fluorescence microscopy. *Optics Letters*, 19(11):780–2.

Henriques, R., Lelek, M., Fornasiero, E. F., Valtorta, F., Zimmer, C., and Mhlanga, M. M. (2010). QuickPALM: 3D real-time photoactivation nanoscopy image processing in ImageJ. *Nature Methods*, 7(5):339–40.

Hess, S. T., Girirajan, T. P. K., and Mason, M. D. (2006). Ultra-high resolution imaging by fluorescence photoactivation localization microscopy. *Biophysical Journal*, 91(11):4258–72.

Hirsch, M., Wareham, R. J., Martin-Fernandez, M. L., Hobson, M. P., and Rolfe, D. J. (2013). A stochastic model for electron multiplication charge-coupled devices–from theory to practice. *PLoS ONE*, 8(1):e53671.

Holden, S. J., Uphoff, S., and Kapanidis, A. N. (2011). Daostorm: an algorithm for high-density super-resolution microscopy. *Nature Methods*, 8(4):279–80.

Huang, B., Bates, M., and Zhuang, X. (2009). Super-resolution fluorescence microscopy. *Annual Review of Biochemistry*, 78:993–1016.

Huang, B., Jones, S. A., Brandenburg, B., and Zhuang, X. (2008a). Whole-cell 3d storm reveals interactions between cellular structures with nanometer-scale resolution. *Nature Methods*, 5(12):1047–1052.

Huang, B., Wang, W., Bates, M., and Zhuang, X. (2008b). Three-dimensional super-resolution imaging by stochastic optical reconstruction microscopy. *Science*, 319(5864):810–3.

Huang, F., Hartwich, T. M. P., Rivera-Molina, F. E., Lin, Y., Duim, W. C., Long, J. J., Uchil, P. D., Myers, J. R., Baird, M. A., Mothes, W., Davidson, M. W., Toomre, D., and Bewersdorf, J. (2013). Video-rate nanoscopy using scmos camera-specific single-molecule localization algorithms. *Nature Methods*, advance on(7):653–8.

Huang, F., Schwartz, S. L., Byars, J. M., and Lidke, K. A. (2011). Simultaneous multiple-emitter fitting for single molecule super-resolution imaging. *Biomedical Optics Express*, 2(5):1377–93.

Huisken, J., Swoger, J., Del Bene, F., Wittbrodt, J., and Stelzer, E. H. K. (2004). Optical sectioning deep inside live embryos by selective plane illumination microscopy. *Science*, 305(5686):1007–9.

Izeddin, I., Boulanger, J., Racine, V., Specht, C. G., Kechkar, A., Nair, D., Triller, A., Choquet, D., Dahan, M., and Sibarita, J. B. (2012). Wavelet analysis for single molecule localization microscopy. *Optics Express*, 20(3):2081–95.

Juette, M. F., Gould, T. J., Lessard, M. D., Mlodzianoski, M. J., Nagpure, B. S., Bennett, B. T., Hess, S. T., and Bewersdorf, J. (2008). Three-dimensional sub-100 nm resolution fluorescence microscopy of thick samples. *Nature Methods*, 5(6):527–9.

Kao, H. P. and Verkman, A. S. (1994). Tracking of single fluorescent particles in three dimensions: use of cylindrical optics to encode particle position. *Biophysical Journal*, 67(3):1291–300.

Kendall, M. and Stuart, A. (1979). *The Advanced Theory of Statistics*. London: Charles Griffin, 700 pages.

Kirshner, H., Aguet, F., Sage, D., and Unser, M. (2013). 3-d psf fitting for fluorescence microscopy: implementation and localization application. *Journal of Microscopy*, 249(1):13–25.

Kirshner, H., Sage, D., and Unser, M. (2011). 3D PSF models for fluorescence microscopy in ImageJ. In *Proceedings of the Twelfth International Conference on Methods and Applications of Fluorescence Spectroscopy, Imaging and Probes (MAF'11)*, page 154.

Křížek, P., Raška, I., and Hagen, G. M. (2012). Flexible structured illumination microscope with a programmable illumination array. *Optics Express*, 20(22):24585–99.

Klar, T. A. and Hell, S. W. (1999). Subdiffraction resolution in far-field fluorescence microscopy. *Optics Letters*, 24(14):954–6.

Knuth, D. E. (1997). *The Art Of Computer Programming*, volume 1. Addison-Wesley, 672 pages, Boston, 3rd edition.

Kobayashi, H., Ogawa, M., Alford, R., Choyke, P. L., and Urano, Y. (2010). New strategies for fluorescent probe design in medical diagnostic imaging. *Chemical Reviews*, 110(5):2620–40.

Křížek, P., Raška, I., and Hagen, G. M. (2011). Minimizing detection errors in single molecule localization microscopy. *Optics Express*, 19(4):3226–35.

Kusumi, A., Sako, Y., and Yamamoto, M. (1993). Confined lateral diffusion of membrane receptors as studied by single particle tracking (nanovid microscopy). effects of calcium-induced differentiation in cultured epithelial cells. *Biophysical Journal*, 65(5):2021–2040.

Laurence, T. A. and Chromy, B. A. (2010). Efficient maximum likelihood estimator fitting of histograms. *Nature Methods*, 7(5):338–9.

Lemmer, P., Gunkel, M., Baddeley, D., Kaufmann, R., Urich, A., Weiland, Y., Reymann, J., Müller, P., Hausmann, M., and Cremer, C. (2008). Spdm: light microscopy with single-molecule resolution at the nanoscale. *Applied Physics B*, 93(1):1–12.

Lemmer, P., Gunkel, M., Weiland, Y., Müller, P., Baddeley, D., Kaufmann, R., Urich, a., Eipel, H., Amberger, R., Hausmann, M., and Cremer, C. (2009). Using conventional fluorescent markers for far-field fluorescence localization nanoscopy allows resolution in the 10-nm range. *Journal of Microscopy*, 235(2):163–71.

Lew, M. D., Thompson, M. A., Badieirostami, M., and Moerner, W. E. (2010). In vivo Three-Dimensional Superresolution Fluorescence Tracking using a Double-Helix Point Spread Function. In Enderlein, J., Gryczynski, Z. K., and Erdmann, R., editors, *Proceedings - Society of Photo-Optical Instrumentation Engineers*, volume 7571, pages 75710Z–75710Z–13.

Lew, M. D., von Diezmann, A. R. S., and Moerner, W. E. (2013). Easy-DHPSF open-source software for three-dimensional localization of single molecules with precision beyond the optical diffraction limit. *Protocol Exchange*, 2013.

Lidke, K. A., Rieger, B., Jovin, T. M., and Heintzmann, R. (2005). Superresolution by localization of quantum dots using blinking statistics. *Optics Express*, 13(18):7052.

Longuet-Higgins, H. C. (1981). A computer algorithm for reconstructing a scene from two projections. *Nature*, 293(5828):133–135.

Ma, H., Long, F., Zeng, S., and Huang, Z.-L. (2012). Fast and precise algorithm based on maximum radial symmetry for single molecule localization. *Optics Letters*, 37(13):2481–3.

Malkusch, S., Endesfelder, U., Mondry, J., Gelléri, M., Verveer, P. J., and Heilemann, M. (2012). Coordinate-based colocalization analysis of single-molecule localization microscopy data. *Histochemistry and Cell Biology*, 137(1):1–10.

Mandula, O., Šestak, I. Š., Heintzmann, R., and Williams, C. K. I. (2014). Localisation microscopy with quantum dots using non-negative matrix factorisation. *Optics Express*, 22(20):24594.

Manley, S., Gillette, J. M., Patterson, G. H., Shroff, H., Hess, H. F., Betzig, E., and Lippincott-Schwartz, J. (2008). High-density mapping of single-molecule trajectories with photoactivated localization microscopy. *Nature Methods*, 5(2):155–7.

McKinney, S. A., Murphy, C. S., Hazelwood, K. L., Davidson, M. W., and Looger, L. L. (2009). A bright and photostable photoconvertible fluorescent protein. *Nature Methods*, 6(2):131–3.

Min, J., Holden, S. J., Carlini, L., Unser, M., Manley, S., and Ye, J. C. (2014a). 3D high-density localization microscopy using hybrid astigmatic/ biplane imaging and sparse image reconstruction. *Biomedical Optics Express*, 5(11):3935.

Min, J., Vonesch, C., Kirshner, H., Carlini, L., Olivier, N., Holden, S., Manley, S., Ye, J. C., and Unser, M. (2014b). FALCON: fast and unbiased reconstruction of high-density super-resolution microscopy data. *Scientific Reports*, 4:4577.

Minsky, M. (1988). Memoir on inventing the confocal scanning microscope. *Scanning*, 10(4):128–138.

Mlodzianoski, M. J., Schreiner, J. M., Callahan, S. P., Smolková, K., Dlasková, A., Santorová, J., Ježek, P., and Bewersdorf, J. (2011). Sample drift correction in 3d fluorescence photoactivation localization microscopy. *Optics Express*, 19(16):15009–19.

Moffitt, J. R., Osseforth, C., and Michaelis, J. (2011). Time-gating improves the spatial resolution of STED microscopy. *Optics Express*, 19(5):4242–54.

Mortensen, K. I., Churchman, L. S., Spudich, J. A., and Flyvbjerg, H. (2010). Optimized localization analysis for single-molecule tracking and super-resolution microscopy. *Nature Methods*, 7(5):377–81.

Mukamel, E. A., Babcock, H., and Zhuang, X. (2012). Statistical deconvolution for superresolution fluorescence microscopy. *Biophysical Journal*, 102(10):2391–400.

O'Neill, R. (1971). Algorithm AS 47 - function minimization using a simplex procedure. *Applied Statistics*, 20:338–345.

Ovesný, M., Křížek, P., Borkovec, J., Švindrych, Z., and Hagen, G. M. (2014a). ThunderSTORM: a comprehensive ImageJ plug-in for PALM and STORM data analysis and super-resolution imaging. *Bioinformatics*, 30(16):2389–2390.

Ovesný, M., Křížek, P., Švindrych, Z., and Hagen, G. M. (2014b). High density 3D localization microscopy using sparse support recovery. *Optics Express*, 22(25):31263.

Owen, D. M., Rentero, C., Magenau, A., Williamson, D., Rodriguez, M., Gaus, K., and Rossy, J. (2010). PALM imaging and cluster analysis of protein heterogeneity at the cell surface. *Journal of Biophotonics*, 3(7):446–454.

Owen, D. M., Williamson, D., Magenau, A., and Gaus, K. (2012). Optical techniques for imaging membrane domains in live cells (live-cell PALM of protein clustering). *Methods Enzymol*, 504:221–235.

Parthasarathy, R. (2012). Rapid, accurate particle tracking by calculation of radial symmetry centers. *Nature Methods*, 9(7):724–6.

Pavani, S. R. P. and Piestun, R. (2008). High-efficiency rotating point spread functions. *Optics Express*, 16(5):3484.

Pavani, S. R. P., Thompson, M. A., Biteen, J. S., Lord, S. J., Liu, N., Twieg, R. J., Piestun, R., Moerner, W. E., Rama, S., and Pavani, P. (2009). Three-dimensional, single-molecule fluorescence imaging beyond the diffraction limit by using a double-helix point spread function. *Proceedings of the National Academy of Sciences of the United States of America*, 106(9):2995–9.

Pellett, P. A., Sun, X., Gould, T. J., Rothman, J. E., Xu, M.-Q., Corrêa, I. R., and Bewersdorf, J. (2011). Two-color STED microscopy in living cells. *Biomedical Optics Express*, 2(8):2364–71.

Pengo, T., Holden, S. J., and Manley, S. (2014). PALMsiever: a tool to turn raw data into results for single-molecule localization microscopy. *Bioinformatics*, pages 797–798.

Petráň, M., Hadravský, M., Egger, M. D., and Galambos, R. (1968). Tandem-scanning reflected-light microscope. *Journal of the Optical Society of America*, 58(5):661–664.

Press, W. H. (2007). *Numerical Recipes 3rd Edition: The Art of Scientific Computing*. Cambridge University Press, 1235 pages.

Qu, X., Wu, D., Mets, L., and Scherer, N. F. (2004). Nanometer-localized multiple single-molecule fluorescence microscopy. *Proceedings of the National Academy of Sciences of the United States of America*, 101(31):11298–303.

Quan, T., Zeng, S., and Huang, Z.-L. (2010). Localization capability and limitation of electron-multiplying charge-coupled, scientific complementary metal-oxide semiconductor, and charge-coupled devices for superresolution imaging. *Journal of Biomedical Optics*, 15(6):066005.

Ram, S., Chao, J., Prabhat, P., Ward, E. S., and Ober, R. J. (2007). A novel approach to determining the threedimensional location of microscopic objects with applications to 3d particle tracking. In Conchello, J.-A., Cogswell, C. J., and Wilson, T., editors, *Three-Dimensional and Multidimensional Microscopy: Image Acquisition and Processing XIV. Edited by Conchello*, volume 6443, pages 64430D–64430D–7.

Ram, S., Prabhat, P., Ward, E. S., and Ober, R. J. (2009). Improved single particle localization accuracy with dual objective multifocal plane microscopy. *Optics Express*, 17(8):6881.

Rayleigh, F. R. S. (1879). XXXI. Investigations in optics, with special reference to the spectroscope. *Philosophical Magazine Series 5*, 8(49):261–274.

Rieger, B. and Stallinga, S. (2014). The lateral and axial localization uncertainty in super-resolution light microscopy. *Chemistry Physical*, 15(4):664–70.

Ronneberger, O., Baddeley, D., Scheipl, F., Verveer, P. J., Burkhardt, H., Cremer, C., Fahrmeir, L., Cremer, T., and Joffe, B. (2008). Spatial quantitative analysis of fluorescently labeled nuclear structures: Problems, methods, pitfalls. *Chromosome Research*, 16(3):523–562.

Rossy, J., Cohen, E., Gaus, K., and Owen, D. M. (2014). Method for co-cluster analysis in multichannel single-molecule localisation data. *Histochemistry and Cell Biology*, 141(6):605–12.

Rust, M. J., Bates, M., and Zhuang, X. (2006). Sub-diffraction-limit imaging by stochastic optical reconstruction microscopy (storm). *Nature Methods*, 3(10):793–5.

Ruusuvuori, P., Aijö, T., Chowdhury, S., Garmendia-Torres, C., Selinummi, J., Birbaumer, M., Dudley, A. M., Pelkmans, L., and Yli-Harja, O. (2010). Evaluation of methods for detection of fluorescence labeled subcellular objects in microscope images. *BMC Bioinformatics*, 11(1):248.

Sage, D., Kirshner, H., Pengo, T., Stuurman, N., Min, J., Manley, S., and Unser, M. (2015). Quantitative evaluation of software packages for single-molecule localization microscopy. *Nature Methods*.

Schindelin, J., Arganda-Carreras, I., Frise, E., Kaynig, V., Longair, M., Pietzsch, T., Preibisch, S., Rueden, C., Saalfeld, S., Schmid, B., Tinevez, J.-Y., White, D. J., Hartenstein, V., Eliceiri, K., Tomancak, P., and Cardona, A. (2012). Fiji: an open-source platform for biological-image analysis. *Nature Methods*, 9(7):676–82.

Scott, D. W. (1985). Averaged shifted histograms: effective nonparametric density estimators in several dimensions. *The Annals of Statistics*, 13(3):1024–1040.

Setzer, S., Steidl, G., and Teuber, T. (2010). Deblurring poissonian images by split bregman techniques. *Journal of Visual Communication and Image Representation*, 21(3):193–199.

Shechtman, Y., Sahl, S. J., Backer, A. S., and Moerner, W. E. (2014). Optimal point spread function design for 3d imaging. *Physical Review Letters*, 113(13):133902.

Shen, Z. and Andersson, S. B. (2011). Bias and precision of the fluorobancroft algorithm for single particle localization in fluorescence microscopy. *IEEE Transactions on Signal Processing*, 59(8):4041–4046.

Shroff, H., Galbraith, C. G., Galbraith, J. A., and Betzig, E. (2008). Live-cell photoactivated localization microscopy of nanoscale adhesion dynamics. *Nature Methods*, 5(5):417–23.

Shroff, H., Galbraith, C. G., Galbraith, J. a., White, H., Gillette, J., Olenych, S., Davidson, M. W., and Betzig, E. (2007). Dual-color superresolution imaging of genetically expressed probes within individual adhesion complexes. *Proceedings of the National Academy of Sciences of the United States of America*, 104(51):20308–20313.

Shtengel, G., Galbraith, J. A., Galbraith, C. G., Lippincott-Schwartz, J., Gillette, J. M., Manley, S., Sougrat, R., Waterman, C. M., Kanchanawong, P., Davidson, M. W., Fetter, R. D., and Hess, H. F. (2009). Interferometric fluorescent super-resolution microscopy resolves 3d cellular ultrastructure. *Proceedings of the National Academy of Sciences of the United States of America*, 106(9):3125–30.

Simonson, P. D., Rothenberg, E., and Selvin, P. R. (2011). Single-molecule-based super-resolution images in the presence of multiple fluorophores. *Nano Letters*, 11(11):5090–6.

Small, A. and Stahlheber, S. (2014). Fluorophore localization algorithms for super-resolution microscopy. *Nature Methods*, 11(3):267–79.

Smirnov, E. B. J., Kováčik, L., Svidenská, S., Schröfel, A., Skalníková, M., Švindrych, Z., Křížek, P., Ovesný, M., Hagen, G. M. G. M., Jůda, P., Michalová, K., Cardoso, M. C., Cmarko, D., Raška, I., Borkovec, J., and Juda, P. (2014). Separation of replication and transcription domains in nucleoli. *Journal of Structural Biology*.

Smith, C. S., Joseph, N., Rieger, B., and Lidke, K. A. (2010). Fast, single-molecule localization that achieves theoretically minimum uncertainty. *Nature Methods*, 7(5):373–5.

Smith, P. J., Taylor, C. M., Shaw, A. J., and McCabe, E. M. (2000). Programmable array microscopy with a ferroelectric liquid-crystal spatial light modulator. *Applied Optics*, 39(16):2664.

Sparrow, C. M. (1916). On Spectroscopic Resolving Power. *The Astrophysical Journal*, 44:76.

Stallinga, S. and Rieger, B. (2010). Accuracy of the gaussian point spread function model in 2D localization microscopy. *Optics Express*, 18(24):24461–24476.

Starck, J.-L. and Murtagh, F. (2002). *Astronomical Image and Data Analysis*. Springer, 338 pages.

Subach, F. V., Patterson, G. H., Renz, M., Lippincott-schwartz, J., and Verkhusha, V. V. (2010). Bright monomeric photoactivatable red fluorescent protein for two-color super-resolution sptPALM of live cells. *Journal of the American Chemical Society*, 132(18):6481–6491.

Sun, T. and Andersson, S. B. (2007). Precise 3-d localization of fluorescent probes without numerical fitting. *IEEE Engineering in Medicine and Biology Society. Annual Conference*, 2007:4181–4.

Tan, P. N., Steinbach, M., and Kumar, V. (2005). *Introduction to Data Mining*. Addison-Wesley Longman Publishing Co., 769 pages.

Thompson, R. E., Larson, D. R., and Webb, W. W. (2002). Precise nanometer localization analysis for individual fluorescent probes. *Biophysical Journal*, 82(5):2775–83.

Uppoor, R. and Niebergall, P. J. (1996). beta-d(+) glucose-glucose oxidase-catalase for use as an antioxidant system. *Pharmaceutical Development and Technology*, 1(2):127–34.

van de Linde, S., Kasper, R., Heilemann, M., and Sauer, M. (2008a). Photoswitching microscopy with standard fluorophores. *Applied Physics B*, 93(4):725–731.

van de Linde, S., Sauer, M., and Heilemann, M. (2008b). Subdiffraction-resolution fluorescence imaging of proteins in the mitochondrial inner membrane with photoswitchable fluorophores. *Journal of Structural Biology*, 164(3):250–254.

Vicidomini, G., Moneron, G., Han, K. Y., Westphal, V., Ta, H., Reuss, M., Engelhardt, J., Eggeling, C., and Hell, S. W. (2011). Sharper low-power STED nanoscopy by time gating. *Nature Methods*, 8(7):571–3.

Vogelsang, J., Cordes, T., Forthmann, C., Steinhauer, C., and Tinnefeld, P. (2009). Controlling the fluorescence of ordinary oxazine dyes for single-molecule switching and superresolution microscopy. *Proceedings of the National Academy of Sciences of the United States of America*, 106(20):8107–8112.

Vogelsang, J., Kasper, R., Steinhauer, C., Person, B., Heilemann, M., Sauer, M., and Tinnefeld, P. (2008). A reducing and oxidizing system minimizes photobleaching and blinking of fluorescent dyes13. *Angewandte Chemie International Edition*, 47(29):5465–5469.

Šonka, M., Hlaváč, V., and Boyle, R. (2007). *Image Processing, Analysis, and Machine Vision*. Cengage Learning, 872 pages, 3rd edition edition.

Weisshart, K. (2014). The Basic Principle of Airyscanning. Technology note, Carl Zeiss Microscopy. Available from: http://confocal-club.ru/upload/article/EN_wp_LSM-880_Basic-Principle-Airyscan.pdf.

Westphal, V. and Hell, S. W. (2005). Nanoscale resolution in the focal plane of an optical microscope. *Physical Review Letters*, 94(14):143903.

Westphal, V., Rizzoli, S. O., Lauterbach, M. A., Kamin, D., Jahn, R., and Hell, S. W. (2008). Video-rate far-field optical nanoscopy dissects synaptic vesicle movement. *Science*, 320(5873):246–9.

Wiedenmann, J., Ivanchenko, S., Oswald, F., Schmitt, F., Röcker, C., Salih, A., Spindler, K.-D., and Nienhaus, G. U. (2004). Eosfp, a fluorescent marker protein with uv-inducible green-to-red fluorescence conversion. *Proceedings of the National Academy of Sciences of the United States of America*, 101(45):15905–10.

Wolter, S., Löschberger, A., Holm, T., Aufmkolk, S., Dabauvalle, M.-C., van de Linde, S., and Sauer, M. (2012). rapidstorm: accurate, fast open-source software for localization microscopy. *Nature Methods*, 9(11):1040–1.

Xu, K., Babcock, H. P., and Zhuang, X. (2012). Dual-objective storm reveals three-dimensional filament organization in the actin cytoskeleton. *Nature Methods*, 9(2):185–8.

Xu, K., Zhong, G., and Zhuang, X. (2013). Actin, spectrin, and associated proteins form a periodic cytoskeletal structure in axons. *Science*, 339(6118):452–6.

Yildiz, A., Forkey, J. N., McKinney, S. a., Ha, T., Goldman, Y. E., and Selvin, P. R. (2003). Myosin v walks hand-over-hand: Single fluorophore imaging with 1.5-nm localization. *Science*, 300(5628):2061–2065.

York, A. G., Ghitani, A., Vaziri, A., Davidson, M. W., and Shroff, H. (2011). Confined activation and subdiffractive localization enables whole-cell PALM with genetically expressed probes. *Nature Methods*, 8(4):327–33.

Zhu, L., Zhang, W., Elnatan, D., and Huang, B. (2012). Faster storm using compressed sensing. *Nature Methods*, 9(7):721–3.